


---

# Hybrid Quantum Monte Carlo for Condensed Matter Models

---



Dissertation zur Erlangung des  
naturwissenschaftlichen Doktorgrades  
der Julius-Maximilians-Universität Würzburg

vorgelegt von  
Stefan Beyl

aus  
Heilbronn

Würzburg 2019

Eingereicht am: 01.08.2019  
bei der Fakultät für Physik und Astronomie

1. Gutachter: Prof. Dr. Fakher F. Assaad
2. Gutachter: Prof. Dr. Giorgio Sangiovanni
3. Gutachter:  
der Dissertation

Vorsitzender: Prof. Dr. Hays Hinrichsen

1. Prüfer: Prof. Dr. Fakher F. Assaad
2. Prüfer: Prof. Dr. Giorgio Sangiovanni
3. Prüfer: Prof. Dr. Ralph Claessen  
im Promotionskolloquium

Tag des Promotionskolloquiums: 23.09.2019

Doktorurkunde ausgehändigt am:



This document is licensed under a Creative Commons  
Attribution-ShareAlike 4.0 International License (CC BY-SA 4.0):  
<https://creativecommons.org/licenses/by-sa/4.0/deed.en>



# Abstract

In this thesis we consider the hybrid quantum Monte Carlo method for simulations of the Hubbard and Su-Schrieffer-Heeger model. In the first instance, we discuss the hybrid quantum Monte Carlo method for the Hubbard model on a square lattice. We point out potential ergodicity issues and provide a way to circumvent them by a complexification of the method. Furthermore, we compare the efficiency of the hybrid quantum Monte Carlo method with a well established determinantal quantum Monte Carlo method for simulations of the half-filled Hubbard model on square lattices. One reason why the hybrid quantum Monte Carlo method loses the comparison is that we do not observe the desired sub-quadratic scaling of the numerical effort. Afterwards we present a formulation of the hybrid quantum Monte Carlo method for the Su-Schrieffer-Heeger model in two dimensions. Electron-phonon models like this are in general very hard to simulate using other Monte Carlo methods in more than one dimensions. It turns out that the hybrid quantum Monte Carlo method is much better suited for this model. We achieve favorable scaling properties and provide a proof of concept. Subsequently, we use the hybrid quantum Monte Carlo method to investigate the Su-Schrieffer-Heeger model in detail at half-filling in two dimensions. We present numerical data for staggered valence bond order at small phonon frequencies and an antiferromagnetic order at high frequencies. Due to an  $O(4)$  symmetry the antiferromagnetic order is connected to a superconducting charge density wave. Considering the Su-Schrieffer-Heeger model without tight-binding hopping reveals an additional unconstrained  $\mathbb{Z}_2$  gauge theory. In this case, we find indications for  $\pi$ -fluxes and a possible  $\mathbb{Z}_2$  Dirac deconfined phase as well as for a columnar valence bond ordered state at low phonon energies. In our investigations of the several phase transitions we discuss the different possibilities for the underlying mechanisms and reveal first insights into a rich phase diagram.



# Zusammenfassung

In der vorliegenden Arbeit betrachten wir die Hybrid-Quanten-Monte-Carlo-Methode für Simulationen des Hubbard- sowie des Su-Schrieffer-Heeger-Modells. Zunächst diskutieren wir die Hybrid-Quanten-Monte-Carlo-Methode am Beispiel des Hubbard-Modells auf dem Quadratgitter. Wir zeigen mögliche Ergodizitätsprobleme auf und präsentieren eine Möglichkeit, diese durch Verwendung komplexwertiger Hilfsfelder zu vermeiden. Für Simulationen des halbgefüllten Hubbard-Modells auf Quadratgittern vergleichen wir die Effizienz der Hybrid-Quanten-Monte-Carlo-Methode mit der einer weit verbreiteten und gebräuchlichen Determinanten-Quanten-Monte-Carlo-Methode. Ein Grund für die Niederlage der Hybrid-Quanten-Monte-Carlo-Methode in diesem Vergleich ist die Skalierung des benötigten Rechenaufwandes. Die erhoffte sub-quadratische Skalierung in Abhängigkeit von Systemgröße und inverser Temperatur wird nicht beobachtet. Anschließend präsentieren wir eine Formulierung der Hybrid-Quanten-Monte-Carlo-Methode zur Untersuchung des halbgefüllten Su-Schrieffer-Heeger-Modells in zwei Dimensionen. Elektron-Phonon-Modelle wie dieses sind in mehr als einer Dimension für gewöhnlich mit anderen Quanten-Monte-Carlo-Methoden nur schwer simulierbar. Es stellt sich heraus, dass sich die Hybrid-Quanten-Monte-Carlo-Methode deutlich besser zur Simulation dieses Modells eignet. Wir erreichen eine vorteilhafte Skalierung des Rechenaufwandes und präsentieren einen Machbarkeitsnachweis. Folglich verwenden wir die Hybrid-Quanten-Monte-Carlo-Methode für nähere Untersuchungen des Su-Schrieffer-Heeger-Modells. Wir zeigen numerische Resultate für eine gestaffelte Ordnung aus Valenzbindungen bei kleinen Phononfrequenzen und für eine antiferromagnetischen Ordnung bei hohen Frequenzen. Aufgrund einer  $O(4)$ -Symmetrie ist die antiferromagnetische Ordnung mit einer supraleitenden Ladungsdichtewelle verknüpft. Ohne Tight-Binding-Hüpfparameter offenbart das Su-Schrieffer-Heeger-Modell eine zusätzliche spezielle  $\mathbb{Z}_2$ -Eichsymmetrie, die nicht den Satz von Gauß erfüllt. In diesem Fall finden wir Hinweise für einen  $\pi$ -Flux-Zustand. Bei niedrigen Phononenergien gibt es außerdem Anzeichen für einen möglichen  $\mathbb{Z}_2$  Dirac deconfined Zustand sowie eine spaltenweise Ordnung von Valenzbindungen. Bei Untersuchungen der Phasenübergänge beleuchten wir die möglichen Mechanismen, die den Übergängen zugrunde liegen. Zum Abschluss diskutieren wir das vielfältige Phasendiagramm, in welches wir erste Einblicke ermöglichen.





# Contents

<b>1</b>	<b>Introduction</b>	<b>1</b>
1.1	Motivation and goal of this work . . . . .	1
1.2	Scope and outline . . . . .	2
<b>I</b>	<b>The Hybrid Quantum Monte Carlo Method</b>	<b>5</b>
<b>2</b>	<b>Monte Carlo – From randomness to certainty</b>	<b>7</b>
2.1	History and motivation of the Monte Carlo method . . . . .	7
2.2	Monte Carlo sampling . . . . .	10
2.3	Metropolis algorithm . . . . .	11
2.4	Updating schemes . . . . .	13
<b>3</b>	<b>Hybrid Quantum Monte Carlo method on the Hubbard model</b>	<b>15</b>
3.1	Basic Formulation . . . . .	15
3.2	The Hybrid Monte Carlo updating scheme . . . . .	19
3.3	The right choice of the integrator . . . . .	21
3.4	How to evaluate the forces and measure observables . . . . .	23
3.5	Solution of linear systems with the conjugate gradient method . . . . .	24
3.6	Ergodicity . . . . .	29
<b>4</b>	<b>Complex Hybrid Quantum Monte Carlo method for the Hubbard model</b>	<b>33</b>
4.1	Complexification . . . . .	33
4.2	Results of the complex HQMC . . . . .	37
4.3	Comparison with the BSS-QMC method for the Hubbard model . . . . .	39
<b>5</b>	<b>Hybrid Quantum Monte Carlo method on the SSH model</b>	<b>43</b>
5.1	HQMC formulation for the SSH model . . . . .	43
5.2	Proof of concept . . . . .	47

<b>II</b>	<b>The Physics of the two-dimensional SSH Model</b>	<b>51</b>
<b>6</b>	<b>The two-dimensional SSH model</b>	<b>53</b>
6.1	Motivation and Origins . . . . .	53
6.2	Symmetries and Expectations . . . . .	55
6.3	Mean Field Results . . . . .	57
6.4	Frequency-dependent phase transition . . . . .	61
<b>7</b>	<b>Zero hopping limit</b>	<b>77</b>
7.1	Unconstrained gauge theory . . . . .	78
7.2	Vanishing hopping parameter . . . . .	82
7.3	Intermediate hopping regime . . . . .	87
7.4	Possible phase diagram . . . . .	91
<b>8</b>	<b>Conclusion</b>	<b>93</b>
<b>III</b>	<b>Appendix</b>	<b>97</b>
<b>A</b>	<b>Trotter Decomposition</b>	<b>99</b>
<b>B</b>	<b>Data analysis</b>	<b>111</b>
B.1	Jackknife method . . . . .	111
B.2	Rebinning . . . . .	112
	<b>Danksagung</b>	<b>115</b>
	<b>Bibliography</b>	<b>117</b>

# 1

## Introduction

### 1.1 Motivation and goal of this work

Today, the Monte Carlo method is a widely used and well established method for various kinds of simulations. It is used in mathematical optimization [1, 2] as well as in statistics [2] and finance [3]. The roots of modern Monte Carlo methods trace back to physical research in the middle of the last century [4]. Also in theoretical physics the method has been an important tool for many decades. Besides the exact diagonalization methods the quantum Monte Carlo methods are often some of the few methods that get along without approximations for simulations of the strongly correlated many-particle problem, see e.g. [5]. Often they are optimized for a particular purpose. Sophisticated Monte Carlo methods allow to simulate quantum mechanical models that can not be solved analytically [1]. Some Monte Carlo methods have been extended, optimized and polished for decades. In particular, the hybrid (or Hamiltonian) quantum Monte Carlo (HQMC) method [6, 7] is used for calculations in particle physics for many years and is still the most important numerical method in lattice gauge theory and a well established textbook method [8]. While the condensed matter community focused on the very well working determinantal quantum Monte Carlo method, as formulated by Blankenbecler, Scalapino and Sugar (BSS-QMC) [9], attempts to use the HQMC method also for simulations in solid state physics [10] ebbed away. With increasing interests in graphene and hexagonal lattices and the according linear dispersion relation of electrons, lattice gauge theory and solid state physics got a little bit closer. In the following, some people started to apply their HQMC methods, developed for lattice gauge theory simulations, to graphene [11, 12, 13]. Although BSS-QMC and HQMC are related in some points they use different approaches and exhibit different scaling behavior. While the BSS-QMC method uses local updates and changes the components of its configuration vector successively to generate

stochastic samples, the HQMC method is based on a global updating procedure changing all components at the same time. Also the scaling of the computational effort to compute a single sample is different. While the BSS-QMC scales cubically with the spatial volume of the system and linearly with the inverse temperature/imaginary time [14], the HQMC often hybridizes time and spatial dimensions and is reported to achieve a sub-quadratic scaling close to linear in the system size [7, 15]. However, due to its composition the scaling of the HQMC method is not predetermined in general. In consequence of its scaling, the BSS-QMC is limited in the size of lattices and additionally the local updating procedure is often insufficient for some electron-phonon models [16]. Although some recent developments for other Monte Carlo methods like the stochastic series expansion [17] made some progress to simulate electron-phonon models, systematic simulations in more than one dimension are only available for some of the models. In view of ongoing improvements of both numerical methods and computing hardware it is worth to revisit the HQMC method for condensed matter models.

The main goal of this work is to investigate the applicability and performance of the HQMC method in condensed matter and to apply it to models which can not be simulated by the BSS-QMC method. Namely, we aim to use the HQMC method to investigate the phase diagram of the two-dimensional Su-Schrieffer-Heeger model.

## **1.2 Scope and outline**

This thesis is structured in two parts. In the first part, we discuss the most important properties and mechanisms of Monte Carlo methods in Chapter 2. In Chapter 3, we revisit a former formulation of the HQMC method for the Hubbard model, one of the most used models in condensed matter physics. We point out some weak points of the formulation and investigate the reasons. Afterwards we provide a solution to overcome these issues and compare the performance of the HQMC method with a standard implementation of the BSS-QMC method in Chapter 4. In Chapter 5, we adapt the HQMC method to the Su-Schrieffer-Heeger (SSH) model in two dimensions, an electron-phonon model that can not be simulated by other Monte Carlo methods. We conclude the first part with a proof of concept.

The second part of this thesis considers the physics of the two-dimensional SSH model. So far no reliable systematic simulations of the SSH model in two dimensions are available. We use the HQMC method presented in the first part to discuss the ground state properties of the SSH model in Chapter 6. We investigate the phases of the model depending on the energy of the phonons as well as on the strength of the bare electronic hopping which is equivalent to the coupling strength

between electrons and phonons in Chapter 7. We conclude this work in Chapter 8 by a summary and an outlook on potential further investigations initiated by this work.

If nothing else is said we use natural units with  $\hbar = 1$  and normalize all energies by the tight-binding hopping parameter  $t$  which is set unity to simplify the notation.



**Part I**

**The Hybrid Quantum Monte Carlo  
Method**





# 2

## Chapter 2

---

# Monte Carlo – From randomness to certainty

This chapter intends to illustrate the ideas behind Monte Carlo methods and introduce the most important properties that also occur in the following chapters. At the beginning we say some words about the history of the Monte Carlo methods. Afterwards we proceed by pointing out typical use cases in physics before we go on with the basic concepts of Monte Carlo methods. We will further discuss all important properties of Markov chain Monte Carlo methods and the Metropolis algorithm. The chapter is concluded by a short outlook on two updating schemes that are most important for the following chapters.

## 2.1 History and motivation of the Monte Carlo method

The Monte Carlo method, as well as other numerical algorithms, started its triumph march in the second half of the last century when computers enabled scientists to speed up their calculations. Enrico Fermi's first experiments with the Monte Carlo method, in the 1930s, were followed by the pioneering work of Stanislaw Ulam, John von Neumann and Nicholas Metropolis in the 1940s which also named the method [4, 18, 19].

However, Buffon's needles (1733) are often referred to as the first Monte Carlo method application [18]. If a needle of length  $L$  falls onto a plain surface covered with parallel lines at distance  $D$  ( $D > L$ , see Fig. 2.1), the probability for the needle to cross one of the lines is equal to  $p = \frac{2L}{\pi D}$ . Like Laplace proposed later on [18], this idea can be used to estimate the value of  $\pi$  by throwing

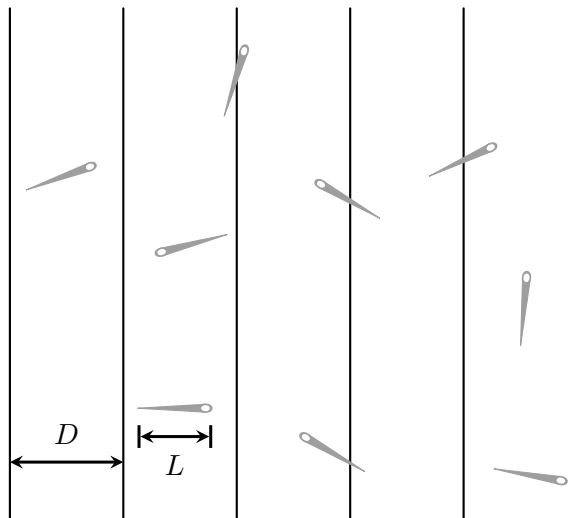


**Figure 2.1:** Sketch of Buffon’s needle experiment. Needles with length  $L$  are lying onto a plain surface covered with parallel lines of distance  $D$  ( $D > L$ ).

a lot of needles onto the surface. If  $n$  of  $N$  needles cross a line we can use the probability  $\frac{n}{N} \approx \frac{2L}{\pi D}$  to approximate

$$\pi \approx \frac{2L N}{D n}. \quad (2.1)$$

Although a giant number of needles is necessary to give a precise approximation of  $\pi$ , this illustrates the usefulness of randomness for calculations. The power of the Monte Carlo method takes effect if problems in larger dimensions are treated. Textbook examples like computing the volume of a unit sphere are used to illustrate the efficiency of Monte Carlo methods. Of course, it is no problem to perform this integration by hand but a numerical integration method, like a Gaussian quadrature, struggles if the dimension is very high. For comparison, a Monte Carlo method is not that sensitive to the dimension of the problem. It assumes a cube surrounding the high dimensional unit sphere and generates randomly points within the cube. For each of those points the Monte Carlo method decides if it is also contained in the unit sphere. The ratio between points inside the unit sphere and the total number of points can be multiplied by the volume of the cube and gives the volume of the sphere. The quality of the Monte Carlo results is only dependent on the number of samples and above a certain dimension it is more efficient to draw random samples than to use another numerical integration method. Therefore Monte Carlo methods can be used to compute integrals or sums which are not evaluable due to their dimension. For illustration we consider an easy example of Ref. [8], considering a system of Ising spins on a lattice in three spatial dimensions and add one dimension for time. Computing the physical properties of a system often requires a summation, or integration, over all possible states of the

system. Due to the two possible states that each of the  $N^4$  spin variables has this means we have to sum over  $2^{N^4}$  configurations. Even for small system sizes like  $N = 16$  the summation would require  $2^{16^4} \approx 10^{19728}$  evaluations. Large lattice simulations in this way are, due to the exponential scaling of the computational effort, even on modern computers not feasible. Furthermore, modern physics is interested in many different types of models, so the configuration space is in general much more complicated compared to the minimal example of Ising spins. More examples, use cases and details can be found in any textbook about Monte Carlo methods like Ref. [2, 18].

Today, Monte Carlo methods are a widely used and very important tool to compute high dimensional integrals in science. Examples like the path integral formulations or the partition function,

$$Z = \text{Tr}\left(e^{-\beta\hat{H}}\right) = \int [\delta x \delta p] \langle x, p | e^{-\beta\hat{H}} | x, p \rangle, \quad (2.2)$$

contain integrals that are often hard to compute. For demonstration purposes the trace contained in the partition function  $Z$  gets evaluated by introducing a basis of position and momentum vectors,  $x$  and  $p$ . (Of course, in practice, the basis is chosen according to the considered model.) The dimension of the spatial and momentum integration is equal to the number of considered particles times the spatial dimension of the model. Although in some cases the integration can be done by hand, in general the considered models are more complicated. Owing to that a numerical brute force calculation can only be successful in special cases. In general sophisticated numerical methods or approximation procedures are necessary. And here the Monte Carlo Method enters. Instead of systematically summing up, or integrating out, the whole configuration space it draws samples out of the configuration space and performs a statistical analysis to estimate the desired result. The reliability of the Monte Carlo result is measured by its statistical standard error. In this way high dimensional integrals, and summations, can be evaluated in a much faster fashion.

In order to motivate the Monte Carlo approach of the following section we draw a line from the physical description to the statistical perspective. From statistical mechanics we know that the expectation value of an observable  $\hat{O}$  in thermal equilibrium is given by

$$\langle \hat{O} \rangle = \frac{\text{Tr}\left(\hat{O} e^{-\beta\hat{H}}\right)}{\text{Tr}\left(e^{-\beta\hat{H}}\right)} = \frac{\int [\delta x \delta p] \langle x, p | \hat{O} e^{-\beta\hat{H}} | x, p \rangle}{\int [\delta x \delta p] \langle x, p | e^{-\beta\hat{H}} | x, p \rangle}. \quad (2.3)$$

Using the language of stochastic processes, we are evaluating the expectation value of  $\hat{O}$  according to a probability distribution which is proportional to the Boltzmann weight  $e^{-\beta\hat{H}}$  and normalized by the partition function  $Z$ . This is the starting point for the following sections to discuss how the Monte Carlo method works in detail.

## 2.2 Monte Carlo sampling

To explain the most important ideas of Monte Carlo algorithms we start with the basic concepts that can be found in any textbook about Monte Carlo methods or statistics (e.g. Ref. [2, 8, 18]). The expectation value  $\langle O \rangle$  of a quantity  $O$  with normalized probability density  $P(x)$  in a domain  $\Omega$  is given by

$$\langle O \rangle = \int_{\Omega} O(x)P(x) dx. \quad (2.4)$$

In case of high dimensional  $\Omega$  it is easier to draw a set  $S \subset \Omega$  of  $N$  random points in  $\Omega$  and compute the estimator

$$\bar{O} = \frac{\sum_{x \in S} O(x)P(x)}{\sum_{x \in S} P(x)}, \quad (2.5)$$

instead of evaluating the integral. In case of large  $N$  the estimator converges to the expectation value

$$\lim_{N \rightarrow \infty} \bar{O} = \langle O \rangle. \quad (2.6)$$

This procedure is often called simple sampling. Because the samples of  $S$  are drawn randomly, a lot of points  $x$  with vanishing small probability weights  $P(x)$  are considered which slow down the convergence. Reducing the number of random points with small weights and increasing the number of random points with high statistical weights is the idea of importance sampling. Therefore an additional probability density  $W(x)$  is defined to extend the fraction in Eq. (2.5). Afterwards we draw  $S$  according to  $W(x)$ . The estimator becomes

$$\bar{O} = \frac{\sum_{x \in S} O(x) \frac{P(x)}{W(x)}}{\sum_{x \in S} \frac{P(x)}{W(x)}}. \quad (2.7)$$

In principle every probability density  $W(x)$  can be used, but to maximize the speed up of convergence it should be close to  $P(x)$ . If so, points in  $\Omega$  with a large statistical weight are drawn more often than points with a very small weight. In the best case  $W(x)$  is proportional (or equal) to  $P(x)$ . In this case, the calculation of the estimator simplifies to

$$\bar{O} = \frac{1}{N} \sum_{x \in S} O(x). \quad (2.8)$$

The central limit theorem and the law of large numbers predict for the standard error of the estimator

$$\epsilon_{\bar{O}} = \sqrt{\frac{1}{N(N-1)} \sum_{x \in S} (O(x) - \bar{O})^2} \quad (2.9)$$

a scaling behavior proportional to  $1/\sqrt{N}$ , independent of the dimension of  $\Omega$ . In practice, the standard error often defines the termination criterion of the sampling process. As long as the error is not as small as requested the sampling goes on.

Unfortunately the samples that are drawn in a Monte Carlo method are often not uncorrelated as we supposed for the data analysis here. We will discuss how to deal with correlated data in Appendix B.

## 2.3 Metropolis algorithm

In practice, neither the probability density  $P(x)$  nor a function  $W(x) \propto P(x)$  are accessible for direct sampling. To use importance sampling anyway, in 1953 Metropolis et al. [20] proposed a method which uses Markov chains to generate samples according to the required probability distribution. Important improvements were made by Hastings in 1970 [21].

The idea of the Metropolis algorithm (details see below) is to use a Markov chain to draw the samples according to the required probability density  $W(x)$ . The Markov chain takes an arbitrary starting point  $x_0$  and uses it to construct the next sample  $x_1$  by a stochastic procedure. Afterwards the new sample  $x_1$  is taken to construct the following sample  $x_2$  in the same way. The Markov chain is therefore defined by its proposal distribution  $T(x_i \rightarrow x_{i+1})$ , representing the conditional probability of proposing  $x_{i+1}$  for given  $x_i$ . At the beginning,  $x_0$  belongs to an arbitrary distribution  $W^{(0)}(x)$ . Each step of the Markov chain changes the configurations,  $x_i \rightarrow x_{i+1}$ , and also the probability distribution  $W^{(i)} \rightarrow W^{(i+1)}$  the  $x$  configurations belong to, until the stationary distribution  $W$  is reached

$$W^{(0)} \xrightarrow{T} W^{(1)} \xrightarrow{T} W^{(2)} \xrightarrow{T} \dots \xrightarrow{T} W \xrightarrow{T} W \xrightarrow{T} \dots \quad (2.10)$$

The number of necessary cycles to equilibrate the distribution is called warm-up time (or burn-in time)  $N_0$ . After the Markov chain reached the stationary distribution  $W(x)$ , all configurations  $x_i$ , with  $i > N_0$  are distributed according to the probability density we want to sample. For calculating the estimator, all samples with  $i < N_0$  are ignored. A sufficient but not necessary

condition for the existence of a stationary distribution is detailed balance [22, 23]

$$W(x_{i+1})T(x_{i+1} \rightarrow x_i) = W(x_i)T(x_i \rightarrow x_{i+1}). \quad (2.11)$$

Monte Carlo methods using Markov chains without detailed balance have to prove the stationarity of the distribution in another fashion. If  $T(x_i \rightarrow x_{i+1})$  is strictly positive for any  $x_i$  and  $x_{i+1}$  the considered Markov chain update is ergodic and the stationary distribution is unique [2, 8, 22]. Ergodicity is important because it ensures that all configurations can be reached. A non-ergodic updating scheme would result in a systematic misbehavior of the entire Monte Carlo process.

In the next step we consider the Metropolis algorithm as it was generalized by Hastings [21]. In general, the Metropolis algorithm does not accept every update of the  $x$  configuration. It uses the last accepted sample (the initial sample  $x_0$  is accepted by default) and a proposal probability  $T_0(x_i \rightarrow x_{i+1})$  [8] to compute the probability of accepting the new configuration  $x_i$  by

$$p_{\text{MH}}(x_i \rightarrow x_{i+1}) = \min \left\{ 1, \frac{W(x_{i+1})T_0(x_{i+1} \rightarrow x_i)}{W(x_i)T_0(x_i \rightarrow x_{i+1})} \right\}, \quad (2.12)$$

Comparing the result with a uniformed random number between 0 and 1 accepts the update or rejects it. If an update is rejected the importance sampling process goes on and uses the old configuration again. For simulations of the partition function  $Z$  the Boltzmann weight  $e^{-\beta H(x)}$  is used as probability distribution  $W(x_i)$ . Contrary to a full integration a local evaluation of the Boltzmann weight is easy and since only the proportionality is important we do not have to care about prefactors. The total transition probability  $T(x_i \rightarrow x_{i+1}) = T_0(x_i \rightarrow x_{i+1}) p_{\text{MH}}(x_i \rightarrow x_{i+1})$  fulfills the detailed balance condition

$$\begin{aligned} W(x_i)T(x_i \rightarrow x_{i+1}) &= W(x_i) T_0(x_i \rightarrow x_{i+1}) p_{\text{MH}}(x_i \rightarrow x_{i+1}) \\ &= W(x_i) T_0(x_i \rightarrow x_{i+1}) \min \left\{ 1, \frac{W(x_{i+1})T_0(x_{i+1} \rightarrow x_i)}{W(x_i)T_0(x_i \rightarrow x_{i+1})} \right\} \\ &= \min \left\{ W(x_i)T_0(x_i \rightarrow x_{i+1}), W(x_{i+1})T_0(x_{i+1} \rightarrow x_i) \right\} \\ &= W(x_{i+1}) T_0(x_{i+1} \rightarrow x_i) \min \left\{ 1, \frac{W(x_i)T_0(x_i \rightarrow x_{i+1})}{W(x_{i+1})T_0(x_{i+1} \rightarrow x_i)} \right\} \\ &= W(x_{i+1})T(x_{i+1} \rightarrow x_i), \end{aligned} \quad (2.13)$$

due to the positivity of all factors [8].

Using a symmetric proposal probability,

$$T_0(x_{i+1} \rightarrow x_i) = T_0(x_i \rightarrow x_{i+1}), \quad (2.14)$$

together with the Boltzmann weight simplifies the Metropolis-Hastings algorithm and recovers for classical systems the original formulation by Metropolis [20] for the acceptance probability

$$p_M(x_i \rightarrow x_{i+1}) = \min \left\{ 1, \frac{e^{-\beta H(x_{i+1})}}{e^{-\beta H(x_i)}} \right\} = \min \{1, e^{-\beta \Delta E}\}, \quad (2.15)$$

with energy difference  $\Delta E = H(x_{i+1}) - H(x_i)$ .

Here we introduced the most important properties and aspects of the Metropolis algorithm and Markov chains. For a deeper discussion we refer to text books like Ref. [2, 8, 23].

## 2.4 Updating schemes

The updating scheme is one of the most important parts of a Markov chain Monte Carlo method. It determines key properties like ergodicity and detailed balance. In general, the efficiency of the whole implementation depends on an updating scheme that is well suited for the considered problem. For this work the two most important updating schemes to propose new configurations are

**Hybrid Quantum Monte Carlo (HQMC) [6, 7, 10, 24]:** HQMC uses Hamilton's equation of motion to simulate a trajectory in a continuous configuration space by molecular dynamics. If the numerical time evolution is done carefully the Metropolis check accepts all proposed updates. Because all components of the configuration field are changed simultaneously we call this a global updating scheme. The method is often also referred to as Hamilton Monte Carlo or simply Hybrid Monte Carlo (HMC).

**Blankenbecler-Scalapino-Sugar Quantum Monte Carlo (BSS-QMC) [9]:** This method assumes a discretized configuration space where each component of the configuration vector has mostly two states. It proposes updates to the Metropolis check by flipping the state of a single component. Referring to spin-1/2 states, they are called local spin flip updates.

We provide a detailed discussion about HQMC in the following chapters. Because HQMC and BSS-QMC belong to the so-called auxiliary field quantum Monte Carlo methods we will also mention commonalities and differences between the methods.





# 3

## Chapter 3

---

# Hybrid Quantum Monte Carlo method on the Hubbard model

In this chapter we discuss the concepts of the hybrid quantum Monte Carlo (HQMC) method and important steps how to implement it. The first section introduces the basic formulation of HQMC. The following sections consider its updating scheme and important properties of the algorithm, namely detailed balance, evaluation of forces, measurements of observables and how to solve the occurring system of linear equations. A discussion about ergodicity problems of the basic formulation concludes this chapter. The results of this and the following chapters, where we point out how to circumvent the ergodicity problems and apply HQMC to the SSH model, are already published by the author and can be found in Ref. [25]. For consistency and comparability we stay close to the notation of the pioneering publication by Scalettar et al. [10] we revisit here. In order to show parallels and differences between the HQMC and BSS-QMC method we mention them wherever possible.

## 3.1 Basic Formulation

The Hamilton operator  $\hat{H}$  of the Hubbard model is given by the sum of a kinetic part  $\hat{H}_K$  and an interaction part  $\hat{H}_U$ ,

$$\hat{H} = \hat{H}_K + \hat{H}_U. \quad (3.1)$$

While the tight-binding Hamiltonian,

$$\hat{H}_K = -t \sum_{\langle i,j \rangle, \sigma} \left( \hat{c}_{i,\sigma}^\dagger \hat{c}_{j,\sigma} + \hat{c}_{j,\sigma}^\dagger \hat{c}_{i,\sigma} \right), \quad (3.2)$$

represents the kinetic energy and favors extended states, the potential energy is provided by the on-site Hubbard interaction

$$\hat{H}_U = U \sum_i \left( \hat{n}_{i,\uparrow} - \frac{1}{2} \right) \left( \hat{n}_{i,\downarrow} - \frac{1}{2} \right), \quad (3.3)$$

and favors localized states. Here, the fermionic operators  $\hat{c}_{i,\sigma}^\dagger$  ( $\hat{c}_{i,\sigma}$ ) create (annihilate) an electron in a Wannier state centered at site  $i$  with  $z$ -component of the spin  $\sigma$ . Nearest neighbors of the underlying lattice are denoted by  $\langle i, j \rangle$ . The hopping element is given by  $t$ ,  $U$  denotes the strength of the Hubbard interaction and  $\hat{n}_{i,\sigma} = \hat{c}_{i,\sigma}^\dagger \hat{c}_{i,\sigma}$ . To compute the partition function, which is the quantity of interest for any thermodynamical property, we discretize the imaginary time  $\tau$  by a Trotter decomposition

$$Z = \text{Tr} e^{-\beta \hat{H}} = \text{Tr} \left( e^{-\Delta\tau \hat{H}} \right)^{N_\tau} \simeq \text{Tr} \left( e^{-\Delta\tau \hat{H}_K} e^{-\Delta\tau \hat{H}_U} \right)^{N_\tau}. \quad (3.4)$$

Where  $N_\tau \Delta\tau = \beta$ . A detailed discussion of the Trotter decomposition is provided in Appendix A. The discretization into  $N_\tau$  slices is common for the HQMC as well as for the BSS-QMC method. It is important to point out that both methods share the same  $\Delta\tau$  discretization error. Especially in view of comparability this is an important property. To integrate out all fermions, it is necessary to decouple the many body interaction term into a sum of single body propagators. This is done by a Hubbard-Stratonovich (HS) decomposition. It introduces an auxiliary field  $x_{i,l}$  at each site  $i$  and at every time slice  $l$ ,

$$\begin{aligned} & \exp \left[ -\Delta\tau U \left( \hat{n}_{i,\uparrow} - \frac{1}{2} \right) \left( \hat{n}_{i,\downarrow} - \frac{1}{2} \right) \right] = \\ & = \left( \frac{\Delta\tau}{\pi} \right)^{1/2} e^{-\Delta\tau U/4} \int_{-\infty}^{\infty} dx_{i,l} \exp \left\{ -\Delta\tau \left[ x_{i,l}^2 + \sqrt{2U} x_{i,l} \left( \hat{n}_{i,\uparrow} - \hat{n}_{i,\downarrow} \right) \right] \right\}. \end{aligned} \quad (3.5)$$

While the corresponding fields in the BSS-QMC algorithm are discrete, here the  $x_{i,l}$  fields used for HQMC are continuous. Note that because the physical behavior is independent of constant prefactors in the partition function we will drop them subsequently. After an integration over the

fermionic degrees of freedom the partition function reads

$$Z = \int [\delta x] e^{-S_B(x)} \det M_\uparrow(x) \det M_\downarrow(x), \quad (3.6)$$

where

$$S_B(x) := \Delta\tau \sum_{i,l} x_{i,l}^2. \quad (3.7)$$

The matrices  $M_\sigma(x)$  possess the block structure

$$M_\sigma(x) = \begin{pmatrix} \mathbb{1} & 0 & 0 & \cdots & 0 & B_{N_\tau,\sigma}(x) \\ -B_{1,\sigma}(x) & \mathbb{1} & 0 & \cdots & 0 & 0 \\ 0 & -B_{2,\sigma}(x) & \mathbb{1} & \cdots & 0 & 0 \\ \vdots & \vdots & \vdots & \ddots & \vdots & \vdots \\ 0 & 0 & 0 & \cdots & \mathbb{1} & 0 \\ 0 & 0 & 0 & \cdots & -B_{N_\tau-1,\sigma}(x) & \mathbb{1} \end{pmatrix}. \quad (3.8)$$

The size of each block matrix is equal to  $V_S \times V_S$ , determined by the number of lattice sites  $V_S$ . While the diagonal elements of  $M_\sigma(x)$  are given by the identity matrix  $\mathbb{1}$ , the off-diagonal block matrices are in form of

$$B_{l,\sigma}(x) = e^{-\Delta\tau K} e^{-\sigma\Delta\tau V_l(x)}. \quad (3.9)$$

Here,  $K$  represents the tight-binding hopping matrix given by its components

$$K_{i,j} = \begin{cases} -t & \langle i, j \rangle \text{ nearest neighbors,} \\ 0 & \text{otherwise.} \end{cases} \quad (3.10)$$

$V_l$  is a diagonal matrix containing the auxiliary fields

$$[V_l(x)]_{i,j} = \delta_{i,j} \sqrt{2U} x_{i,l}. \quad (3.11)$$

As a side note, while HQMC involves  $M_\sigma(x)$  itself the BSS-QMC method makes use of another representation for the determinant,

$$\det M_\sigma(x) = \det \left( \mathbb{1} + \prod_{l=1}^{N_\tau} B_{l,\sigma}(x) \right). \quad (3.12)$$

We will reveal the background later.

At this point we can take a closer look at the partition function we obtained in Eq. (3.6) and discuss the absence of the fermionic sign problem. Therefore we have to consider half filling and a bipartite lattice. Lattices are bipartite if two subsets can be distinguished in the way that neighboring lattice sites always belong to different subsets. Half filling together with bipartiteness allows a particle-hole transformation to prove

$$\det M_{\downarrow}(x) = e^{-\Delta\tau\sqrt{2U}\sum_{i,l}x_{i,l}} \det M_{\uparrow}(x), \quad (3.13)$$

which means both determinants always have the same sign and all auxiliary field configurations have a positive statistical weight [26]. Doping the model away from half filling, by introducing a finite chemical potential  $\mu$ , or simulating a non-bipartite lattice would destroy this symmetry and generate a sign problem. Figuratively speaking, this means the function we want to integrate takes positive and negative values which partially cancel each other and the whole sampling process slows down. Especially for low temperatures and large lattice sizes the number of required samples grows exponentially due to the NP-hardness of the sign problem [27]. If the sign problem is present, it strongly limits the application of Monte Carlo algorithms. Therefore we remain for our discussion at half filling,  $\mu = 0$ , and on bipartite square lattices with periodic boundary conditions. For a more detailed discussion how the sign problem can be handled we refer to e.g. Ref. [28].

In contrast to the BSS-QMC method and to achieve a good scaling of the HQMC method, the determinants in Eq. (3.6) are substituted. Because of the large numerical effort that is required to calculate a determinant the HQMC method samples them stochastically. Therefore, we have to introduce so-called pseudo fermion fields  $\phi_{\sigma}$  by performing a Gaussian integration,

$$\sqrt{\det(2\pi M_{\sigma}(x))} = \int_{-\infty}^{\infty} d\phi_{\sigma} e^{-\frac{1}{2}\phi_{\sigma}^T M_{\sigma}^{-1}(x)\phi_{\sigma}}, \quad (3.14)$$

and get

$$Z = \int [\delta x \delta\phi_{\uparrow} \delta\phi_{\downarrow}] e^{-S_B(x) - \sum_{\sigma} \phi_{\sigma}^T (M_{\sigma}^T(x) M_{\sigma}(x))^{-1} \phi_{\sigma}}. \quad (3.15)$$

This step implicitly assumes the absence of negative weights,  $\det M_{\uparrow}(x) \det M_{\downarrow}(x) > 0$ .

We have now achieved a state where the partition function can be sampled by a Monte Carlo process to determine the physical properties of the model. The next step is the elaboration of an effective updating scheme.

Except for using continuous auxiliary fields and the pseudo fermion representation the general

procedure, and most of the properties, are equivalent for the BSS-QMC method.

### 3.2 The Hybrid Monte Carlo updating scheme

In this section we take a closer look at how the hybrid quantum Monte Carlo algorithm generates its samples. The discussion is based on the description of Markov chain Monte Carlo methods in Chapter 2. Here we start with the principles and continue in the following section with some details of our implementation.

The first aim is to rewrite the exponent so it becomes similar to a Hamilton function. Therefor we add an additional field to the partition function. With respect to the HS field  $x_{i,l}$ , we introduce a canonical conjugated variable  $p_{i,l}$  such that Eq. (3.15) becomes

$$Z = \int [\delta x \delta p \delta \phi_{\uparrow} \delta \phi_{\downarrow}] P(x, p, \phi_{\uparrow}, \phi_{\downarrow}). \quad (3.16)$$

The distribution function we use,

$$P(x, p, \phi_{\uparrow}, \phi_{\downarrow}) = e^{-\mathcal{H}(x, p, \phi_{\uparrow}, \phi_{\downarrow})}, \quad (3.17)$$

contains the Hamilton function defined by

$$\mathcal{H}(x, p, \phi_{\uparrow}, \phi_{\downarrow}) := S_B(x) + \sum_{i,l} p_{i,l}^2 + \sum_{\sigma} \phi_{\sigma}^T \left( M_{\sigma}^T(x) M_{\sigma}(x) \right)^{-1} \phi_{\sigma}. \quad (3.18)$$

Interpreting the  $x$  fields in terms of a position vector, the  $p$  fields play the role of the according momentum vector in a potential determined by  $\phi_{\uparrow}$  and  $\phi_{\downarrow}$ . The HQMC algorithm has to draw samples of  $P(x, p, \phi_{\uparrow}, \phi_{\downarrow})$  on a state space which is spanned by a set of continuous fields  $\{x, p, \phi_{\uparrow}, \phi_{\downarrow}\}$ . Only the momentum fields  $p$  can be sampled directly because they are Gaussian distributed. Sampling of the other fields requires some more effort. To sample the pseudo fermion fields  $\phi_{\sigma}$  we introduce the auxiliary variable

$$R_{\sigma} := \left( M_{\sigma}^T(x) \right)^{-1} \phi_{\sigma}, \quad (3.19)$$

which can be drawn from a Gaussian distribution. Afterwards, a matrix-vector multiplication yields the required sample of  $\phi_{\sigma}$  by

$$\phi_{\sigma} = M_{\sigma}^T(x) R_{\sigma}. \quad (3.20)$$

The most difficult part of the HQMC algorithm is the efficient sampling of the HS fields  $x$ . Therefore, the algorithm uses Hamilton's equations of motion, according to the Hamilton function in Eq. (3.18). At fixed values of the pseudo fermions, Hamilton's equations of motion are

$$\dot{p}_{i,l} = -\frac{\partial \mathcal{H}}{\partial x_{i,l}} \quad (3.21)$$

$$\dot{x}_{i,l} = \frac{\partial \mathcal{H}}{\partial p_{i,l}}. \quad (3.22)$$

The phase space is spanned by the HS field and its canonical conjugated momentum field. Starting at a given point  $(x, p)$  and evolving the system by a time integration leads to a new point  $(x', p')$  in the phase space. The new sample is accepted or rejected, according to the Metropolis-Hastings rule

$$\begin{aligned} r_{\text{MH}}((x, p) \rightarrow (x', p')) &= \min \left\{ 1, \frac{T_0((x', p') \rightarrow (x, p)) P(x', p', \phi)}{T_0((x, p) \rightarrow (x', p')) P(x, p, \phi)} \right\} \\ &= \min \left\{ 1, e^{\mathcal{H}(x, p, \phi) - \mathcal{H}(x', p', \phi)} \right\}. \end{aligned} \quad (3.23)$$

Here  $T_0$  corresponds to the proposal probability density which we choose symmetrically (see Sec. 2.3 and Sec. 3.3). To decide whether the new configuration is accepted or rejected, the method compares  $r_{\text{MH}}((x, p) \rightarrow (x', p'))$  with a uniformed random number between 0 and 1. For any Hamiltonian propagation that is done exactly, the acceptance is unity. Nevertheless it is important to notice the extensive character of the energy difference in the exponent of the Metropolis-Hasting rule. To achieve high acceptance the energy difference has to stay small. Later on we will discuss its relevance to scaling.

Summarizing, the HQMC updating scheme consists of three steps:

1. draw Gaussian samples for  $p$  and  $R$ ,
2. evolve  $x$  and  $p$  according to Hamilton's equations of motions,
3. accept or reject the new values of  $x$  and  $p$  according to the Metropolis-Hastings ratio.

Except for the  $S_{\text{B}}(x)$  term the  $p$  and  $R$  fields determine the artificial energy at the beginning of the time evolution. That is why the sampling of  $p$  and  $R$  is also named heat bath updates. Monitoring the artificial energy shows how it saturates until the Markov Chain reaches its stationary distribution after the warm-up time (see Sec. 2.3).

Note, the update scheme of the BSS-QMC method is much simpler. It uses local spin flip updates to generate new configurations of the auxiliary field. This means the flip of a single auxiliary field component is accepted or rejected by a Metropolis check. For details about the spin flip updates and efficient implementations we refer to Ref. [14].

### 3.3 The right choice of the integrator

This section addresses the details of the time integration for the Hamiltonian motion, in this context often also referred to as molecular dynamics. We have to take care and preserve two important properties of Hamilton's equations of motion. First, as we know from Liouville's theorem, the phase space volume has to be conserved, and secondly, the equations are time reversal symmetric. Every chosen integrator that fulfills these conditions guarantees that the proposal probability is symmetric, i.e.  $T_0((x, p) \rightarrow (x', p')) = T_0((x', p') \rightarrow (x, p))$  [23]. Integration methods with these essential traits are called symplectic integrators [29]. The most well known representative of them is the Leapfrog method. It satisfies the time reversibility and is due to its efficiency well established in numerics. The Leapfrog method solves the equation of motion iteratively over an artificial time, which is discretized into time steps intervals  $\Delta t$ . Note, this discretization can be interpreted as a symmetric Trotter decomposition [30].

Initially, the Leapfrog starts by evolving the momentum field by a time  $\Delta t/2$  while keeping the auxiliary fields fixed. Afterwards, it propagates the auxiliary field

$$x_{i,l}(t + \Delta t) - x_{i,l}(t) = \int_t^{t+\Delta t} dt' 2p_{i,l}(t') = 2p_{i,l}\left(t + \frac{1}{2}\Delta t\right)\Delta t + \mathcal{O}(\Delta t^3) \quad (3.24)$$

and the momentum field

$$p_{i,l}\left(t + \frac{3}{2}\Delta t\right) - p_{i,l}\left(t + \frac{1}{2}\Delta t\right) = - \int_{t+1/2\Delta t}^{t+3/2\Delta t} dt' \frac{\partial \mathcal{H}(x, t')}{\partial x_{i,l}} = - \frac{\partial \mathcal{H}(x, t + \Delta t)}{\partial x_{i,l}} \Delta t + \mathcal{O}(\Delta t^3) \quad (3.25)$$

by a time-step size  $\Delta t$  in alternating fashion until it reaches the stopping time, for example  $1/\Delta t$ . Regardless of the choice of the numerical integrator, we have to control its systematical error. In the case of HQMC we perform a Metropolis check, as discussed above, after the Leapfrog method to validate the new auxiliary field configuration. It compares the artificial energy of the system before and after the Leapfrog propagation and rejects the proposed update if the differences are too large. This procedure ensures detailed balance which is important for every Markov chain

Monte Carlo method (see Sec. 2.3). As side effect the Metropolis check controls the systematical errors of the Leapfrog method and the implied conjugate gradient method to evaluate the forces (see Sec. 3.4 and 3.5). The acceptance rate depends on the time-step size  $\Delta t$  and the precision of the conjugate gradient method, as studied in Ref. [7]. We made the experience that configurations in the phase space where the (scalar) product of the gradient of the potential times the velocity in the according direction is large compared to the Leapfrog time-step size,

$$\frac{\nabla V(x) \cdot \dot{x}}{|\dot{x}|^2} \gg \Delta t, \quad (3.26)$$

has low probability to be accepted. Therefore, another Leapfrog run with another sample of momentum and pseudo fermion fields but the same auxiliary field configuration may have much better propensity to produce an acceptable configuration. If several Leapfrog runs fail, the time-step size has to be made smaller.

As a conceivable way out, we implemented the adaptive Leapfrog method [31]. It is also time reversible but selects the time-step size according to the gradient of the potential,  $\Delta t \propto 1/|\nabla H|^2$ . Summarizing our experience with this integrator, we achieved very good acceptance, but as soon as a single badly conditioned configuration occurs, it slows down to very small step sizes in order to solve the equation of motion with the required precision in regions of high variability. This behavior results in an increase of computing time for the whole update. Very likely, these regions correspond to regions that we will discuss in Sec. 3.6, where determinants change signs and the symplectic integrator has to fight against singularities in the gradient of the potential. Meanwhile, Leapfrog runs with a fixed time-step size may fail a couple of times trying to integrate the badly conditioned configuration, but if the step size is not too large they also end up with an accepted configuration. In many cases the multiple trials of the fixed step-size Leapfrog method took less computing time compared to the adaptive version to overcome a badly conditioned configuration. A further way to improve the acceptance is the substitution of a single long Leapfrog run by several shorter runs. If the integration time is still long enough to move the system a sufficient distance away from the initial configuration in the phase space, the side effect of reduced correlations may be found. We attribute this effect to the additional sampling of  $\phi_\sigma$  and  $p_\sigma$  fields between measurements. For larger system sizes or larger values of  $\beta$  the acceptance can drop down, what requires to reduce  $\Delta t$  in order to preserve a high acceptance ratio. Finally, the optimal step size  $\Delta t$  depends on system size, temperature, physical parameters and the simulated physical model in general. The easiest way to adjust the step size is to monitor the acceptance ratio. If most of the updates are rejected the step size has to be shortened until the acceptance ratio raises.



### 3.4 How to evaluate the forces and measure observables

As mentioned above, the generation of new samples is the numerically expensive part of the algorithm. In particular, the evaluation of the force terms, required by the Leapfrog method, needs most of the computing time. To evaluate the derivative of the potential, we can make use of an algebraic identity as well as of the symmetry of  $M_\sigma^\top M_\sigma$  to simplify

$$\begin{aligned} \frac{\partial}{\partial x_{i,l}} \phi_\sigma^\top \left( M_\sigma^\top(x) M_\sigma(x) \right)^{-1} \phi_\sigma &= \\ &= -2 \phi_\sigma^\top \left( M_\sigma^\top(x) M_\sigma(x) \right)^{-1} \left[ M_\sigma^\top(x) \left( \frac{\partial}{\partial x_{i,l}} M_\sigma(x) \right) \right] \left( M_\sigma^\top(x) M_\sigma(x) \right)^{-1} \phi_\sigma. \end{aligned} \quad (3.27)$$

At this point it is very easy to point out the reason for the numerical effort:  $(M_\sigma^\top(x) M_\sigma(x))^{-1}$  is hard to calculate. Although  $M_\sigma(x)$  is a sparse matrix with a clear structure, its inverse is dense and, due to bad scaling, a straightforward numerical inversion can only be the last resort.

A closer look at Eq. (3.27) reveals a way out. We do not need to know the inverse matrix itself. It is enough to know the result of its product with the vector  $\phi_\sigma$ . In other words, instead of inverting the matrix to evaluate the forces it is sufficient to solve a system of linear equations that is given by

$$M_\sigma^\top(x) M_\sigma(x) X_\sigma = \phi_\sigma. \quad (3.28)$$

Fortunately, the numerical effort to find  $X_\sigma$ , or a very good approximation of it, is numerically manageable.

However, the inverse of  $M_\sigma(x)$  appears also in another part of the algorithm. A measurement of observables can be performed after each Leapfrog run. The most important observable is the bare one-particle Green's function

$$G_\sigma(i-j, \tau - \tau') = G_\sigma((i, \tau), (j, \tau')) = \begin{cases} \langle \hat{c}_{\sigma,(i,\tau)} \hat{c}_{\sigma,(j,\tau')}^\dagger \rangle & \tau \geq \tau' \\ -\langle \hat{c}_{\sigma,(j,\tau')}^\dagger \hat{c}_{\sigma,(i,\tau)} \rangle & \tau < \tau' \end{cases}, \quad (3.29)$$

which is equal to  $[M_\sigma^{-1}(x)]_{(i,\tau),(j,\tau')}$  [10, 28]. Wick's theorem allows to reduce any many-particle observable to a linear combination of the one-particle Green's function [28]. Hence, it is the corner stone for all measurements of electron quantities. To avoid a numerical expensive straightforward inversion of  $M_\sigma(x)$ , the HQMC method can be implemented by using a stochastic inversion, which also reduces the inversion problem to a system of linear equations. In detail, the method has to sample  $2[(M_\sigma^\top(x) M_\sigma(x))^{-1} \phi_\sigma]_i [R_\sigma]_j$  as an unbiased estimator for each component  $[M_\sigma^{-1}(x)]_{i,j}$ .

This can be seen from combining Eq. (3.20), where the pseudo fermion field is sampled by the auxiliary variable  $R_\sigma$ , with the system of linear equations in Eq. (3.28). Performing the outer product leads to

$$X_\sigma R_\sigma^T = \left[ \left( M_\sigma^T(x) M_\sigma(x) \right)^{-1} \phi_\sigma \right] R_\sigma^T = M_\sigma^{-1}(x) \left( M_\sigma^T(x) \right)^{-1} M_\sigma^T(x) R_\sigma R_\sigma^T = M_\sigma^{-1}(x) R_\sigma R_\sigma^T. \quad (3.30)$$

Because  $R_\sigma$  is generated according to  $e^{-R_\sigma^T R_\sigma}$ , its second statistical momentum has to be equal to the variance of its probability distribution

$$\langle [R_\sigma]_i [R_\sigma]_j \rangle = \frac{1}{2} \delta_{i,j}, \quad (3.31)$$

so we can justify the unbiased estimator because of

$$2 \langle X_\sigma R_\sigma^T \rangle = M_\sigma^{-1}(x). \quad (3.32)$$

A disadvantage of the stochastic inversion is the introduction of additional stochastic noise to our measurements. In contrast, the BSS-QMC method uses a direct inversion because the numerical effort is the same as to compute the determinants in Eq. (3.12) which are required during the update procedure [28, 14].

### 3.5 Solution of linear systems with the conjugate gradient method

In the section above, we showed that a quick solver for systems of linear equations is required millions of times in every hybrid quantum Monte Carlo simulation. In this section we will discuss this step in more detail by taking the example of the Hubbard model. To simplify the notation and enhance readability the spin index  $\sigma$  is suppressed in this section. The physical spin up and spin down sectors are treated in exactly the same way. A textbook Gaussian elimination takes  $\mathcal{O}(N^3)$  flops to solve a system of  $N \times N$  linear equations. In contrast to the cubic scaling of a direct inversion, iterative solvers can be used to find the required solution in a fraction of the time. For sparse matrices, like here, the computing effort can shrink up to a linear growth with the  $\mathcal{O}(N)$  entries of the matrix. Several iterative solvers are available. Due to the structure and symmetry of  $(M^T(x)M(x))$  the conjugate gradient (CG) method is a well suited choice to solve the corresponding system of linear equations. It is a well established method and belongs to the textbook examples of iterative solvers. For a modern and detailed introduction to iterative solvers we refer to the literature like Ref. [32]. Note, as for the introduction of the pseudo fermions we

can assume  $O = M^T(x)M(x)$  to be positive definite for the discussion of the CG method. The absence of auxiliary field configurations  $x$  that would lead to a positive semi-definite matrix  $O$  is discussed in Sec. 3.6.

We will explain the CG method on a prototypical system

$$OX = \phi, \tag{3.33}$$

where  $O = M^T(x)M(x)$  is symmetric positive definite. The solution of Eq. (3.33) is also the unique minimum of the quadratic function

$$f(X) = \frac{1}{2}X^T OX - X^T \phi. \tag{3.34}$$

Like all iterative solvers, the CG method starts with an initial guess  $X_0$  and improves it stepwise. The key idea of the CG method is not to evaluate the direct gradient at each point to use it as search direction. Instead, the CG method selects that search direction which is orthogonal, with respect to the scalar product induced by  $O$ , to all previously used search directions. Summarizing this idea gives this iterative prescription:

$$\begin{aligned} X_{n+1} &= X_n + \zeta_n d_n \\ r_{n+1} &= r_n - \zeta_n O d_n \\ \eta_n &= \langle r_{n+1}, r_{n+1} \rangle / \langle r_n, r_n \rangle \\ d_{n+1} &= r_{n+1} + \eta_n d_n \\ \zeta_{n+1} &= \langle r_{n+1}, r_{n+1} \rangle / \langle d_{n+1}, O d_{n+1} \rangle. \end{aligned} \tag{3.35}$$

Here  $X_n$  represents the approximation to the solution  $X$  after  $n$  steps of iterations. The corresponding residual is given by

$$r_n = \phi - OX_n. \tag{3.36}$$

Its norm can be used as a measure of how close the iterative solution is to the exact solution. To define a termination criterion we use the residual vector and stop the CG method if the actual solution fulfills

$$\varepsilon_n = \sqrt{\frac{(\phi - OX_n)^2}{\phi^2}} \leq 10^{-7}, \tag{3.37}$$

similar to the criterion used in Ref. [10]. Scalar products between vectors  $r$  and  $d$  are written as  $\langle r, d \rangle$ . If nothing is known, a vector of zeros, or any other arbitrary vector, can be used as initial guess  $X_0$ . Nevertheless, a well designed initial guess can lower the number of iterations necessary

to reach the required precision and thereby speed up the whole algorithm. For a chosen  $X_0$

$$\begin{aligned} r_0 &= \phi - OX_0 \\ d_0 &= r_0 \end{aligned} \tag{3.38}$$

completes the initial data. Because it is possible to show that

$$\langle d_m, Od_n \rangle = 0 \quad \text{for } m \neq n, \tag{3.39}$$

all search directions  $d_n$  are linearly independent, with respect to  $O$ . Hence, an arithmetically exact implementation would deliver the exact solution after  $N$  iterations. Besides a well suited initial guess, the CG method can be improved by using a preconditioner, like the authors in Ref. [10] mention. It is known that the efficiency of the CG method depends on the condition number of the matrix, which grows for stronger interaction strengths  $U$  and larger values of  $\beta$  [33]. The improvement of the condition number, and thus an acceleration of the iterative solver, is the idea behind preconditioning. A suitable preconditioner is given by a matrix  $\tilde{O}$  which is close to the matrix  $O$  and easy to invert. In best case  $\tilde{O}^{-1}O \simeq \mathbf{1}$ . For symmetric and positive definite matrices a Cholesky decomposition of  $\tilde{O}$ ,

$$\tilde{O} = L^T L, \tag{3.40}$$

is often a good starting point. It uses triangular matrices  $L$ , which are easy to invert. Although a slightly different preconditioner is used to speed up the Hubbard model, we will use the Cholesky decomposition to illustrate the idea and functional principle of a preconditioner. We define

$$\begin{aligned} O' &= (L^T)^{-1} O L^{-1} \\ X' &= LX \\ \phi' &= (L^T)^{-1} \phi, \end{aligned} \tag{3.41}$$

and rewrite Eq. (3.33) to obtain

$$O'X' = \phi', \tag{3.42}$$

which leads to

$$r'_n = \phi' - O'X'_n = (L^T)^{-1} r_n. \tag{3.43}$$

Because  $O'$  is a symmetric positive definite matrix, by definition the CG method can be used to solve the modified system of linear equations in Eq. (3.42). Modifying the iteration scheme results

in a description for an arbitrary preconditioner matrix  $\tilde{O}$ :

$$\begin{aligned}
X_{n+1} &= X_n + \zeta'_n d_n \\
r_{n+1} &= r_n - \zeta'_n O d_n \\
\eta'_n &= \langle r_{n+1}, \tilde{O}^{-1} r_{n+1} \rangle / \langle r_n, \tilde{O}^{-1} r_n \rangle \\
d_{n+1} &= r_{n+1} + \eta'_n d_n \\
\zeta'_{n+1} &= \langle r_{n+1}, \tilde{O}^{-1} r_{n+1} \rangle / \langle d_{n+1}, O d_{n+1} \rangle.
\end{aligned} \tag{3.44}$$

In theory, a Cholesky decomposition can be a good choice as preconditioner. In practice, the numerical effort to calculate it denies this idea. An exact Cholesky decomposition is as expensive as a direct inversion of the initial matrix. Therefore, the authors of Ref. [10] advise to use an incomplete Cholesky decomposition, by neglecting the hopping matrix of the electrons and slightly shifting the diagonal elements of  $(M^T(x)M(x))$ . According to them, the matrix that has to be decomposed is given by

$$\tilde{O}_0 = \begin{pmatrix} \alpha \mathbb{1} + B_{0,1}^2 & -B_{0,1} & 0 & \cdots & 0 & B_{0,N_\tau} \\ -B_{0,1} & \alpha \mathbb{1} + B_{0,2}^2 & -B_{0,2} & \cdots & 0 & 0 \\ 0 & -B_{0,2} & \alpha \mathbb{1} + B_{0,3}^2 & \cdots & 0 & 0 \\ \vdots & \vdots & \vdots & \ddots & \vdots & \vdots \\ 0 & 0 & 0 & \cdots & \alpha \mathbb{1} + B_{0,N_\tau-1}^2 & -B_{0,N_\tau-1} \\ B_{0,N_\tau} & 0 & 0 & \cdots & -B_{0,N_\tau-1} & \alpha \mathbb{1} + B_{0,N_\tau}^2 \end{pmatrix} \tag{3.45}$$

with diagonal block matrices  $B_{0,l}$ . The slight shift, e.g.  $\alpha = 1.05$ , is necessary to prevent the matrix to become ill conditioned and prevent a pivot breakdown of the CG method, as discussed in Ref. [34]. However, the preconditioner matrix Eq. (3.45) is not analytically invertible for  $\alpha \neq 1$  [10]. In general, an incomplete Cholesky decomposition partitions the preconditioner matrix into

$$\tilde{O}' = L^T D L, \tag{3.46}$$

with diagonal matrix

$$D = \begin{pmatrix} D_1 & 0 & 0 & \cdots & 0 & 0 \\ 0 & D_2 & 0 & \cdots & 0 & 0 \\ 0 & 0 & D_3 & \cdots & 0 & 0 \\ \vdots & \vdots & \vdots & \ddots & \vdots & \vdots \\ 0 & 0 & 0 & \cdots & D_{N_\tau-1} & 0 \\ 0 & 0 & 0 & \cdots & 0 & D_{N_\tau} \end{pmatrix}, \tag{3.47}$$

as well as upper triangular matrix

$$L = \begin{pmatrix} \mathbb{1} & -L_1 & 0 & \cdots & 0 & L_{N_\tau} \\ 0 & \mathbb{1} & -L_2 & \cdots & 0 & 0 \\ 0 & 0 & \mathbb{1} & \cdots & 0 & 0 \\ \vdots & \vdots & \vdots & \ddots & \vdots & \vdots \\ 0 & 0 & 0 & \cdots & \mathbb{1} & -L_{N_\tau-1} \\ 0 & 0 & 0 & \cdots & 0 & \mathbb{1} \end{pmatrix}. \quad (3.48)$$

In the atomic limit (no hopping) they consist of diagonal block matrices of size  $V_S \times V_S$ . The numerical effort is minimized by using a recursive definition to determine the block matrices

$$\begin{aligned} L_l &= D_l^{-1} B_{0,l} \\ D_l &= \alpha \mathbb{1} + B_{0,l}^2 - B_{0,l-1} D_{l-1}^{-1} B_{0,l-1}, \end{aligned} \quad (3.49)$$

while for the border,  $l = N_\tau$ , holds

$$\begin{aligned} L_{N_\tau} &= D_1 B_{0,N_\tau} \\ D_{N_\tau} &= \alpha \mathbb{1} + B_{0,N_\tau}^2 - B_{0,N_\tau-1} D_{N_\tau-1}^{-1} B_{0,N_\tau-1} - B_{0,N_\tau} D_1^{-1} B_{0,N_\tau}. \end{aligned} \quad (3.50)$$

Now we have prepared the ground to use an incomplete Cholesky decomposition within the preconditioned CG method as described above. It remains the discussion, if this is the best possible preconditioner for our purpose. Unfortunately this question is not easy to answer precisely. Here, we want to refer to the arguments of Scalettar et al. [10] who observe a dependency of the condition number, and implicitly the number of iterations, on the interaction strength  $U$  and the ongoing search for a better preconditioner. The only progress we are aware of can be found in [34] for systems with very strong interactions and for randomly generated configurations of the auxiliary field. However, the condition number of a warmed up Monte Carlo system is not necessarily comparable with those of random configurations.

Of course, the CG method belongs to the first iterative numerical solvers, but in tests with other methods like BiCGstab or GMRES the CG method turned out to be the most stable and most efficient implementation to solve the required system of linear equations. Also various attempts to construct another preconditioner by ourselves failed. In most of the cases the reason can be found in the band structure of the matrix  $M$ . Many ideas to construct another preconditioner need at least at one point something like the product of the  $B_l$  block matrices, like in the alternative representation of the fermionic determinant in Eq. (3.12). For large  $\beta$ , where a preconditioner becomes most important, the evaluation of this product is numerical unstable. The BSS-QMC

method which relies on this product has to perform a numerically expensive stabilization [14]. In the case of a preconditioner, used to speed up an iterative solver, the numerical price of a stabilization is inappropriately high. Consequently, most of the approaches to define a new preconditioner slow down the solver or the solver fails completely. The results for different solvers are comparable. A discussion of the structure of the eigenvalues can be found in Ref. [33].

Recently, some progress in developing a different type of solver for usage in HQMC was published [35]. Unfortunately, it offers no better scaling and requires more computing memory compared to the CG method. Therefore, the (preconditioned) conjugate gradient was the method of choice for all simulations in this work.

## 3.6 Ergodicity

Most of the method and implementation details in the previous section were already discussed in the original paper by Scalettar et al. [10]. We reimplemented the hybrid quantum Monte Carlo method and performed systematic simulations of varying system sizes for different physical parameters. Let us recall, we can regard the integrand of the partition function in Eq. (3.6) as the probability density the update scheme has to sample and both determinants always have the same sign according to Eq. (3.13). At high temperatures the method works well and the Monte Carlo samples are strongly dominated by auxiliary field configurations with positive determinants. For increasing  $\beta$  the configuration space becomes much more fractionalized into  $(+, +)$  (sign  $\det(M_\sigma) = 1$ ) and  $(-, -)$  (sign  $\det(M_\sigma) = -1$ ) domains. Since the determinants are real continuous functions of the continuous auxiliary field  $x$  every  $(+, +)$  domain is separated from the neighboring  $(-, -)$  domain by a hypersurface with  $\det(M_\sigma) = 0$ . This has important consequences for the sampling procedure. A matrix with vanishing determinant can not be inverted. Translated to the phase space of the Leapfrog this corresponds to a diverging potential energy on the hypersurface of vanishing determinants. Furthermore, also the force terms are diverging, trying to push the system away from the barrier. Fig. 3.1 shows a two dimensional scan in a section of the configuration space. We performed brute force calculations of the determinant in its representation of Eq. (3.12) to visualize the barrier for a given configuration. The logarithmic plot corresponds to the energy landscape the Leapfrog has to pass through.

Because the symplectic integrator is chosen to conserve energy the Leapfrog method will in principle not be able to cross a barrier [36]. In particular, in every fractionalized configuration space, each molecular dynamics run will be trapped in the pocket of its initial point. Because the sign of the determinant is a property of the matrix itself, updates of momentum or pseudo fermion

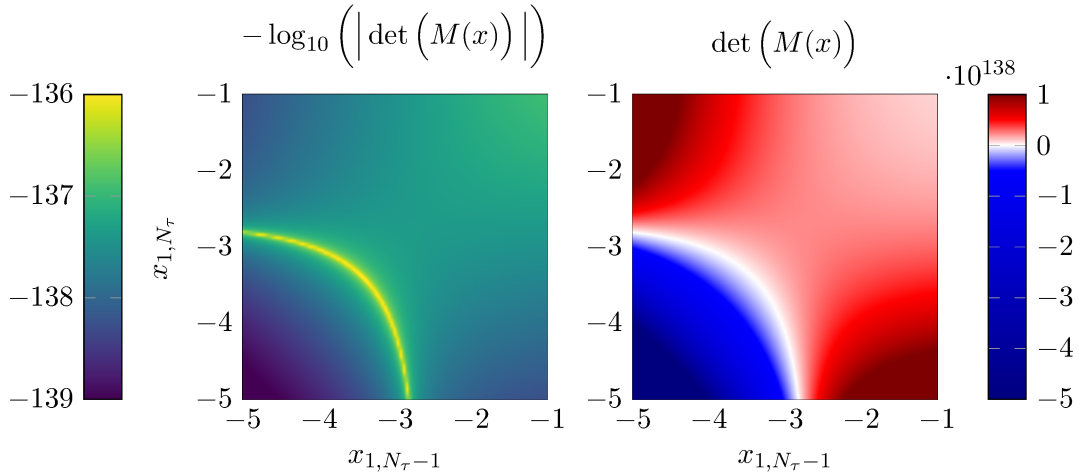


**Figure 3.1:** Scans in the configuration space, calculated by evaluation of the determinant in two dimensions, visualize the existing borders on a  $8 \times 8$  lattice with  $\beta = 8.0$ ,  $N_\tau = 80$  and  $U = 0.5$ . The left plot shows the logarithmized determinant that is equivalent to the configuration space the HQMC method has to sample. The second plot shows the determinant itself. It shows how the zero modes separate the configuration space in areas of positive and negative signs.

fields can not cross that barrier either. This means the whole Monte Carlo simulation is not ergodic. The consequences are arbitrary wrong results. Fig. 3.2 shows the randomness of observing a allegedly good or a totally wrong result, depending on the arbitrarily chosen starting point, or rather the corresponding pocket. While the configuration starting in a  $(+, +)$  pocket delivers results close the correct solution, the second run, starting in a  $(-, -)$  domain results in totally wrong physics. Due to its discrete auxiliary fields, the BSS-QMC method does not suffer from ergodicity problems and can be used for benchmark results.

A justified question is whether different integration techniques encounter the barriers in a different manner. A simple Leapfrog integrator could cross a barrier for sufficient large step size, but the Metropolis check afterwards will most likely reject the new configuration. Same applies for other ideas like Langevin dynamics [36]. In contrast, the adaptive integrator [31] recognizes the increasing forces close to the barrier and reacts by decreasing its step size to a vanishing small value. It is unable to cross the potential barrier but slows down the whole simulation indefinitely by trying to integrate Hamilton's equation of motion in a diverging energy landscape.



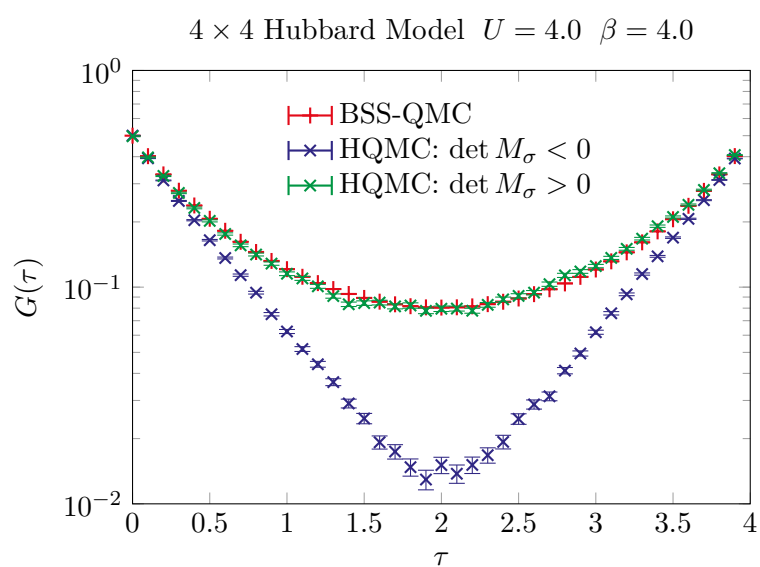


**Figure 3.2:** Green's functions, calculated with the hybrid quantum Monte Carlo method and the BSS-QMC [14] algorithms on a  $4 \times 4$ -lattice at  $U = 4$  and  $\Delta\tau = 0.1$ . Starting the simulation in different sectors clearly produces different results.



# 4 Chapter 4

---

## Complex Hybrid Quantum Monte Carlo method for the Hubbard model

In the previous chapter we discussed the initial formulation of the hybrid quantum Monte Carlo method with real auxiliary fields. At the end we illustrated ergodicity problems which we attempt to solve in this chapter.

Several routes promise to circumvent the ergodicity problem of the algorithm using real auxiliary fields. Some suitable transformations could be found to eliminate the potential barriers or the Leapfrog could be modified to enable tunneling between the pockets [36]. A combination of the importance sampling scheme of the BSS algorithm with the HQMC method was discussed in Ref. [37] and has the potential to solve the ergodicity issues. In this thesis, we will pursue the idea of an extension of the auxiliary fields to the complex plane [38] to obtain an implementation that is as fast as possible.

### 4.1 Complexification

In this section we discuss the extension from the continuous auxiliary fields to the complex plane to circumvent the ergodicity problem. The extension to complex numbers will double the dimension of the phase space that has to be sampled by molecular dynamics. It retains the potential barriers but, due to the additional degrees of freedom, the integrator should be able to move around them. Like the auxiliary fields, the determinants become complex. At half filling the determinant of the spin up and spin down sector always have the same sign in the real formulation, for complex fields they are complex conjugated to each other as we will see.

The first step to the complexification is a decoupling of the Hubbard interaction by introducing a free parameter  $\alpha \in [0, 1]$

$$\hat{H}'_{\text{U}} = \sum_i \alpha \frac{U}{2} (\hat{n}_{i,\uparrow} + \hat{n}_{i,\downarrow} - 1)^2 - \sum_i (1 - \alpha) \frac{U}{2} (\hat{n}_{i,\uparrow} - \hat{n}_{i,\downarrow})^2. \quad (4.1)$$

It decouples the Hubbard interaction into a charge and a spin sector. Utilizing  $\hat{n}_{i,\sigma}^2 = \hat{n}_{i,\sigma}$  only a constant addend in the decoupled Hubbard interaction term  $\hat{H}'_{\text{U}}$  is different from the original  $\hat{H}_{\text{U}}$ . Of course, the physical results are independent of  $\alpha$ . Its single purpose is to modify the configuration space we have to sample. The new parameter  $\alpha$  interpolates between the purely real and purely imaginary formulation. Using  $\alpha = 0$  leaves everything as discussed in the previous chapter. For  $\alpha = 1$  the Hubbard-Stratonovich field is purely imaginary. This formulation is comparable with the formulations used in Refs. [12, 13, 39, 40, 41, 42]. As supposed by the authors of Ref. [25] and subsequently discussed and shown in Refs. [43, 44], the purely imaginary formulation also suffers from ergodicity problems. Therefore, we go on now with a complex formulation,  $\alpha \in (0, 1)$ , where the number of auxiliary field components is doubled.

We have to redefine a couple of symbols we already introduced in the previous chapter. For distinction we add a prime to the redefined variables. Naturally, the decoupled Hubbard interaction leads to a doubling of the auxiliary fields

$$e^{-\Delta\tau \hat{H}'_{\text{U}}} \propto \int dx_{i,l} dy_{i,l} \exp \left\{ -\Delta\tau \sum_i \left[ x_{i,l}^2 + y_{i,l}^2 + \left( \sqrt{2U(1-\alpha)} x_{i,l} + i\sqrt{2U\alpha} y_{i,l} \right) \left( \hat{n}_{i,\uparrow} - \frac{1}{2} \right) - \left( \sqrt{2U(1-\alpha)} x_{i,l} - i\sqrt{2U\alpha} y_{i,l} \right) \left( \hat{n}_{i,\downarrow} - \frac{1}{2} \right) \right] \right\}, \quad (4.2)$$

and we substitute

$$S'_{\text{B}}(x, y) := \Delta\tau \sum_i (x_i^2 + y_i^2). \quad (4.3)$$

To improve readability, we define a combined notation to interpret the two fields as components of a single complex field

$$z_{i,l} := \sqrt{2U(1-\alpha)} x_{i,l} + i\sqrt{2U\alpha} y_{i,l}. \quad (4.4)$$

To keep the notation light we will switch between both notations, depending on which one fits

best to the considered expressions. Accordingly, the partition function becomes

$$Z = \int [\delta z \delta \bar{z}] e^{-S_B(z, \bar{z})} e^{\Delta\tau \sum_{i,l} \frac{z_{i,l}}{2}} \det M'_\uparrow(z, \bar{z}) e^{-\Delta\tau \sum_{i,l} \frac{\bar{z}_{i,l}}{2}} \det M'_\downarrow(z, \bar{z}), \quad (4.5)$$

while the block structure of the occurring matrices remains unchanged

$$M'_\sigma = \begin{pmatrix} \mathbb{1} & 0 & 0 & \cdots & 0 & B'_{N_\tau, \sigma} \\ -B'_{1, \sigma} & \mathbb{1} & 0 & \cdots & 0 & 0 \\ 0 & -B'_{2, \sigma} & \mathbb{1} & \cdots & 0 & 0 \\ \vdots & \vdots & \vdots & \ddots & \vdots & \vdots \\ 0 & 0 & 0 & \cdots & \mathbb{1} & 0 \\ 0 & 0 & 0 & \cdots & -B'_{N_\tau-1, \sigma} & \mathbb{1} \end{pmatrix}, \quad (4.6)$$

with

$$B'_{l, \sigma}(z, \bar{z}) = e^{-\Delta\tau K} e^{-\sigma \Delta\tau V'_{l, \sigma}(z, \bar{z})}, \quad (4.7)$$

and

$$[V'_{l, \sigma}(z, \bar{z})]_{i, j} = \begin{cases} z_{i, l} \delta_{i, j} & \sigma = \uparrow \\ \bar{z}_{i, l} \delta_{i, j} & \sigma = \downarrow \end{cases}. \quad (4.8)$$

We can use the particle-hole symmetry at half filling to obtain an additional relation between the spin up and spin down matrix

$$e^{-\Delta\tau \sum_{i, l} \frac{\bar{z}_{i, l}}{2}} \det M'_\downarrow = e^{\overline{\Delta\tau \sum_{i, l} \frac{z_{i, l}}{2}}} \det M'_\uparrow = e^{\Delta\tau \sum_{i, l} \frac{\bar{z}_{i, l}}{2}} \det M'^\dagger_\uparrow. \quad (4.9)$$

In particular, this means all configurations possess a positive real statistical weight and the complexification does not lead to a sign problem. Furthermore, this relation can be used to simplify the partition function, by a substitution of the spin down sector through the spin up sector

$$\begin{aligned} Z &= \int [\delta z \delta \bar{z}] e^{-S'_B(z, \bar{z})} e^{\Delta\tau \sum_{i, l} \frac{z_{i, l} + \bar{z}_{i, l}}{2}} \det M'_\uparrow(z, \bar{z}) \det M'^\dagger_\uparrow(z, \bar{z}) \\ &= \int [\delta x \delta y] e^{-S'_B(x, y)} \det \left[ e^{\Delta\tau \frac{\sqrt{2U(1-\alpha)}}{N_\tau V_S} \sum_{i, l} x_{i, l}} M'_\uparrow(x, y) M'^\dagger_\uparrow(x, y) \right] \\ &= \int [\delta x \delta y] e^{-S'_B(x, y)} \det \left[ \mathcal{M}_\uparrow(x, y) \mathcal{M}_\uparrow^\dagger(x, y) \right]. \end{aligned} \quad (4.10)$$

Here we have defined

$$\mathcal{M}_\uparrow(x, y) := \kappa(x) M'_\uparrow(x, y), \quad (4.11)$$

and

$$\kappa(x) := \exp \left\{ \Delta\tau \frac{\sqrt{2U(1-\alpha)}}{2N_\tau V_S} \sum_{i,l} x_{i,l} \right\}. \quad (4.12)$$

Once again, we eliminate the determinants by introducing a complex pseudo fermion field  $\phi'_\uparrow$  and obtain

$$Z = \int [\delta x \delta y \delta \phi'_\uparrow \delta \phi'^{\dagger}_\uparrow] e^{-S'_B - \phi'^{\dagger}_\uparrow (\mathcal{M}'_\uparrow \mathcal{M}_\uparrow)^{-1} \phi'_\uparrow}. \quad (4.13)$$

The structure of the partition function is now comparable with the version of Eq. (3.15) in the previous chapter before adding the momentum fields.

Subsequently the system of linear equations we have to solve is also complex. In fact, the number of degrees of freedom is twice as large as before, but because the updates require only one spin sector, a single run of a complex version of the CG method is sufficient.

The sampling of the other auxiliary variables works analogously to the previous sampling. Again we make use of

$$R'_\uparrow := \left( \mathcal{M}'_\uparrow(x, y) \right)^{-1} \phi'_\uparrow \Rightarrow Z \propto e^{-R'^{\dagger}_\uparrow R'_\uparrow}, \quad (4.14)$$

to sample Gaussian random numbers for the real and imaginary part of  $R'_\uparrow$  and multiply them with the matrix  $\mathcal{M}'_\uparrow(x, y)$  to obtain the complex pseudo fermion fields

$$\phi'_\uparrow = \mathcal{M}'_\uparrow(x, y) R'_\uparrow. \quad (4.15)$$

Since the components of the auxiliary fields are doubled, we also have to introduce twice as many momentum fields to define the new artificial Hamilton function

$$\mathcal{H}'(x, y, p_x, p_y, \phi'_\uparrow, \phi'^{\dagger}_\uparrow) := S'_B(x, y) + \sum_{i,l} \left( (p_x)_{i,l}^2 + (p_y)_{i,l}^2 \right) + \phi'^{\dagger}_\uparrow \left( \mathcal{M}'_\uparrow(x, y) \mathcal{M}_\uparrow(x, y) \right)^{-1} \phi'_\uparrow. \quad (4.16)$$

Again, all momentum fields are distributed Gaussian and therefore easy to sample. The required complex version of the Leapfrog is guided by the new version of Hamilton's equations of motion

$$\begin{aligned} \dot{x}_{i,l} &= \frac{\partial \mathcal{H}'(x, y)}{\partial (p_x)_{i,l}} = 2(p_x)_{i,l}, & (\dot{p}_x)_{i,l} &= -\frac{\partial \mathcal{H}'(x, y)}{\partial x_{i,l}}, \\ \dot{y}_{i,l} &= \frac{\partial \mathcal{H}'(x, y)}{\partial (p_y)_{i,l}} = 2(p_y)_{i,l}, & (\dot{p}_y)_{i,l} &= -\frac{\partial \mathcal{H}'(x, y)}{\partial y_{i,l}}. \end{aligned} \quad (4.17)$$

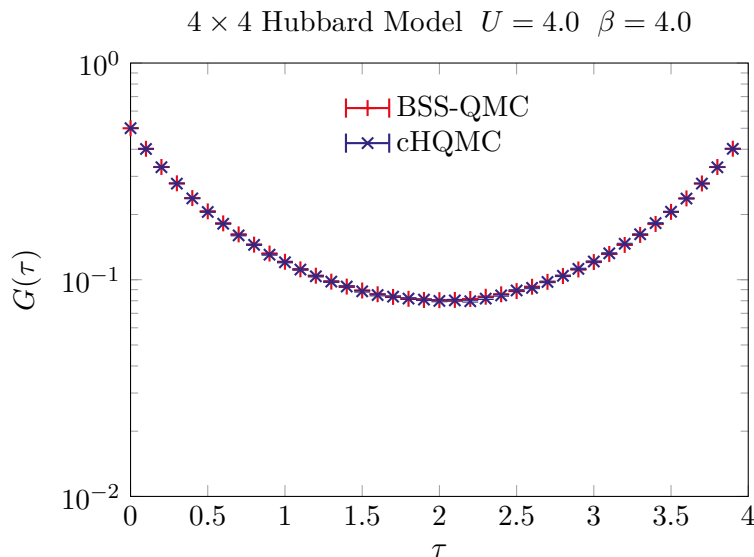


**Figure 4.1:** The local single particle Green’s function, calculated by the complexified HQMC (cHQMC) algorithm ( $\alpha = 0.5$ ) compared to the results of a BSS-QMC simulation [14] for the same set of parameters as in Fig. 3.2.

It is easy to see that the differential equations decouple into the two parts of the auxiliary field.

For measurements of the single particle Green’s function we use the same stochastic inversion as in the previous chapter. The inverse matrix ( $M'_\sigma{}^{-1}$ ) can be sampled by the unbiased estimator

$$[(M'_\sigma{}^\dagger M'_\sigma)^{-1} \phi_\sigma]_i [R'_\sigma]_j = [X'_\sigma]_i [R'_\sigma]_j. \quad (4.18)$$

In detail, the doubling of the degrees of freedom compensated the additional factor of 2 that was present in the previous formulation due to the variance of the used Gaussian distributions. Because we are sampling the inverse of a complex matrix, also the estimator is complex. All unphysical imaginary parts cancel during the Monte Carlo sampling schemes.

## 4.2 Results of the complex HQMC

Repeating the benchmark test of Fig. 3.2 with the complex hybrid quantum Monte Carlo formulation (cHQMC) shows a good agreement with the reference results. Fig. 4.1 shows the results for the same set of parameters as before. The single particle Green’s function is the easiest accessible observable for HQMC methods. To ensure the cHQMC method gives correct results, we also

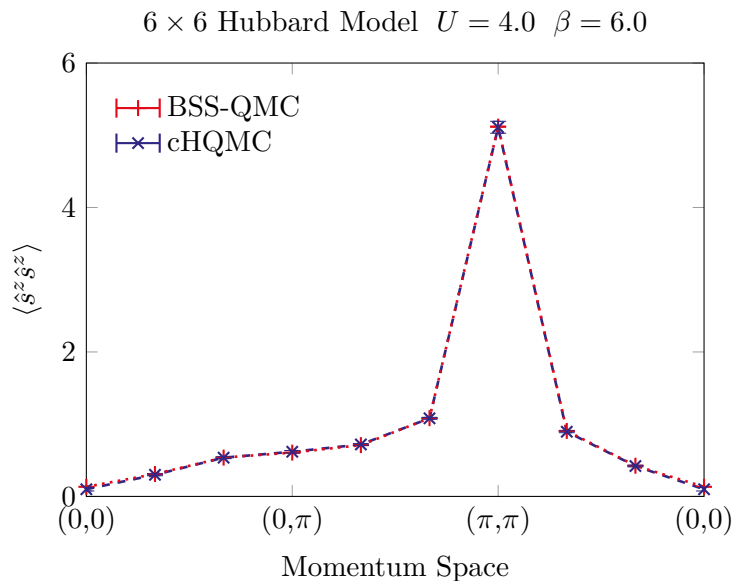


**Figure 4.2:** Results of the cHQMC ( $\alpha = 0.5$ ) for equal-time spin-spin-correlation functions in momentum space and the benchmark results of the BSS-QMC method [14].

compared higher observables like equal-time spin-spin-correlation functions

$$\langle \hat{s}_i^z(\tau) \hat{s}_j^z(\tau) \rangle = \frac{1}{4} \left\langle \left( \hat{n}_{\uparrow,i}(\tau) - \hat{n}_{\downarrow,i}(\tau) \right) \left( \hat{n}_{\uparrow,j}(\tau) - \hat{n}_{\downarrow,j}(\tau) \right) \right\rangle. \quad (4.19)$$

Therefore, Wick's theorem is important for the method. It allows us to decompose many particle Green's functions into expressions that only require single particle Green's functions. Fig. 4.2 shows the excellent agreement between cHQMC and BSS-QMC results for equal-time spin-spin-correlation functions in the momentum space. Obviously, the single particle Green's function plays an important role for all measurements. Because it is computed by stochastic inversion, additional noise enters the measuring procedures and has to be compensated by generating enough samples.

To analyze the runtime and benchmark the scaling of the algorithm we performed simulations in one, two and three dimensions at different inverse temperatures  $\beta$ . The initial hope was to achieve a favorable scaling with system size and inverse temperature, in an ideal situation close to a linear scaling. However, in contrary to our aspirations, the achieved scaling did not fulfill our desires. In particular, there are two main reasons that are responsible for the scaling behavior. The first one is the observation that the number of CG iterations that are needed to solve the occurring systems of linear equations grows nearly linearly with the Euclidean system size (see Fig. 4.3). The other reason has its origin in the acceptance rate. Due to the Metropolis check,



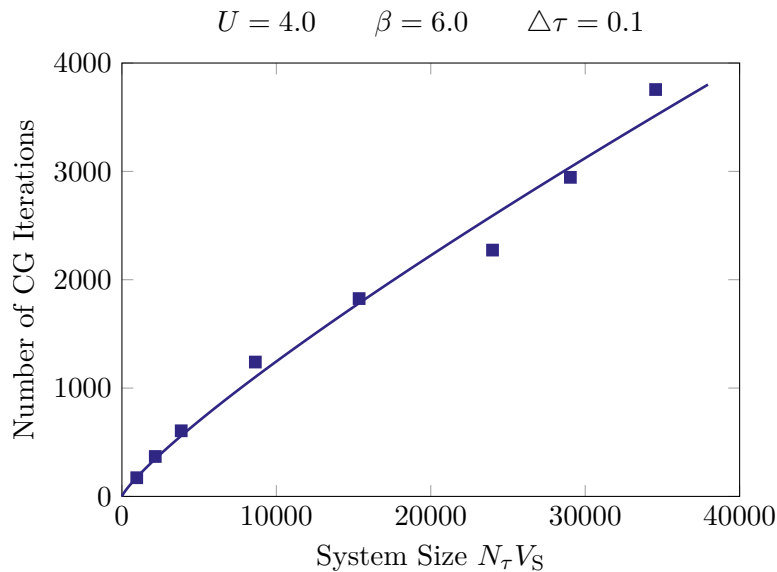


**Figure 4.3:** Average number of CG iterations that are needed to solve a system of linear equations, as a function of the Euclidean system size that is given by the product of Trotter slices and the lattice volume ( $N_\tau V_S$ ).

the Leapfrog update has to propose auxiliary field configurations with the same energy as the initial configuration. Because the energy difference is an extrinsic quantity for our method, the Leapfrog time steps have to be shortened for larger lattice sizes and inverse temperatures. To keep the acceptance high, we have to rescale the artificial time step of the Leapfrog method as  $\Delta t \propto V_S^{-1} \beta^{-1}$ . Combined with the numerical effort of linearly scaling vector operations we achieved a scaling of approximately

$$\left(L^d \beta\right)^{2.5-3.0}. \quad (4.20)$$

As it is common to visualize how the scaling depends on the lattice dimension  $d$  we write  $L^d$  instead of  $V_S$  as volume of the lattice.

### 4.3 Comparison with the BSS-QMC method for the Hubbard model

Now all important ideas of the complex HQMC method are discussed, but a detailed comparison with competing algorithms like the BSS-QMC remains. In this subsection we compare our implementation of the complex HQMC method with the ALF implementation [14] of the BSS-QMC method. We compare the computational effort they need to simulate the half-filled Hubbard model. The ALF package is an optimized and well established software package. What makes

the BSS-QMC method predetermined for a comparison is the systematical error that comes from exactly the same Trotter decomposition as for the HQMC method.

At this point we have to discuss the similarities and distinctive features of the methods. For a detailed introduction to the BSS-QMC method we refer to the literature like Ref. [28, 14]. As mentioned, BSS-QMC and HQMC are very similar. The basic idea is to use an auxiliary field to sample the partition function after a Trotter decomposition. In contrast to the HQMC method, the BSS-QMC uses a discretized Hubbard-Stratonovich field with only two possible values per component. Instead of using pseudo fermions the BSS-QMC method keeps the determinant in the partition function given by the representation of Eq. (3.12). So-called single spin flip updates are the update scheme of the method. The Markov chain is constructed through flipping single auxiliary field components in combination with a Metropolis check. For measurements it also uses Wick's theorem to reduce many-body operators in terms of the single particle Green's function. In contrast to the HQMC the BSS-QMC uses a direct inversion scheme to perform the measurements. Due to the instability of the matrix product over the block matrices  $B_{l,\sigma}$ , a numerical stabilization is necessary. Most of the numerical effort is spent in matrix operations as the stabilization or the calculation of the determinants. Because all steps of the method are static the scaling behavior of the numerical effort of the BSS-QMC method can be determined to  $(L^d)^3\beta$ . The cubic scaling dependency on the lattice volume together with long autocorrelation times, like for electron-phonon models [16], due to the local update scheme are often seen as the bottleneck of the method. The occurrence of the sign problem is identical for both methods and strongly model dependent. The HQMC method has a lot of free parameters, like the number, the step size and the length of Leapfrog updates between measurements or the number of stochastic inversions per measurement. In contrast BSS-QMC methods require much less fine-tuning. To speed up the implementation it is important for the BSS-QMC as well as for the HQMC how to deal with exponentiated matrices like the Hopping matrix that are contained in the block matrices  $B_{l,\sigma}$ . Appendix A addresses how to optimize this part of the methods.

To maximize comparability the both methods are tested on the same hardware with the same computing resources. The data analysis is performed afterwards by the same routines for the data of both methods. A minimal overview of the two most important data analysis tools for quantum Monte Carlo methods can be found in Appendix B.

Properties like required memory or effective scaling are also important for every numerical algorithm. For Monte Carlo methods the fluctuations due to the statistical approach are unfortunate but inherent. According to the central limit theorem, error bars decrease with the square root of the number of measured samples, or equivalently with the square root of the computing time.

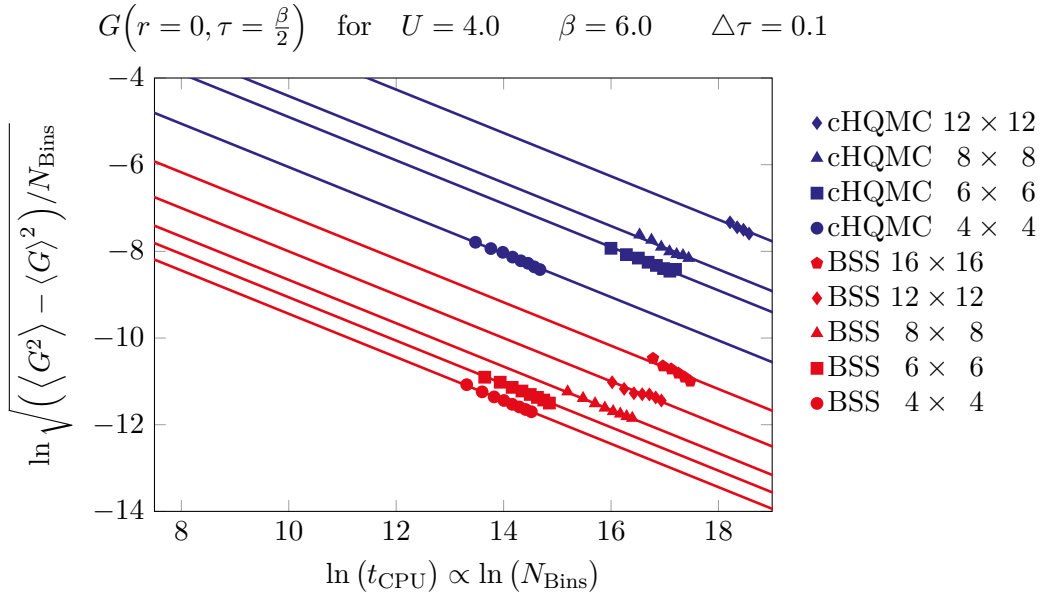


**Figure 4.4:** Comparison of error bars of BSS-QMC and cHQMC as function of computing time for several system sizes.

The remaining prefactor of this behavior corresponds to the fluctuations of the method. Figure 4.4 shows the decay of stochastic errors for simulations of the Hubbard model for several system sizes. The BSS-QMC as well as the cHQMC show the expected behavior as function of the computational time. But Fig. 4.4 also illustrates the precision of the BSS-QMC method. For a given computational time it achieves much smaller error bars compared to the cHQMC method. It is known that in a half-filled Hubbard model the spin correlation length diverges exponentially with inverse temperature. This scaling is valid in a temperature regime that corresponds to the so-called renormalized classical regime [45]. The used parameters,  $U = 4$  and  $\beta = 6$ , place the simulations in this regime [46]. This region is considered as *hard* for Monte Carlo simulations.

Summarizing, the complex Hybrid quantum Monte Carlo method is able to simulate the half-filled Hubbard model. We discussed the scaling of its numerical effort and compared it in an ambitious scenario with the well established BSS-QMC method. Even if the cHQMC was not able to compete with the precision of the ALF implementation the benchmark plots visualize the agreement between the methods. In the next chapter we will apply the HQMC method to an electron-phonon model that can not be simulated by the BSS-QMC and which can maybe profit from the global-update scheme of HQMC.



# 5

## Chapter 5

---

# Hybrid Quantum Monte Carlo method on the SSH model

So far we only discussed the usage of the HQMC method for simulations of the Hubbard model. As we found out in the previous chapter the HQMC method is not able to compete with the BSS-QMC method on this model. In the next step we now face another type of model which is known to be hard for the BSS-QMC method. In Ref. [16] the authors present measurements of autocorrelation times if the BSS-QMC method is used to simulate electron-phonon models. Especially in two and higher dimensions the autocorrelation effects prevent any simulation. The physical description of phonons on a lattice is similar to the field of lattice gauge theory in high-energy physics where HQMC methods are widely used. The global updates of the method seems to be the perfect choice to overcome the autocorrelation problems of the BSS-QMC method.

In this chapter we present how the two-dimensional Su-Schrieffer-Heeger (SSH) model [47] can be simulated in the HQMC framework. We concentrate on the numerical and conceptual aspects of the HQMC implementation, as also presented in Ref. [25]. A detailed discussion about the history and physics of the SSH model is provided in the next chapter of this thesis.

## 5.1 HQMC formulation for the SSH model

This section is aimed at describing a HQMC formulation for the SSH model on a square lattice. With respect to universality, we discuss the implementation for an arbitrary number of spin flavors

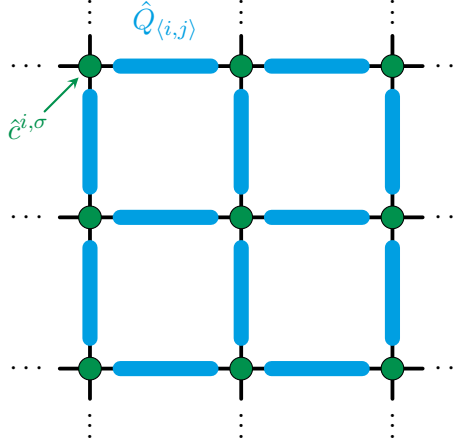


**Figure 5.1:** Sketch of the SSH lattice.

$N_{\text{col}}$ . Starting with the general form of an electron-phonon Hamiltonian  $\hat{H}$  we distinguish a pure electronic  $\hat{H}_{\text{el}}$ , a pure phononic  $\hat{H}_{\text{ph}}$  and a coupling term  $\hat{H}_{\text{ep}}$ , hence

$$\hat{H} = \hat{H}_{\text{el}} + \hat{H}_{\text{ph}} + \hat{H}_{\text{ep}}. \quad (5.1)$$

Like for the Hubbard model, the free electronic energy is represented by a tight-binding Hamiltonian on the square lattice

$$\hat{H}_{\text{el}} = -t \sum_{\langle i,j \rangle, \sigma} \left( \hat{c}_{i,\sigma}^\dagger \hat{c}_{j,\sigma} + \hat{c}_{j,\sigma}^\dagger \hat{c}_{i,\sigma} \right), \quad (5.2)$$

where  $\langle i, j \rangle$  denotes nearest neighbors. Lattice vibrations are modeled by harmonic oscillators on the links between neighboring lattice sites, see Fig. 5.1. The according term in the Hamiltonian

$$\hat{H}_{\text{ph}} = \sum_{\langle i,j \rangle} \left[ \frac{1}{2m} \hat{P}_{\langle i,j \rangle}^2 + \frac{k}{2} \hat{Q}_{\langle i,j \rangle}^2 \right], \quad (5.3)$$

contains the position operator  $\hat{Q}_{\langle i,j \rangle}$  and the momentum operator  $\hat{P}_{\langle i,j \rangle}$ , as well as the mass constant  $m$  and the force constant  $k$ . The lattice vibrations modulate the electronic hopping, as represented by the interaction part of the Hamiltonian

$$\hat{H}_{\text{ep}} = g \sum_{\langle i,j \rangle, \sigma} \hat{Q}_{\langle i,j \rangle} \left( \hat{c}_{i,\sigma}^\dagger \hat{c}_{j,\sigma} + \hat{c}_{j,\sigma}^\dagger \hat{c}_{i,\sigma} \right). \quad (5.4)$$

Here  $g$  denotes the strength of the coupling between electrons and phononic vibrations. To keep the notation simple, we introduce the bond labeling

$$b := \langle i, j \rangle. \quad (5.5)$$

In order to formulate the path integral description of the partition function, we choose a real space basis in which  $\hat{Q}_b$  is diagonal

$$\hat{Q}_b |x_b\rangle = x_b |x_b\rangle, \quad (5.6)$$

which can be used to write the partition function

$$Z = \text{Tr} \int \prod_b dx_b \langle x_b | e^{-\beta \hat{H}} | x_b \rangle. \quad (5.7)$$

Using the standard real space path integral, followed by integrating out the fermions brings us to

$$Z = \int \prod_{b,l} dx_{b,l} e^{-S_0(x)} \left[ \det M(x) \right]^{N_{\text{col}}}, \quad (5.8)$$

which is equivalent to the the representation we used for the Hubbard model in Eq. (3.6). The bosonic variables  $x_{b,l}$  play the role of the auxiliary field in the Hubbard model. In contrast to the artificial Hubbard-Stratonovich fields, the phononic variables  $x_{b,l}$  possess intrinsic imaginary-time dynamics resulting from the momentum operators of the harmonic oscillators and is put in the action term

$$S_0(x) := \Delta\tau \sum_{b,l} \left( \frac{m}{2} \left[ \frac{x_{b,l+1} - x_{b,l}}{\Delta\tau} \right]^2 + \frac{k}{2} x_{b,l}^2 \right). \quad (5.9)$$

Because the phonons do not care about the spins of the electrons, the partition function factorizes and each power of the determinant corresponds to one of the initial spin sectors. Therefore we introduce the notation for the hopping operator of a single spin sector as

$$\hat{K}_b := \hat{c}_i^\dagger \hat{c}_j + \hat{c}_j^\dagger \hat{c}_i. \quad (5.10)$$

The matrix  $M(x)$  has still the same block structure as initially shown in Eq. (3.8). Here, the block matrices  $B_l$  contain the exponentiated matrix representation of the phonon-modulated electron hopping

$$B_l = \exp \left\{ -\Delta\tau \sum_b (g x_{b,l} - t) K_b \right\}. \quad (5.11)$$

In Appendix A we regard several methods how to handle  $B_l$  in order to minimize the numerical effort.

The absence of the sign problem is obvious for any even number of spin flavors, see Eq. (5.8). This also holds for odd numbers of spin flavors, assuming a bipartite lattice. For this we have to demonstrate  $\det M(x) > \varepsilon$  for a finite positive constant  $\varepsilon$ . Unfortunately we can only show the weaker statement  $\det M(x) \geq 0$ . This means singularities in the configuration space are still possible but, in contrast to the real continuous field formulation of the Hubbard model, there is no reason for them to form domain walls or any kind of connected structures in the extremely high dimensional configuration space. To prove the statement we consider a single spin degree of freedom and introduce a Majorana basis on the sublattices  $A$  and  $B$  of the bipartite lattice

$$\begin{aligned} i \in A: \quad \hat{\gamma}_{i,1} &= (\hat{c}_i + \hat{c}_i^\dagger) & \hat{\gamma}_{i,2} &= -i(\hat{c}_i - \hat{c}_i^\dagger) \\ i \in B: \quad \hat{\gamma}_{i,1} &= -i(\hat{c}_i - \hat{c}_i^\dagger) & \hat{\gamma}_{i,2} &= -(\hat{c}_i + \hat{c}_i^\dagger). \end{aligned} \quad (5.12)$$

Rewriting the hopping part in terms of Majorana results in

$$\sum_b (-t + g x_{b,l}) \hat{K}_b = \frac{i}{2} \sum_{\substack{\langle i,j \rangle \\ n=1,2}} (-t + g x_{\langle i,j \rangle, l}) \hat{\gamma}_{i,n} \hat{\gamma}_{j,n}. \quad (5.13)$$

Pulling the sublattice summation out of the trace leads to a factorizing formulation of the fermionic part of the partition function

$$\mathrm{Tr} \prod_{l=1}^{N_\tau} e^{-\Delta\tau \sum_b (-t + g x_{b,l}) \hat{K}_b} = \left[ \mathrm{Tr} \prod_{l=1}^{N_\tau} e^{-i \frac{\Delta\tau}{4} \sum_{\langle i,j \rangle} (-t + g x_{\langle i,j \rangle, l}) \hat{\gamma}_i \hat{\gamma}_j} \right]^2. \quad (5.14)$$

While the trace over a Majorana mode has to be a real number [48] its square, which is equal to the determinant we are looking for, has to be positive or zero. Thereby, it holds

$$\det M(x) \geq 0. \quad (5.15)$$

Because this is true for every spin sector, no negative statistical weights can be generated.

The next step to formulate an HQMC implementation of the SSH model is to redefine

$$\tilde{x}_{b,l} := \sqrt{\frac{k}{2}} x_{b,l}, \quad \omega_0^2 := \frac{k}{m}, \quad \tilde{g} := \sqrt{\frac{2}{k}} g. \quad (5.16)$$



Once again we introduce pseudo fermions  $\phi_\sigma$  for each spin flavor and conjugated momenta  $p$

$$Z = \int \left[ \delta x \delta p \prod_{\sigma=1}^{N_{\text{col}}} \delta \phi_\sigma \right] \exp \left\{ - \Delta\tau \underbrace{\left[ \sum_b \left( \omega_0^{-2} \left[ \frac{\tilde{x}_{b,l+1} - \tilde{x}_{b,l}}{\Delta\tau} \right]^2 + \tilde{x}_{b,l}^2 \right) \right]}_{=S_0(\tilde{x})} - \sum_{\sigma=1}^{N_{\text{col}}} \phi_\sigma^\top \left( M^\top(x) M(x) \right)^{-1} \phi_\sigma - \sum_b p_{b,l}^2 \right\} \quad (5.17)$$

From now on, everything is alike the implementation of the Hubbard model. We choose initial configurations of the phononic fields, generate random numbers to sample the momentum and pseudo fermion fields. Followed by performing a Leapfrog integration of Hamilton's equation of motion to update the auxiliary field. A Metropolis check accepts or rejects the updated bosonic field configurations before performing the measurements of observables. Afterwards the method goes on by sampling new random numbers.

Again, the CG method is used to solve the systems of linear equations. In contrast to the Hubbard model, a preconditioner is not necessary for the SSH model. The uncompleted Cholesky decomposition we used for the Hubbard model is also not applicable because the  $B$  block matrices in Eq. (5.11) only consist of the hopping part. Previously we neglected this part and concentrated on the interaction terms to construct a preconditioner. The lack of an onsite electron-electron interaction term prevents us from using the same uncompleted Cholesky decomposition as preconditioner. Fortunately, the condition numbers are much better and even a not preconditioned CG solver works quite fast and stable for the SSH model.

Henceforth we will return to spins with two degrees of freedom.

## 5.2 Proof of concept

Because no reliable benchmark results for the SSH model in two dimensions are available so far, we decided to compare with results of the continuous time integration method [49] (CT-INT)<sup>1</sup>. In general, the CT-INT method suffers from a sign problem for simulations of the two-dimensional SSH model. To compare data we had to choose a regime where the sign problem can be controlled. In Fig. 5.2 we compare results for the local Green's function while Fig. 5.3 shows the data for

<sup>1</sup>We gratefully acknowledge Martin Hohenadler for generating the benchmark data and making them available.

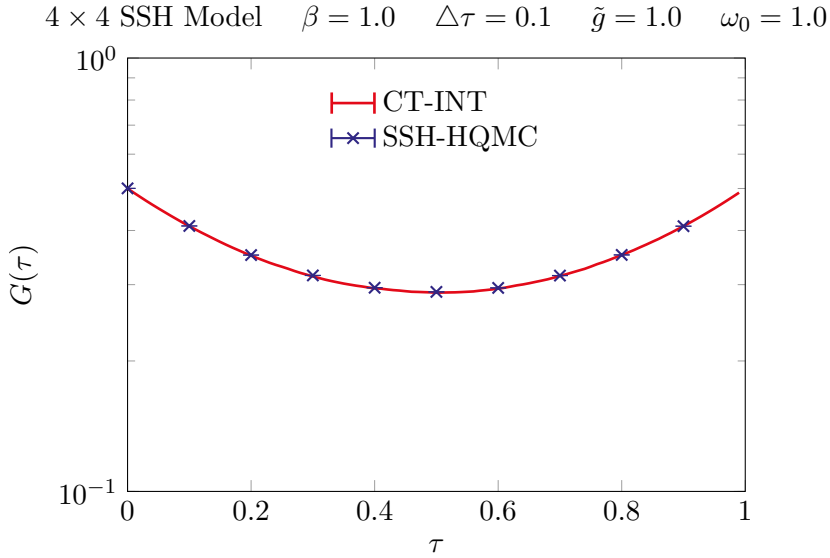


**Figure 5.2:** CT-INT and HQMC results for the local Green’s function of the SSH model. (error bars smaller than line width)

spin-spin correlation functions. Both plots visualize the perfect agreement between the different methods.

As we learned in the previous chapters, apart from the correctness of physical results the scaling of a method is one of the key points to decide if it is practicable or not. Comparing the models, the HQMC method seems to scale much better for the phononic SSH model. Primarily, the dependency of the acceptance rate on the Leapfrog step size is much weaker than for the Hubbard model. For simulations of the SSH model it was sufficient to choose  $\Delta t \propto V_S^{-0.25} \beta^{-0.25}$  in most cases. Note that for the Hubbard model, we had to use  $\Delta t \propto V_S^{-1} \beta^{-1}$ . We assume this as a result of a well behaved effective action, where singularities are no issue. Fig. 5.4 and Fig. 5.5 show how the number of CG iterations, which are necessary to achieve the desired accuracy, depends on the system size ( $V_S \times N_\tau$ ). While the number of iterations flattens for larger lattice volumes (Fig. 5.4) it grows approximately linear if  $\beta$  is increased (Fig. 5.5). This causes an asymmetry between temporal and spatial scaling of the method.

Combining CG and Leapfrog scaling the numerical effort of the HQMC method for the SSH model can be estimated to

$$(L^d)^{1.25-1.5} \beta^{2.25-2.5}. \quad (5.18)$$

Finally, the achieved scaling is sufficient to perform first reliable simulations of the SSH model in higher dimensions.

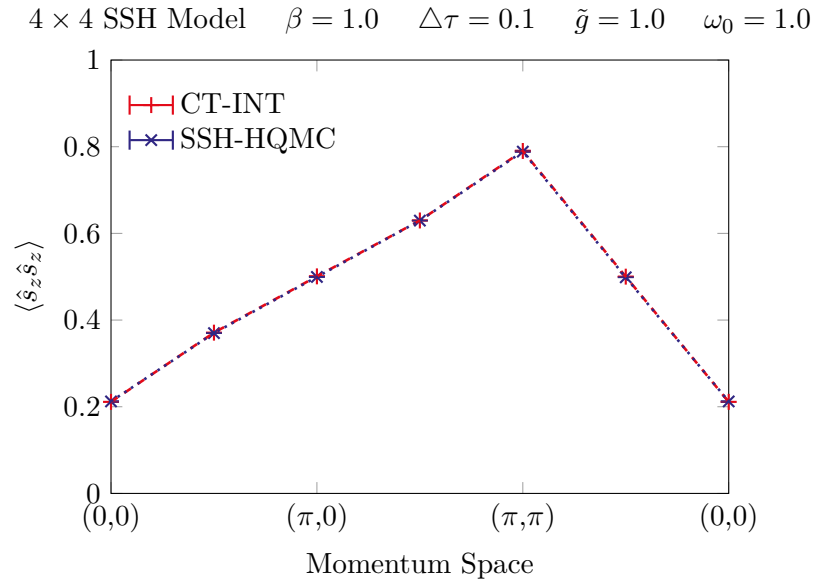


**Figure 5.3:** CT-INT and HQMC results of spin-spin correlation functions in the momentum space for the SSH model. (error bars smaller than line width)

Summarizing, the HQMC results passed all benchmark tests and provides a competitive scaling behavior. It seems like the HQMC method is well on its way to extend the success of quantum Monte Carlo methods to phononic models in higher dimensions.

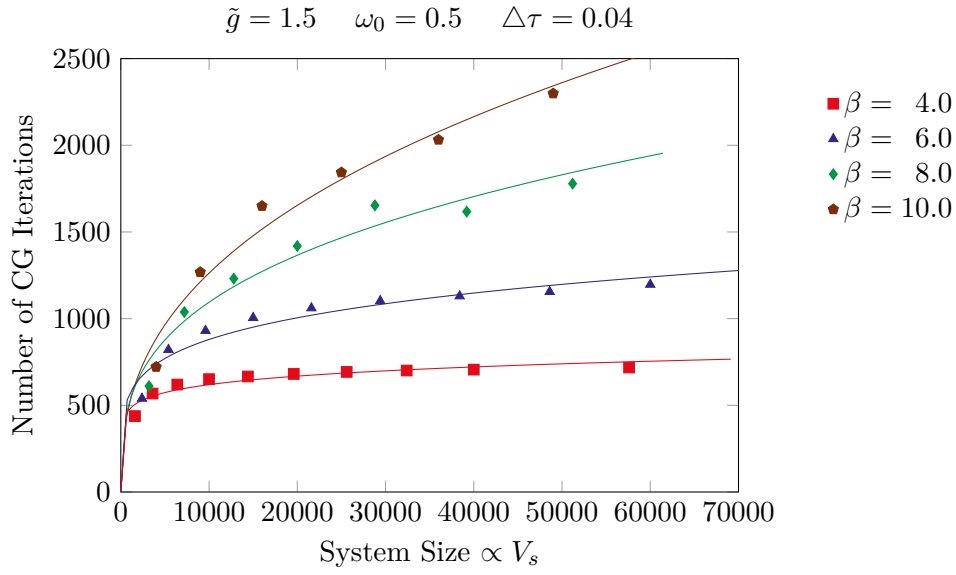


**Figure 5.4:** Number of CG iterations required for a given accuracy at various temperatures as functions of the lattice volume  $V_s$ . For this plot we considered  $4 \times 4$ ,  $6 \times 6$ ,  $8 \times 8$ ,  $10 \times 10$ ,  $12 \times 12$ ,  $14 \times 14$ ,  $16 \times 16$ ,  $18 \times 18$ ,  $20 \times 20$  and  $24 \times 24$  lattices.

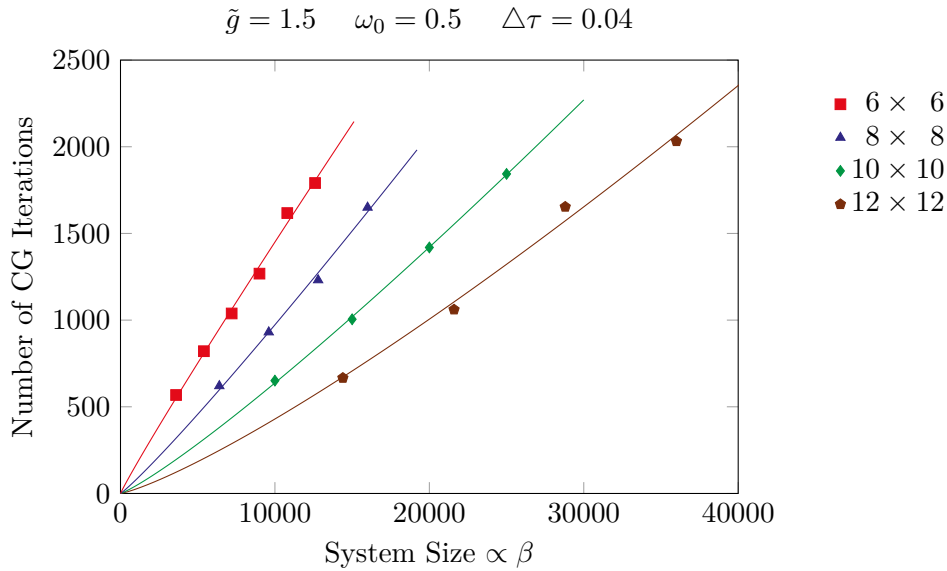


**Figure 5.5:** Number of CG iterations for different lattice sizes as function of the inverse temperature,  $\beta = \Delta\tau N_\tau$ . For this plot we considered  $\beta = 6.0$ ,  $8.0$ ,  $10.0$  and  $12.0$ .

## **Part II**

# **The Physics of the two-dimensional SSH Model**



# 6

## Chapter 6

# The two-dimensional SSH model

In this chapter we discuss the physics of the two-dimensional Su-Shrieffer-Heeger model. At the beginning, we take a short look at the origins of the model and some important properties in the one-dimensional case. In the following section we go on with a discussion of the symmetries of the SSH model and which phases are expected to show up in two dimensions. Afterwards we use a mean field approach to investigate the valence bond ground state. At the end of this chapter we present HQMC simulation results and discuss the frequency-dependent phase transition. Currently a publication of the results of this chapter is in preparation.

## 6.1 Motivation and Origins

Initially, the SSH model was proposed to describe solitons in conducting polymers [47]. In order to model the influence of vibrations inside the molecules on the behavior of electrons, the authors of Ref. [47] use harmonic oscillators, related to the bonds between the atoms in the molecules, and couple them to the quantized hopping of the electrons. As given in Eq. (5.1), the SSH Hamiltonian reads

$$\hat{H} = \sum_{\langle i,j \rangle, \sigma} (g \hat{Q}_{\langle i,j \rangle} - t) (\hat{c}_{i,\sigma}^\dagger \hat{c}_{j,\sigma} + \hat{c}_{j,\sigma}^\dagger \hat{c}_{i,\sigma}) + \sum_{\langle i,j \rangle} \left[ \frac{1}{2m} \hat{P}_{\langle i,j \rangle}^2 + \frac{k}{2} \hat{Q}_{\langle i,j \rangle}^2 \right].$$

Fig. 6.1 shows a popular one-dimensional application example of the SSH model, mentioned in Refs. [47, 50]. Without doping, a single conducting electron belongs to each carbon atom in polyacetylene molecules. Each of them forms together with one of the neighboring conduction electrons an additional chemical binding between their atoms. In this way, an alternating pattern of double bindings between the carbon atoms is established. Modeling processes like this was a

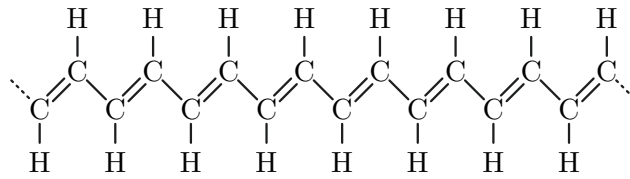


**Figure 6.1:** Structural formula of polyacetylene.

purpose of Su, Schrieffer and Heeger when they discussed the model in Refs. [47, 50]. Besides the bond ordering phase the one-dimensional SSH model also exhibits a charge density wave state as well as a Luttinger liquid in its phase diagram [51].

Furthermore, the one-dimensional SSH model is a textbook example of topology in condensed matter [52]. Abstracting the bond pattern of Fig. 6.1 to an effective tight-binding model yields a bipartite chain as shown in Fig. 6.2a. The dashed gray line marks the unit cell of the one-dimensional lattice. Sites are colored accordingly to the sublattice they belong to. Double bindings cause an increased tight-binding hopping parameter  $v$ . Therefore it holds  $v > w$ , where  $w$  belongs to bonds with a single chemical binding. Of course, the formation of this pattern breaks the previous translation symmetry spontaneously and could also choose  $w > v$ . In general, the lowering of the energy of a one-dimensional half-filled system by periodic lattice distortions is called Peierls-instability [53]. In the next step we consider the limiting cases where the weaker hopping process can be neglected. Therefore, two states are possible. Either the hopping remains only within the same unit cells, see Fig. 6.2b, or between different unit cells, Fig. 6.2c. In the first case, all electrons are paired and the system forms an insulator. In the second case, the electrons at the edges stay unpaired in contrast to all electrons in the bulk. The free electron states at the edge of the chain are called edge states. Therefore, this case is a minimal example for a topological insulator, having an insulating bulk but conducting states at the edges. For a more detailed discussion about topology, phase boundaries in one dimension and related topics we refer to the literature like Refs. [52, 53].

Besides its importance for topology, three decades after its introduction the one-dimensional SSH model is still the subject of scientific investigations [51, 54]. Nevertheless, not much is known about the pure SSH model in higher dimensions. Mean field investigations like in Refs. [55, 56, 57, 58] discuss some properties and the interplay with other quantum mechanical models like Hubbard interaction and discuss bond states as in the one-dimensional case. In addition, Ref. [59] uses a Monte Carlo method to investigate some spectroscopic properties of the SSH model in monolayer graphene. However, reliable results for the phase diagram of the SSH model in higher dimensions are still not available.



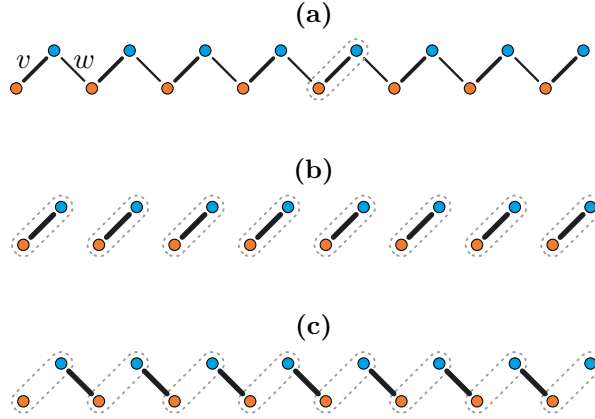


**Figure 6.2:** Bipartite one-dimensional chain of the SSH model with different types of dimerization.

## 6.2 Symmetries and Expectations

Initially, we discuss the fundamental symmetries of the SSH model on the square lattice to deduce physical expectations. Because we are considering a square lattice the according discrete  $C_4$  symmetry is transferred to the considered model. We already mentioned some further symmetries in Chapter 5 due to their importance for the implementation of the HQMC method. On the bipartite square lattice the SSH model is symmetric with respect to a particle-hole transformation. Moreover, we can also rewrite the model in terms of the Majorana basis in Eq. (5.11). As mentioned in Ref. [60], the Majorana representation is equivalent to an  $O(4) = SU(2) \times SU(2)$  symmetry that connects the  $SU(2)$  spin rotation symmetry of the electrons with the  $SU(2)$  rotation symmetry of the Anderson pseudospin  $\hat{\eta}$  [61]. Analogous to the usual spin vector of electrons, the Anderson pseudospin vector can be characterized by ladder operators

$$\hat{\eta}_i^+ = \hat{c}_{i,\uparrow}^\dagger \hat{c}_{i,\downarrow}^\dagger, \quad \hat{\eta}_i^- = \hat{c}_{i,\uparrow} \hat{c}_{i,\downarrow} \quad \text{and} \quad \hat{\eta}_i^z = \hat{n}_{i,\uparrow} + \hat{n}_{i,\downarrow} - 1. \quad (6.1)$$

In detail, for a given  $O(4)$  symmetry an antiferromagnetic (AFM) phase is equivalent to a charge density wave (CDW) including a superconducting (SC) phase. Note, due to the Anderson pseudo spin representation the CDW is always connected to the SC phase. However, considering the  $O(4)$  symmetric case we use the notation of a AFM/CDW/SC phase. As discussed in Ref. [60], the  $O(4)$  symmetry can also be understood by a  $SO(4) = \frac{SU(2) \times SU(2)}{\mathbb{Z}_2}$  symmetry that has to be combined with the  $\mathbb{Z}_2$  occupation parity, which is equivalent to the particle-hole symmetry, to recover the  $O(4)$  symmetry of the SSH model with two spin flavors on a bipartite lattice, as associated with the

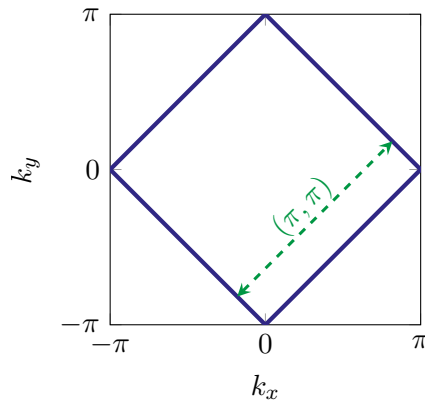


**Figure 6.3:** The Fermi surface of the half-filled two-dimensional tight-binding model in the first Brillouin zone with  $(\pi, \pi)$  nesting.

Majorana representation. The occupation parity acts like an Ising variable. In the thermodynamic limit it can break the symmetry between AFM and CDW/SC spontaneously.

Besides temperature and lattice size, the model itself has two independent parameters. On one side we have the coupling strength  $g$  between electrons and phonons. On the other side the energy of a phonon excitation  $\omega_0$  plays an important role in the SSH model.

In case of zero coupling  $g = 0$  the pure tight-binding model has a quadratic Fermi surface in the first Brillouin zone, see Fig. 6.3. At half filling it has two special features. Due to the Van Hove singularities the density of states is diverging and the entire Fermi surface is nested with respect to a momentum vector of  $(\pi, \pi)$ . Proceeding from this, we may suppose that also the ground state will be  $(\pi, \pi)$  ordered, due to a Stoner instability.

Like the mentioned bond patterns in one dimension, also in two dimensions on a square lattice a spontaneous breaking of the  $C_4$  lattice symmetry by a valence bond solid phase (VBS) is expected at small phonon frequencies [55]. In contrast, another ground state is expected if large frequencies are considered. In the anti-adiabatic limit, the phonon mass  $m$  vanishes and therefore  $\omega_0 \rightarrow \infty$ , the phonons can be integrated out and yield an exact effective Hamiltonian [62]

$$\hat{H}_\infty = -t \sum_b \hat{K}_b - \frac{\tilde{g}^2}{4} \sum_b \hat{K}_b^2, \quad (6.2)$$

with the electronic hopping operator

$$\hat{K}_b := \sum_\sigma \left( \hat{c}_{i(b),\sigma}^\dagger \hat{c}_{j(b),\sigma} + \hat{c}_{j(b),\sigma}^\dagger \hat{c}_{i(b),\sigma} \right). \quad (6.3)$$

Here we use  $i(b)$  and  $j(b)$  to label the neighboring lattice sites according to the bond  $b$ . Furthermore, as shown in Ref. [60] it holds

$$\sum_b \hat{K}_b^2 \propto \sum_b \left( \hat{\mathbf{s}}_{i(b)} \cdot \hat{\mathbf{s}}_{j(b)} + \hat{\boldsymbol{\eta}}_{i(b)} \cdot \hat{\boldsymbol{\eta}}_{j(b)} \right), \quad (6.4)$$

considering (pseudo-)spin vector operators  $\hat{\mathbf{s}}_{i(b)}$  and  $\hat{\boldsymbol{\eta}}_{i(b)}$ . Thereby,  $\hat{H}_\infty$  reflects the O(4) symmetry and we expect the AFM/CDW/SC phase as ground state for high frequencies [60]. According to the Mermin-Wagner theorem [63] the AFM/CDW/SC phase can be only stable at zero temperature, because it breaks the continuous rotation symmetry of the spins. In contrast, the VBS phase breaks the discrete lattice symmetry and can be preserved at finite temperatures.

Meanwhile, very strong couplings between electrons and phonons are beyond the physical motivation of the SSH model but connect the theory of a condensed matter phonon model to the subject of high energy physics and gauge field physics. Unfortunately, due to numerical issues we observed a drop in the performance of the HQMC method for very strong couplings. Fortunately, increasing  $g$  is not the only way to achieve simulation results for strong interactions between electrons and phonons in the SSH model. Instead of increasing  $g$  we can lower the tight binding hopping  $t$  to study the strong interaction regime. At  $t = 0$  we reach the limiting case of a (unconstrained)  $\mathbb{Z}_2$  gauge field theory on the square lattice.

In this chapter we discuss the SSH model with  $t = 1$  and address the case  $t = 0$  in Chapter 7.

## 6.3 Mean Field Results

In order to motivate the valence bond solid phase (VBS) and discuss possible bond patterns we take a look at a mean field description of the SSH model in the adiabatic limit  $\omega_0 = 0$ . Although the mean field results are not as general as Monte Carlo results we address them to prepare the ground for a detailed discussion of the simulation results and connect to other mean field studies. Starting point is the SSH Hamiltonian in the adiabatic limit, therefore  $m \rightarrow \infty$  to achieve  $\omega_0 = 0$ . If the phonon mass goes to infinity, it suppresses the phonon momentum operators in the Hamiltonian, resulting in

$$\hat{H}_{\text{MF}} = \sum_b \left( \tilde{g}\phi_b - t \right) \hat{K}_b + \sum_b \phi_b^2. \quad (6.5)$$

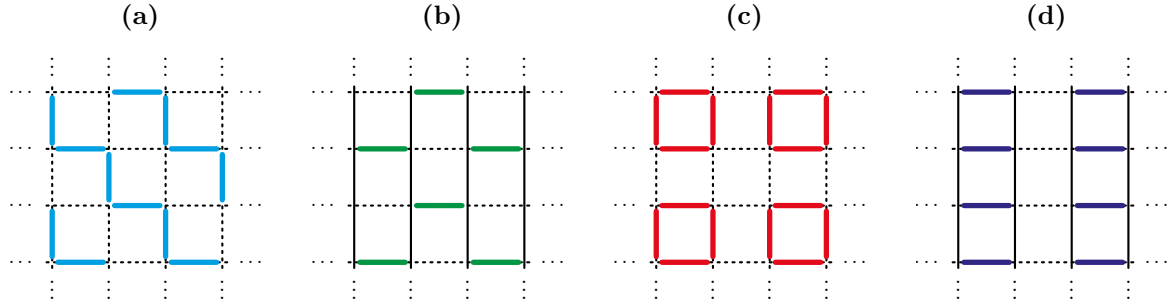


**Figure 6.4:** Patterns as discussed in Ref. [55]. Strong bonds are colored, weak bonds are dotted and unchanged bonds are represented by solid lines.

Here we used the substitutions introduced in Eq. (5.16). Due to the mean field approach the bond operators  $\hat{Q}_b$  got replaced by classical variables  $\phi_b$ . In contrast to previous mean field studies of the SSH model at  $\omega_0 = 0$ , see e.g. Refs. [55, 56, 57, 58, 64, 65], we use a slightly different and more flexible approach. In Ref. [55], the authors assume several bond patterns and compare them with each other to determine the ground state. Therefore, they replace the term  $(\tilde{g}\phi_b - t)$  in Eq. (6.5) by  $-t(1 \pm \delta)$  and neglect  $\phi_b^2$ . Fig. 6.4 shows the patterns discussed in Ref. [55]. The patterns in the subplots of Fig. 6.4 show sequentially:  $(\pi, \pi)$  ordering in the  $x$  and  $y$  bonds simultaneously,  $(\pi, \pi)$  ordering only in the  $x$  bonds and unchanged bonds in the  $y$  direction,  $(\pi, 0)$  bond ordering in the  $x$  direction together with  $(0, \pi)$  ordering of bonds oriented in the  $y$  direction and finally a  $(\pi, 0)$  pattern for bonds in the  $x$  direction only.

In Ref. [55], the authors claim the  $(\pi, \pi)$  ordered pattern of Fig. 6.4b as ground state. Later on a discussion about this opened in Refs. [66, 67]. Arguments how the missing  $\phi_b^2$  terms should be included are presented and the pattern in Fig. 6.4a was supposed to be the ground state.

As mentioned, we make use of a more flexible approach. Instead of varying a single  $\delta$  to find the minimal energy of predefined patterns, we use more degrees of freedom to achieve a mean field solution without proposing a pattern and include the  $\phi_b^2$  terms of Eq. (6.5).

Supposing a VBS state, we have to choose the unit cell, and therefore the according Brillouin zone, in a proper way. To allow several bond patterns, with modulations according to  $(\pi, \pi)$  or  $(\pi, 0)$ , we double the lattice vectors of the square lattice  $\vec{a}_x$  and  $\vec{a}_y$

$$\begin{aligned}\vec{a}_1 &= 2\vec{a}_x \\ \vec{a}_2 &= 2\vec{a}_y.\end{aligned}\tag{6.6}$$

In the following we will label the four lattice sites that are contained in a single unit cell as

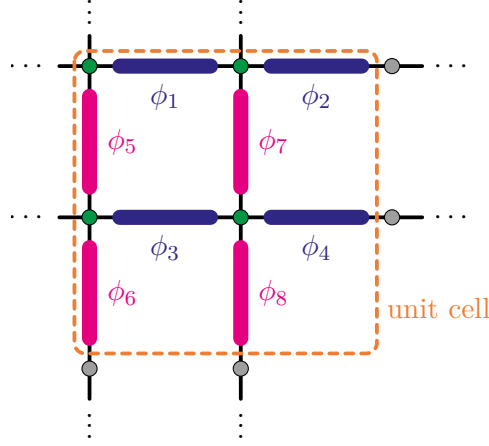


**Figure 6.5:** The unit cell of the mean field ansatz is chosen to be four times larger than the original one to capture different VBS orders.

sublattice sites  $A$ ,  $B$ ,  $C$  and  $D$ . Fig. 6.5 illustrates the arrangement of the eight phonic bond variables  $\phi_b$  contained in the new unit cell.

Assuming periodic boundary conditions leads to the Fourier space representation

$$\hat{H}_{\text{MF}} = \sum_{k \in \text{BZ}} \sum_{\alpha, \beta} \sum_{\sigma} \hat{c}_{\alpha, \sigma}^{\dagger} h_{\alpha, \beta}(k) \hat{c}_{\beta, \sigma} + N_x N_y \sum_{b=1}^8 \phi_b^2 \quad (6.7)$$

with

$$h_{\alpha, \beta}(k) = \begin{pmatrix} 0 & (\tilde{g}\phi_1 - t) + (\tilde{g}\phi_2 - t)e^{-ik_x} & (\tilde{g}\phi_5 - t) + (\tilde{g}\phi_6 - t)e^{-ik_y} & 0 \\ (\tilde{g}\phi_1 - t) + (\tilde{g}\phi_2 - t)e^{ik_x} & 0 & 0 & (\tilde{g}\phi_7 - t) + (\tilde{g}\phi_8 - t)e^{-ik_y} \\ (\tilde{g}\phi_5 - t) + (\tilde{g}\phi_6 - t)e^{ik_y} & 0 & 0 & (\tilde{g}\phi_3 - t) + (\tilde{g}\phi_4 - t)e^{-ik_x} \\ 0 & (\tilde{g}\phi_7 - t) + (\tilde{g}\phi_8 - t)e^{ik_y} & (\tilde{g}\phi_3 - t) + (\tilde{g}\phi_4 - t)e^{ik_x} & 0 \end{pmatrix} \quad (6.8)$$

The indices  $\alpha$  and  $\beta$  in Eq. (6.7) sum over the sublattices  $A$ ,  $B$ ,  $C$  and  $D$ . The variables  $N_x$  and  $N_y$  represent the lattice size in  $x$  and  $y$  direction in terms of the  $2 \times 2$  unit cell. The mean field solution corresponds to the global minimum of the energy as a function of the phonic variables  $\phi_b$ . A diagonalization of the matrix  $h_{\alpha, \beta}$  yields the sorted eigenvalues  $\lambda_1(k, \phi) \leq \lambda_2(k, \phi) \leq \lambda_3(k, \phi) \leq \lambda_4(k, \phi)$ . Considering half filling and taking the spin summation into account we can write the energy function, normalized to a single lattice site, as

$$E_{\text{MF}}(\phi) = \frac{1}{2N_x N_y} \sum_{k \in \text{BZ}} [\lambda_1(k, \phi) + \lambda_2(k, \phi)] + \frac{1}{4} \sum_{b=1}^8 \phi_b^2. \quad (6.9)$$

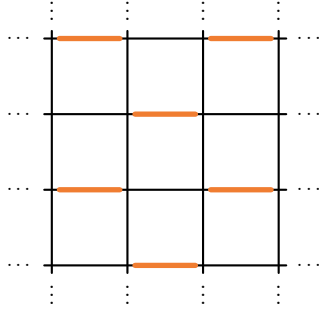


**Figure 6.6:**  $(\pi, \pi)$  VBS pattern according to our mean field approach. Strong bonds are colored while weak bonds are represented by solid lines.

In order to check our implementation we compared the energy of the free system and predefined patterns with results from Ref. [55]. Here we took into account that the authors also neglected the  $\phi_b^2$  terms in this specific publication and reproduced the benchmark data. Contrary to the expectations in Refs. [66, 67], we achieve the lowest energy according to the  $(\pi, \pi)$  pattern of Fig. 6.4b for including the  $\phi_b^2$  terms. For more detailed discussions about the patterns of Fig. 6.5 we refer to the literature, see e.g. Refs. [57, 58].

From now on we do not restrict ourselves to predefined patterns. Instead we are using all degrees of freedom to find the ground state. Due to the  $C_4$  lattice symmetry, the global minimum of the energy function in Eq. (6.9) is four-fold degenerate. Minimizing the mean field energy for a given set of parameters reveals a  $\phi$  field configuration that can be interpreted as a VBS pattern. Table 6.1 shows a sample ground state configuration of  $\phi$ .

$\phi_1$	$\phi_2$	$\phi_3$	$\phi_4$	$\phi_5$	$\phi_6$	$\phi_7$	$\phi_8$
-1.26	-0.32	-0.32	-1.26	-0.32	-0.32	-0.32	-0.32

**Table 6.1:** A sample mean field solution for  $t = 1.0$ ,  $\tilde{g} = 1.5$  and  $N_x = N_y = 50$ .

In general, the phonons strengthen the electronic hopping on all bonds. However, two bonds dominate. The values on the first and fourth bond are much larger than the others. Every lattice site has only one strong bond and three relatively weak bonds, see Fig. 6.6. The pattern of strong bonds corresponds to a  $(\pi, \pi)$  ordering as expected from the shape of the Fermi surface in Fig. 6.3.

Proceeding from this mean field observation we will show how the ground state evolves at finite phonon frequencies  $\omega_0$  using the HQMC method.

## 6.4 Frequency-dependent phase transition

After discussing the symmetries of the model and considering the mean field results for the adiabatic limit, we move on to the two-dimensional SSH model at finite frequencies. Because this chapter is dedicated to the frequency-dependent transition we keep the electron-phonon coupling fixed at  $\tilde{g} = 1.5$  if not stated otherwise. In the following, we use the HQMC method as introduced in Chapter 5 to simulate the SSH model in two dimensions with periodic boundaries. To improve the performance of our implementation we use an additional checkerboard decomposition as explained in detail in Appendix A.

Initially, we take a closer look at several structure factors. The structure factor  $S_O(\vec{q})$  of an operator  $\hat{O}$  is the Fourier transformed auto correlation function of  $\hat{O}$  and can be used to detect long range ordered phases. Due to the square lattice of our model we use a discrete Fourier transformation and the structure factor is given by

$$S_O(\vec{q}) = \sum_{\vec{r}} e^{-i\vec{q}\vec{r}} \left( \langle \hat{O}_i(\tau) \hat{O}_j(\tau) \rangle - \langle \hat{O} \rangle^2 \right). \quad (6.10)$$

with  $\vec{r} = \vec{r}_j - \vec{r}_i$ . In case of a long range ordered phase the structure factor shows a peak that diverges with the system size below the critical temperature.

To check for a VBS phase we can look at the structure factors of the electronic bond hopping operator  $\hat{K}_b$  or the phononic displacement operator  $\hat{X}_b$ . Like for all observables that are derived from the single particle Green's function by Wick's theorem, the HQMC method involves a stochastic inversion to measure  $\hat{K}_b$ . The phononic displacement observables are more accessible. We can simply use the  $\tilde{x}$  configurations the HQMC method samples to calculate correlation functions and structure factors. To detect the AFM/CDW/SC phase we can check the structure factors of the spin operator  $\hat{s}_i^z$  as well as the structure factor of the occupation number operator  $\hat{n}_i$ . Besides the equal time structure factor we can also make use of the according susceptibility as defined by

$$\chi_s(\vec{q}) = \int_0^\beta d\tau \sum_{\vec{r}} e^{-i\vec{q}\vec{r}} \left( \langle \hat{s}_i^z(\tau_1) \hat{s}_j^z(\tau_2) \rangle - \langle \hat{s}^z \rangle^2 \right), \quad (6.11)$$

for spin-spin correlations with  $\tau = \tau_2 - \tau_1$ .

The two subplots (a) and (b) of Fig. 6.7 illustrate on a path through the first Brillouin zone how the peak of the susceptibilities grows with the size of the lattice at a certain temperature. In addition, the subplots (c)-(f) show the structure factors for different values of the phonon frequency  $\omega_0$ . Plots of corresponding susceptibilities are presented in the subplots (g)-(i) of Fig. 6.7.

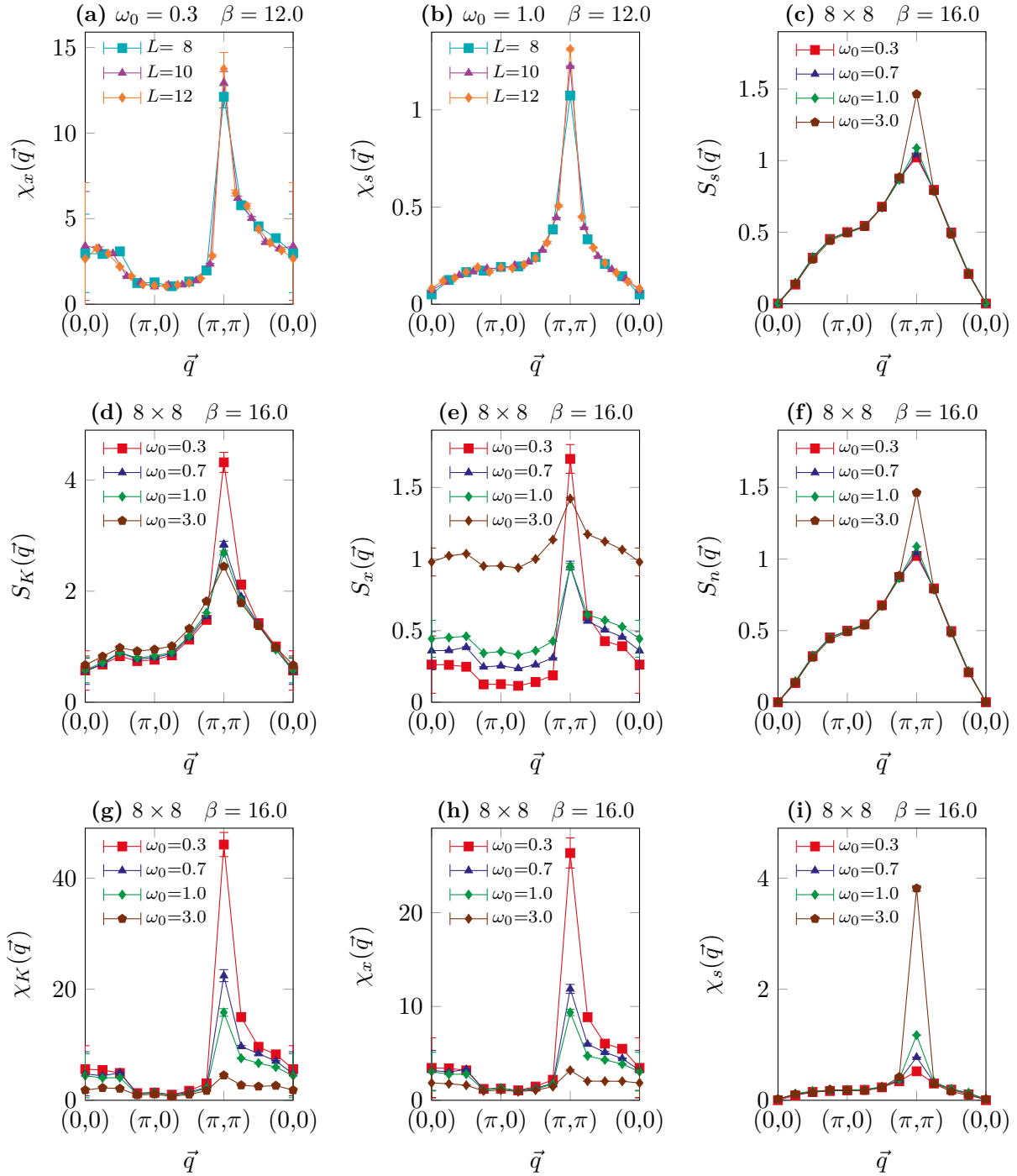


**Figure 6.7:** (a)-(b): Susceptibilities for different  $L \times L$  lattice sizes with  $t = 1.0$ ,  $\beta = 12.0$  and  $\tilde{g} = 1.5$  (c)-(i) Structure factors and susceptibilities for several values of  $\omega_0$  on a  $8 \times 8$  lattice with  $t = 1.0$ ,  $\beta = 16.0$  and  $\tilde{g} = 1.5$ .



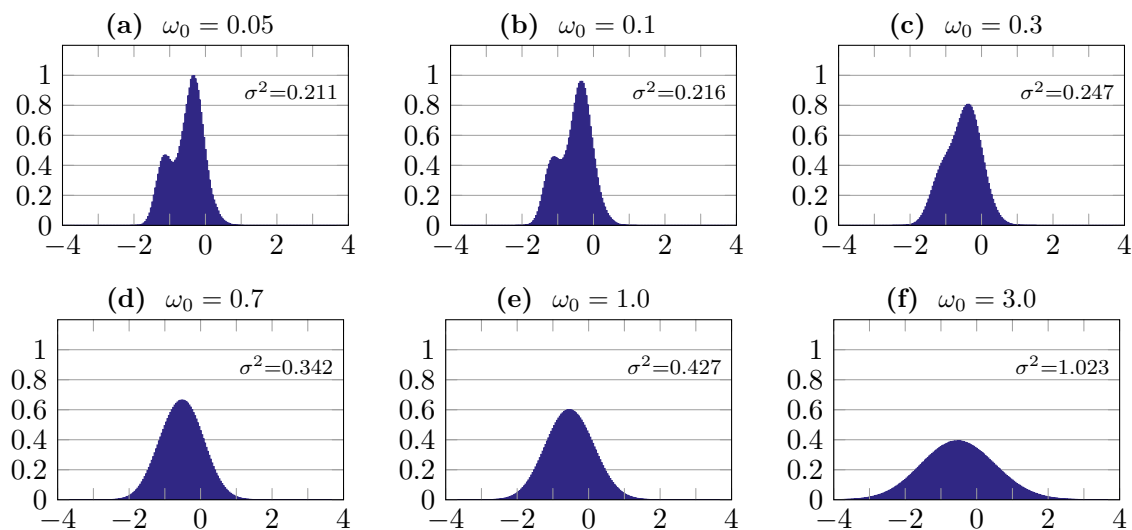


**Figure 6.8:** Histograms and variances of  $x_b$  field distributions for several frequencies  $\omega_0$  on a  $8 \times 8$  lattice with  $t = 1.0$ ,  $\beta = 16.0$  and  $\tilde{g} = 1.5$ . The variances are calculated according to  $\sigma^2 = \langle (\tilde{x} - \langle \tilde{x} \rangle)^2 \rangle$ .

All plots concerning the bond observables  $\hat{X}$  and  $\hat{K}$  in Fig. 6.7 exhibit a clear peak at  $\vec{q} = (\pi, \pi)$  for small frequencies. This observation corresponds to the VBS phase that is expected from mean field theory. For larger frequencies the VBS phase vanishes. In the plots concerning the spin operator  $\hat{s}^z$  and the particle operator  $\hat{n}$  of Fig. 6.7 we can also see a peak at  $\vec{q} = (\pi, \pi)$  that indicates the AFM/CDW/SC phase. Due to the  $O(4)$  symmetry, discussed in Sec. 6.2, the subplots (c) and (f) are identical. Accordingly, we only show data for the spin observables in the following. Furthermore, from now on for simplicity we call the AFM/CDW/SC phase just an AFM phase, being aware of the degeneracy. In contrast to equal time structure factors, susceptibilities suppress background contributions to the critical fluctuations [68], see subplots (g)-(i). It remains to discuss the  $\omega_0$  dependent shift of  $S_x(\vec{q})$  in Fig. 6.7e. An offset in the momentum space is connected to the data in real space at  $\vec{r} = 0$ . In case of the phonon configurations the  $\vec{r} = 0$  correlation functions are identical to the variance of the  $\tilde{x}$  distribution. Fig. 6.8 shows histograms and the according variances of the fields  $\tilde{x}$  for several phonon frequencies  $\omega_0$ . As we see, the variances of the distributions are identical to the shifts in Fig. 6.7e.

In addition, we can use the histograms in Fig. 6.8 to discuss some qualitative behavior of the phonon fields. The distribution of the phonon fields visualize how the VBS order vanishes. At small frequencies the VBS phase is very pronounced. As for the mean field solution in Table 6.1, a quarter of all phonon fields takes significantly smaller values than the others. Those smaller

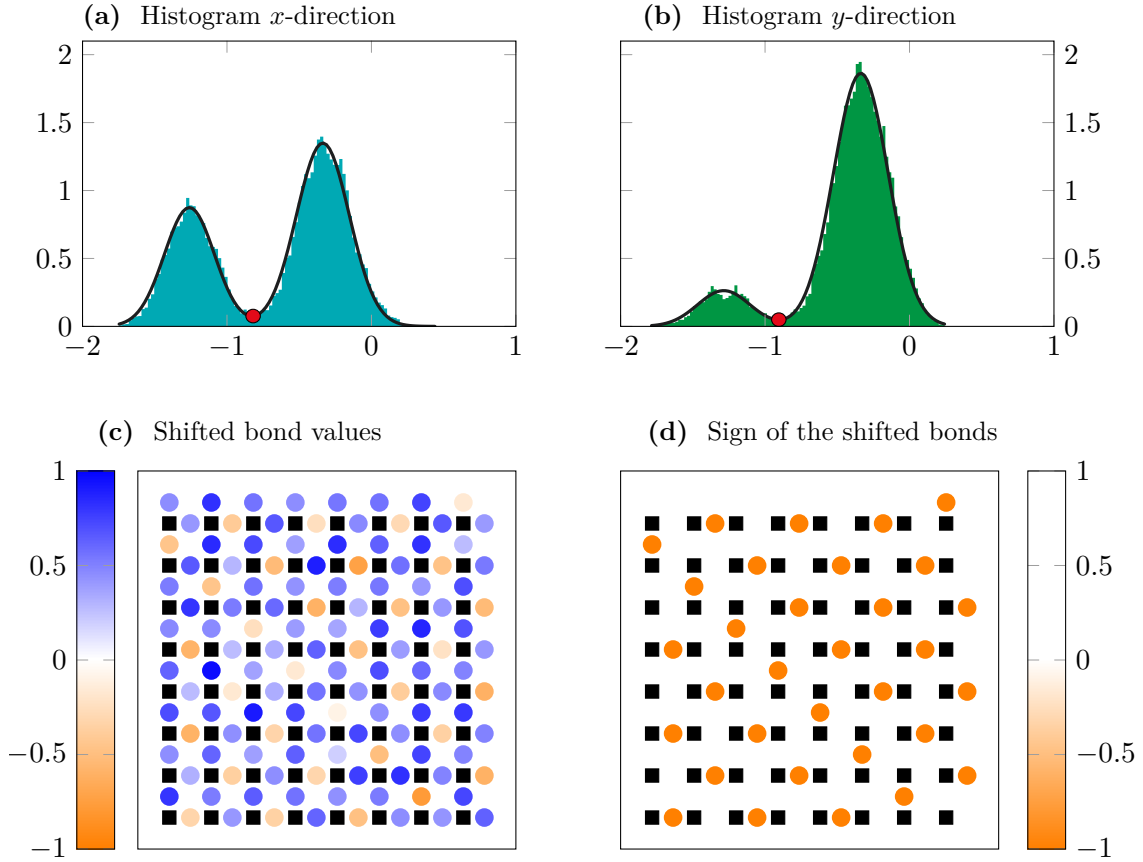


**Figure 6.9:** Bond histograms and snapshot of a single Monte Carlo lattice configuration using  $\omega_0 = 0.1$  on a  $8 \times 8$  lattice with  $t = 1.0$ ,  $\beta = 80.0$  and  $\tilde{g} = 1.5$ . All bond values of the lattice configuration are shifted with respect to the local minimums in the histograms (red points) to distinguish between strong (orange) and weak (blue) bonds.

bond values correspond to the strong bonds in the VBS. Increasing the phonon frequencies lowers the distance between the two peaks until they merge and only a single peak remains in the AFM state. Furthermore, we observe negative mean values for all histograms. This is expected, because the phonons try to lower the energy of the system by a uniform distortion of the lattice. The potential energy costs which are connected to the non-vanishing displacements are compensated by a lowering of the kinetic energy of the electrons. This also agrees with the mean field results in Table 6.1.

To discuss the pattern of the  $(\pi, \pi)$  ordered VBS state in the HQMC simulation we can take a look at a single sample of the Monte Carlo process. In Fig. 6.9 we consider a single bond configuration of  $\tilde{x}$  as sampled by the HQMC method on an  $8 \times 8$  lattice at  $\beta = 80$ ,  $\omega_0 = 0.1$ ,  $\tilde{g} = 1.5$ . Due to

$\Delta\tau = 0.1$  the sample contains  $N_\tau = 800$  lattice configurations, one per  $\tau$ -slice. For a qualitative discussion of the bond pattern we consider the histograms of bond variables in  $x$ - and  $y$ -direction separately. In (a) and (b) of Fig. 6.9 we fitted the histograms of the bond variables with a bimodal Gaussian. To achieve a good fit we use all 800  $\tau$ -slices for the histogram. Because of the term  $\frac{\Delta\tau}{\omega_0^2} \left( \frac{\tilde{x}_{i,l+1} - \tilde{x}_{i,l}}{\Delta\tau} \right)^2$  in Eq. (5.9) fluctuations in imaginary time are rather expensive at small frequencies. Therefore, all  $\tau$ -slices should be similar to each other. The minimum between the two modes in a histogram marks the distinction point between strong and weak bonds. As the histograms show, it seems like there are only a few strong bonds in  $y$ -direction but approximately half of the bonds in  $x$ -direction are strong. Fig. 6.9c illustrates the bond configuration of a single  $\tau$ -slice. Black squares represent the sites of the lattice. The disks between the sites symbolize the bonds. The disk colors encode the strength of the bonds. Here the values of  $\tilde{x}$  are shifted according to the local minimum of the bimodal fit. Weak bonds are blue, while the strong bonds take the orange color. The pattern becomes easier to recognize if only the sign of the shifted bond variables is plotted, as in Fig. 6.9d. The used color map hides the weak bonds and only the strong bonds remain in the picture. The pattern of the Monte Carlo sample is the same as for the mean field solution in Fig. 6.6. In addition, Fig. 6.9d also shows a small domain of a VBS pattern in  $y$ -direction. This is expected for a snapshot of a Monte Carlo configuration and corresponds to the small left peak in the histogram of bonds oriented in  $y$ -direction.

Summarizing what we observed from the histograms, we can distinguish between stronger and weaker bonds in the VBS ground state. The number of weaker bonds is three times larger than the number of strong bonds. Furthermore, the bond pattern of single bond configurations agrees with the staggered mean field pattern. Increasing the phononic frequency  $\omega_0$  the two modes in the histograms continuously get closer to each other and merge. In the AFM phase only a single Gaussian remains and becomes wider if the frequency is enlarged further.

Before discussing further results of the HQMC method we briefly summarize our discussion of the first HQMC results. The structure factors, susceptibilities and histograms show the existence of a  $(\pi, \pi)$  ordered VBS phase at small frequencies. This agrees with the mean field results. At larger frequencies they reveal the expected  $O(4)$  symmetric AFM phase at finite lattices as discussed in Sec. 6.2. Besides the existence of the phases we are also interested in the mechanism of the corresponding phase transitions. Here it is important to notice the kind of broken symmetries. While the AFM state breaks the continuous rotation symmetry of the spins, the VBS state breaks the discrete lattice symmetry. Several scenarios are conceivable.

A first order phase transition could be a candidate to explain the ground state phase transition of the SSH model (Fig. 6.10a). In general the Ginzburg-Landau theory describes second order phase

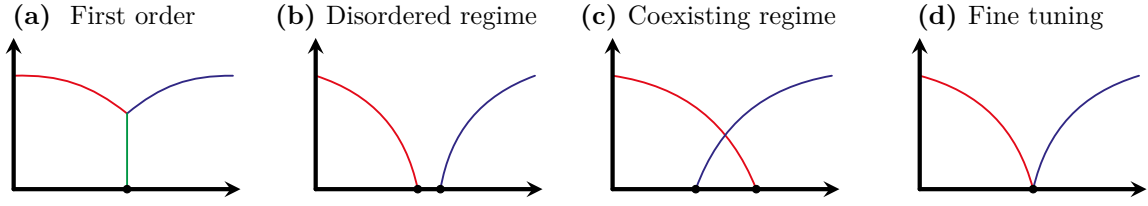


**Figure 6.10:** Sketch of the four different scenarios that are possible inside the framework of Ginzburg-Landau theory.

transitions of single order parameters. It does not connect several ground states breaking different symmetries with each other. In this framework a coexisting or a disordered regime between the VBS and AFM phase is expected, see sketches in Fig. 6.10b and Fig. 6.10c. Only a fine tuning of the parameters could cause a direct transition in Ginzburg-Landau theory, see Fig. 6.10d. Another concept that describes a continuous and direct phase transition between VBS and AFM states is the so called deconfined quantum critical point (DQCP) [69, 70]. Proposed for spin systems it describes how the vortices of a VBS ordered phase, carrying a spin degree of freedom, condense at the critical point and lead to the AFM phase.

In the next step we look at further bond observables. We can use the field  $\tilde{x}$  to define an effective hopping parameter for each bond

$$t_b^{\text{eff}} = t - \tilde{g} \tilde{x}_b. \quad (6.12)$$

Although we do not expect a  $\pi$ -flux state [71] at  $t = 1.0$ , we can use the effective hopping to check it. If the products of the four hopping parameters according to each plaquette of the square lattice are negative, it is called a  $\pi$ -flux state. In order to investigate a possible  $\pi$ -flux phase, we take the mean of all plaquette products of the effective hoppings

$$f_\pi(\tilde{x}) = \frac{1}{L_x L_y} \sum_{\square} \prod_{b \in \square} t_b^{\text{eff}}. \quad (6.13)$$

Fig. 6.11 shows the averages of several bond observables for different lattice sizes, temperatures and frequencies. The expectation value of the electronic hopping  $\langle \hat{K} \rangle$ , Fig. 6.11a, is approximately constant at small frequencies and decreases in the AFM phase. As mentioned before, negative  $\tilde{x}_b$  values can be interpreted as strengthening of the electronic hopping. So the behavior of  $\langle \hat{K} \rangle$  agrees with the behavior of the mean value of the phononic bond variables  $\tilde{x}$ , Fig. 6.11b. The mean of the fields is always negative but grows especially in the AFM phase slowly. Fig. 6.11c illustrates the behavior of the  $\pi$ -flux function  $f_\pi$ . As expected it shows no indications for a  $\pi$ -flux

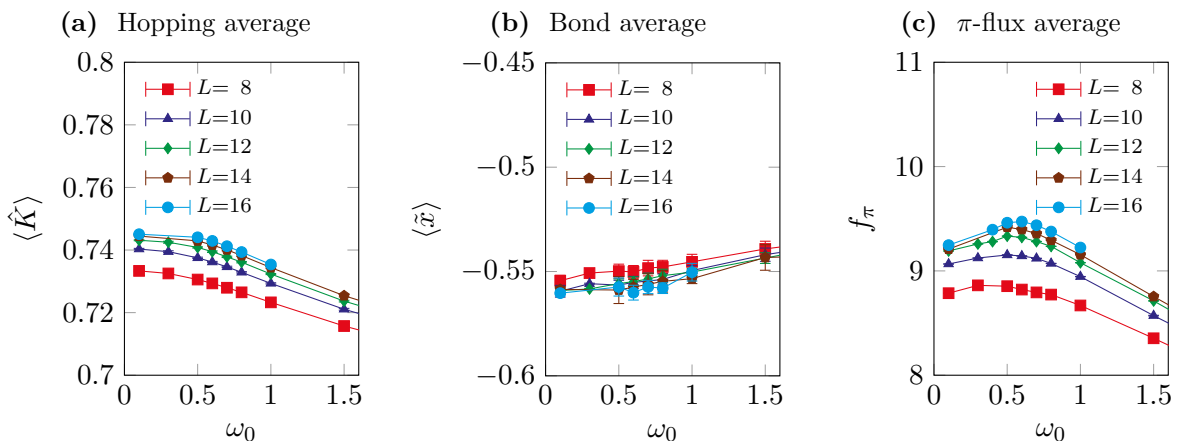


**Figure 6.11:** Bond observables for  $L \times L$  lattices with  $t = 1.0$ ,  $\beta = L$  and  $\tilde{g} = 1.5$ .

state. However, it exhibits a maximum in the  $\omega_0$  regime where we observe the phase transition between the VBS and AFM phase.

Another useful tool to investigate phase transitions in finite size systems is the so called correlation ratio [72]. It takes the structure factor or susceptibility of an observable and converts the information to a number between 0 and 1. Numbers close to 1 indicate a long range ordered phase. Taking the spin susceptibility as an example, the correlation ratio is defined by

$$R_{\chi_s} = 1 - \frac{\chi_s(\vec{q}_0 + \vec{\delta})}{\chi_s(\vec{q}_0)}. \quad (6.14)$$

Here  $\vec{q}_0$  labels the momentum vector according to the ordered state, and  $\vec{\delta}$  is the smallest momentum vector that can be resolved by the size of the lattice. Furthermore, the correlation ratio is invariant under the renormalization group (RG) flow by construction. For an  $L \times L$  lattice and a critical frequency  $\omega_c$ , the correlation ratio can be written as a scaling function

$$R \simeq F_{\text{RG}}\left(\frac{L^z}{\beta}, (\omega_c - \omega_0)^\nu\right), \quad (6.15)$$

with critical exponent  $\nu$  and dynamical scaling exponent  $z$ . The structure factor/susceptibility exhibits a peak at  $\vec{q}_0$  if the system is in an ordered state. In case of a long range ordered phase the peak diverges below the critical temperature for increasing the system size. Fig. 6.12 sketches how the correlation ratio works. If no long ranged ordered phase is established, the correlation function has similar values at  $\vec{q}_0$  and the neighboring points in the momentum space. This means the fraction term in  $R$  is close to 1 and  $R$  itself vanishes. In the case of a long range ordered phase

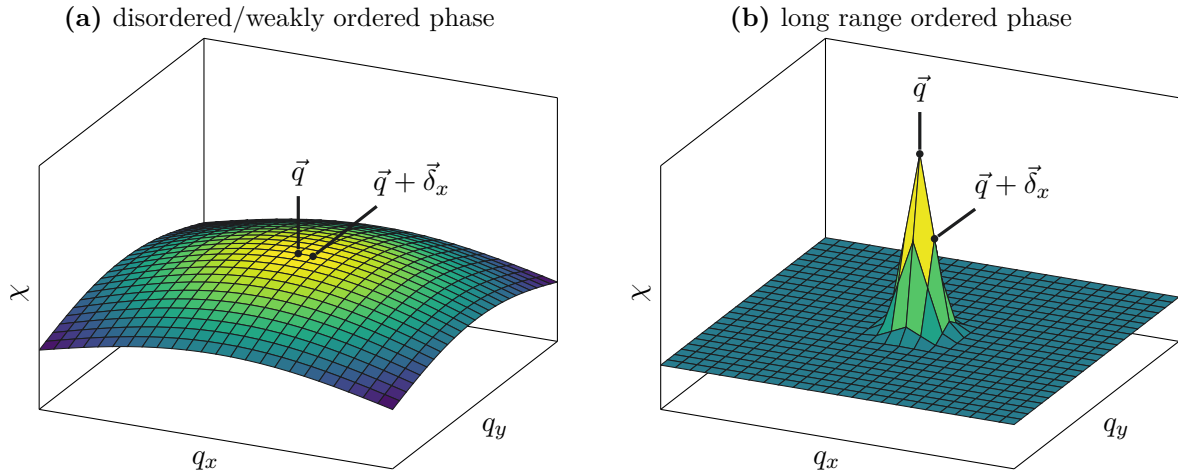


**Figure 6.12:** Schematic plots of the susceptibility for a disordered and ordered phase.

the fraction becomes smaller and  $R$  approaches 1 for increasing lattice sizes. In the following we will use the correlation ratio  $R$  to decide if a long range ordered state is present or not. If  $R$  is larger for a given lattice size compared to its value on a smaller lattice the physical system is in an ordered state. Otherwise the system is disordered or in a phase according to a different observable. Naturally, the correlation ratio changes if parameters of the systems are varied. A phase transition takes place where the correlation ratios of different lattice sizes are crossing. The dynamical exponent  $z$  is important, because it influences the crossing of the correlation ratio.

Unfortunately, we have no clear indications for  $z$  in the two-dimensional SSH model. In case of the DQCP scenario a dynamical scaling exponent of  $z = 1$  is expected [70]. For the moment we use this as an assumption to discuss correlation ratios and potentially determine a critical frequency.

For the next step we take a look at the correlation ratios of the structure factors and susceptibilities in Fig. 6.13. Overall, all subfigures confirm the VBS phase at small frequencies and the AFM phase at large frequencies. Some of the plots like (a) show a very strong lattice size dependent drift in the crossings of the ratios. Others, like (b) or (c) exhibit a clear crossing point. Taking the shifts into account, all correlation ratios support a critical value of  $\omega_c \approx 0.7$ . Furthermore, we have no indication for a first order transition. All correlation ratios are smooth and illustrate a continuous and most probably direct transition between the VBS and AFM phase.

The simplest way to exclude the fine tuning scenario is to change the electron-phonon coupling that was fixed to  $\tilde{g} = 1.5$  up to now. Larger value of  $\tilde{g} = 1.75$  should strengthen the VBS phase and shift the transition to larger frequencies. Fig. 6.14 shows the correlation ratios for  $\tilde{g} = 1.75$ .

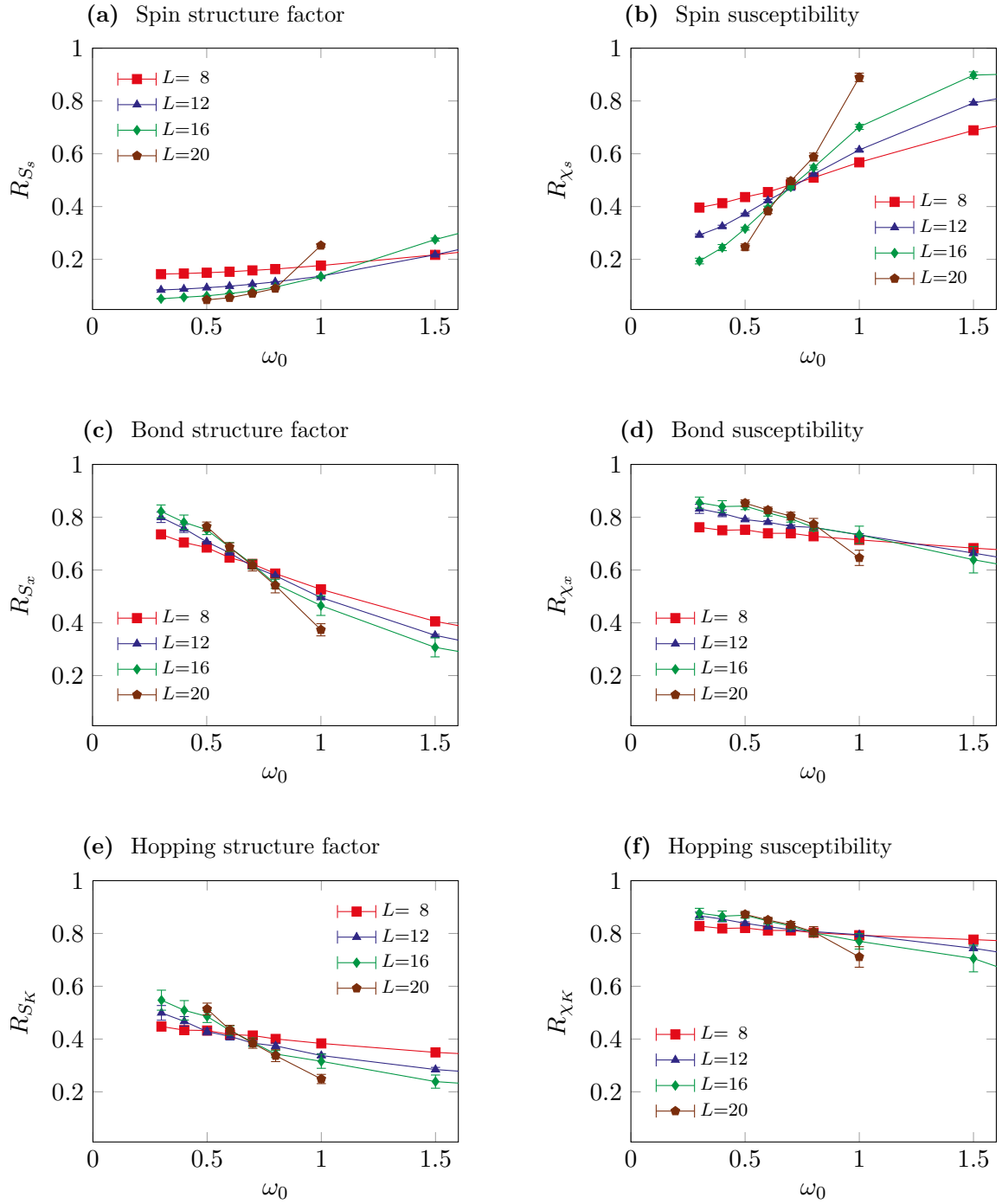


**Figure 6.13:** Correlation ratio for several observables. In all plots we use lattice sizes of  $L \times L$  and  $\beta = L$  with  $\tilde{g} = 1.5$  and  $\Delta\tau = 0.1$ .

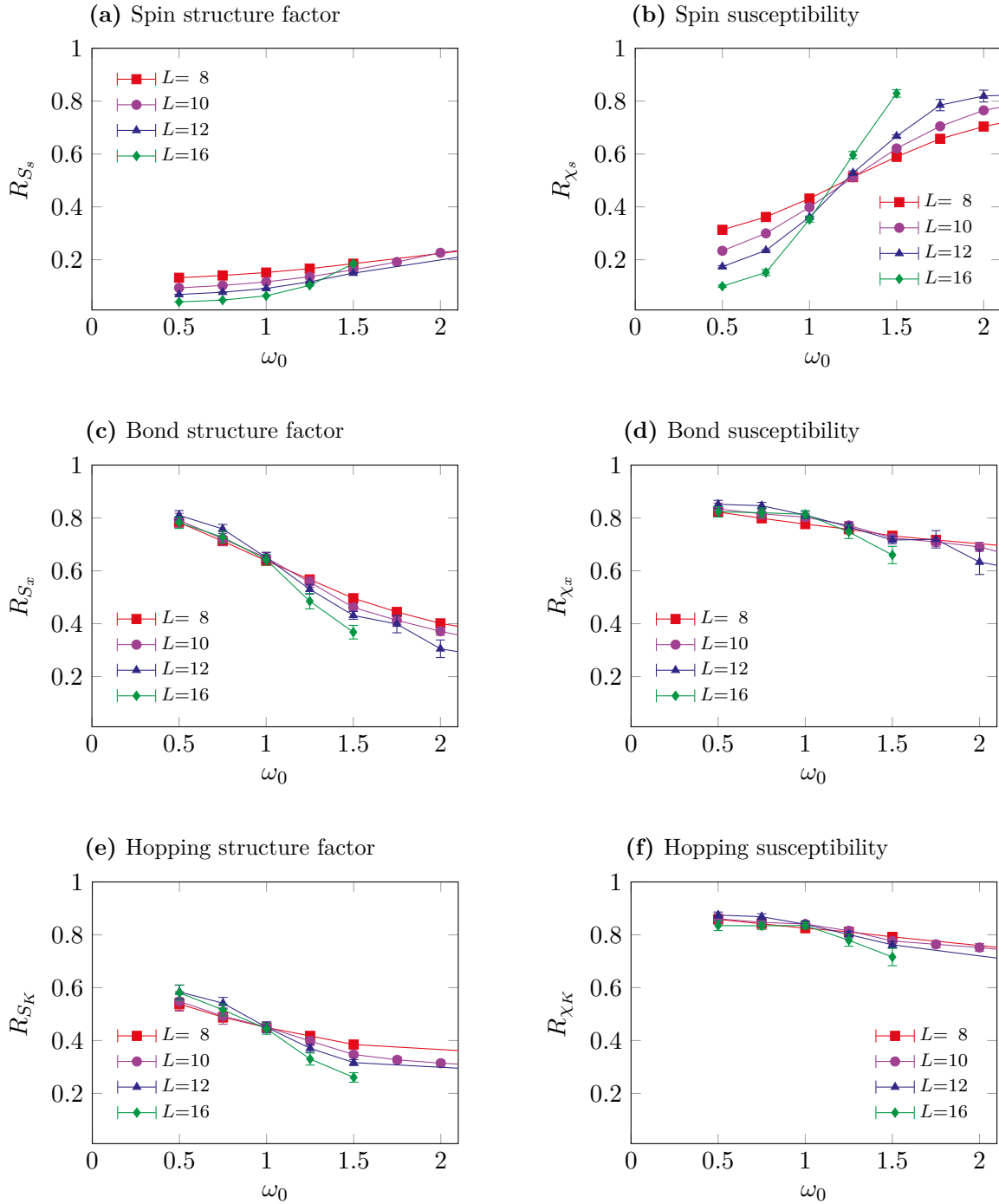


**Figure 6.14:** Correlation ratios for  $\tilde{g} = 1.75$ . In all plots we use lattice sizes of  $L \times L$  and  $\beta = L$  with  $\Delta\tau = 0.1$ .



If we take the finite size drift of the crossings into account a critical frequency of  $\omega_c \approx 1.0$  seems reasonable for all observables in Fig. 6.14.

Summarizing the observations from the correlation ratios, we observe apparently single transitions. So far this seems to be compatible with a DQCP interpretation of the phase transition.

In order to check our assumption of  $z = 1$ , we make use of a possibility to determine the dynamical exponent  $z$  as pointed out in Ref. [73, 74]. We have to compare Monte Carlo results of the spin susceptibility  $\chi_s$  with the predicted behavior in  $d$  dimensions at  $\omega_c$

$$\chi_s(\vec{q} = 0) \propto T^{\frac{d}{z}-1}. \quad (6.16)$$

In our case,  $d = 2$ , this means  $z = 1$  if  $\chi_s(\vec{q} = 0)$  vanishes linearly when the temperature  $T$  goes to zero. Fig. 6.15 shows the temperature behavior of  $\chi_s(\vec{q} = 0)$  for different frequencies and lattice sizes. The linear scaling is only expected at the critical point. We assume  $\omega_c \simeq 0.7$ . This is compatible with our observations from the correlation ratios as well as for the histograms, structure factors and susceptibilities. Subplots (a)-(c) show the spin susceptibility itself. To identify linear behavior, we multiplied the susceptibilities with the inverse temperature  $\beta$  and show them in (d)-(f). Subfigures (a) and (d) show that the spin susceptibility at  $\omega_0 = 0.3$  vanishes according to a non-linear behavior. At  $\omega_0 = 0.7$ , the data of subplots (b) and (e) propose the required linear behavior for the  $10 \times 10$  and  $12 \times 12$  lattice. However, the smaller  $8 \times 8$  lattice probably suffers from size effects and shows another result. For  $\omega_0 = 1.0$  in (c) and (f) it is hard to determine the exact behavior of the spin susceptibility due to the quality of the data. As shown e.g. in Ref. [60] for another model, the expectation is to see it vanishing slower compared to linearity. Again the  $8 \times 8$  lattice seems to be too small. Taking the error bars into account, also the expected growth of  $\beta\chi_s(\vec{q} = 0)$  in (f) for small temperatures can not be clearly identified. Attempts to improve the data turned out to be very challenging. We made the experience that sampling very small quantities like here can be difficult for the HQMC method. The stochastic inversion we are using for all measurements based on Green's function introduces a small amount of additional stochastic noise. In general, if large quantities are measured this is of no consequence. In case of very small quantities, like here, the noise of the stochastic inversion takes effect. To reduce this noise we have to compute many more samples inside a stochastic inversions. At a certain point, when the computing of the measurements requires more effort than the Monte Carlo updates, this slows down the performance of the HQMC method and we stopped to improve the data.

Eventually, being aware of the uncertainty, we remain with our assumption of  $z = 1$  due to two reasons: Fig. 6.15 also does not clearly disprove the assumption and we know  $z = 1$  is the correct

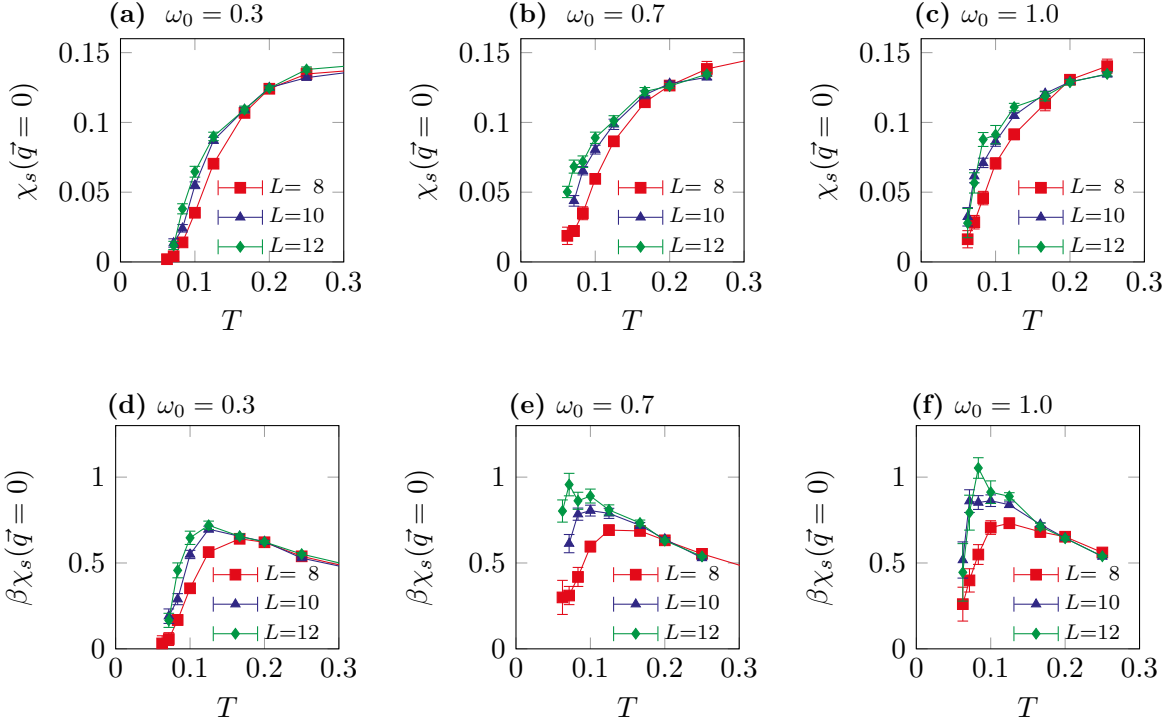


**Figure 6.15:** Low temperature behavior of the spin susceptibility.

choice of the DQCP scenario [70] we discuss later.

Up to now we only investigated the behavior of observables connected to the order parameters of the VBS and AFM phase. The Monte Carlo data of the last observable we want to discuss here are more general. The single particle Green's function provides insights to the electronic band structure. Especially, we can use it to discuss the size of the single particle gap  $\Delta$  during the phase transition. The local Green's function at  $\tau = \frac{\beta}{2}$  provides information about the size of the gap. Smaller values of the Green's function correspond to larger gap sizes. Fig. 6.16 shows how the local imaginary time Green's function changes during the transition. Starting at small frequencies in the VBS phase the single particle gap is clearly present. Increasing the frequency lowers the gap size and the Green's function at  $\tau = \frac{\beta}{2}$  takes larger values. The system has to be deep inside the AFM regime to get to a gap of the size as observed in the VBS state. Neither a closing nor a lowering of the single particle gap is expected by the bosonic theory of DQCP [69].

Moreover, we can use the spectral representation of the Green's function

$$G(\tau) = \int_{-\infty}^{\infty} d\omega \frac{e^{-\tau\omega}}{1 + e^{-\beta\omega}} A(\omega) \quad (6.17)$$

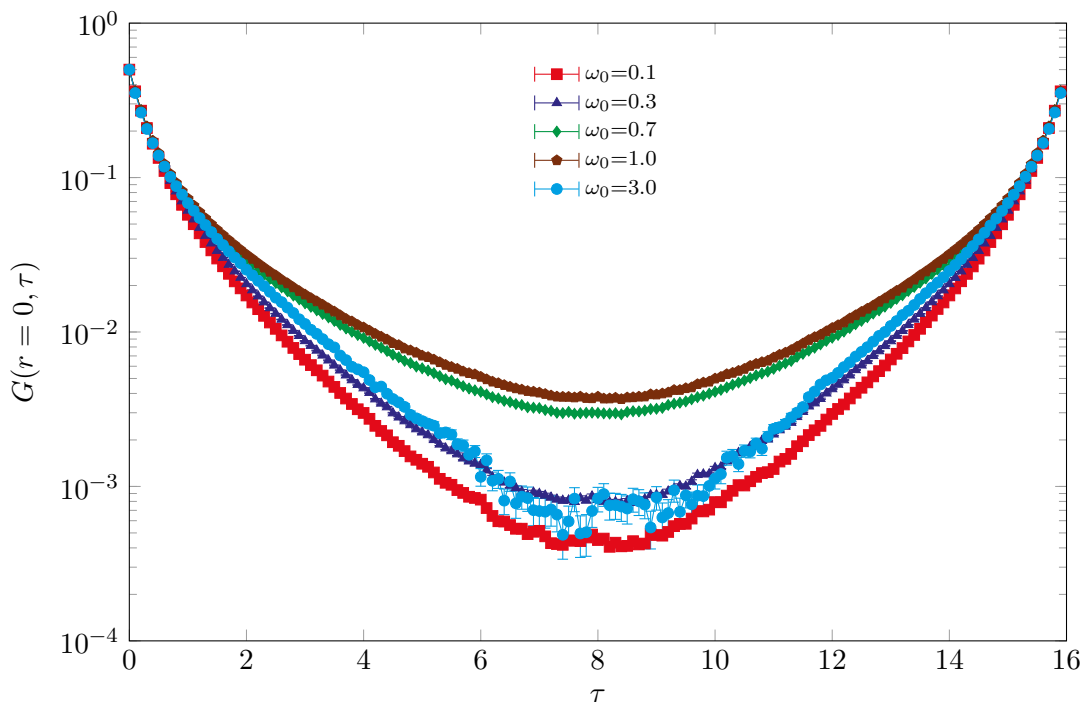


**Figure 6.16:** Local Green's function for several phonon frequencies  $\omega_0$  on a  $8 \times 8$  lattice with  $\tilde{g} = 1.5$ ,  $\beta = 16.0$  and  $\Delta\tau = 0.1$ .

to approximate the density of states  $N(\omega)$  at  $\omega = 0$ . As pointed out in Ref. [75], assuming a gapped system and small temperatures the density of states is

$$N(0) \propto \beta G\left(\vec{r} = 0, \tau = \frac{\beta}{2}\right). \quad (6.18)$$

At zero temperature and  $\omega = 0$  the density of states has to vanish in an ordered state. For finite temperatures we expect that thermal fluctuations cause a finite  $N(0)$  according to

$$N(\omega = 0, T) \propto e^{-\frac{\Delta}{T}}. \quad (6.19)$$

Simulation results of  $\beta G\left(\vec{r} = 0, \tau = \frac{\beta}{2}\right)$  for several phonon frequencies  $\omega_0$  and as function of temperature  $T$  are plotted in Fig. 6.17. Besides the considered  $e^{-\frac{\Delta}{T}}$  behavior they also show smaller gap sizes close to the phase transition for all lattice sizes and for all temperatures.

Concluding from our HQMC simulation results, we observe a continuous and most likely direct transition between a staggered  $(\pi, \pi)$  VBS phase and the  $O(4)$  symmetric AFM phase. Furthermore we observed a suppression of the single particle gap in the parameter regime of the transition.

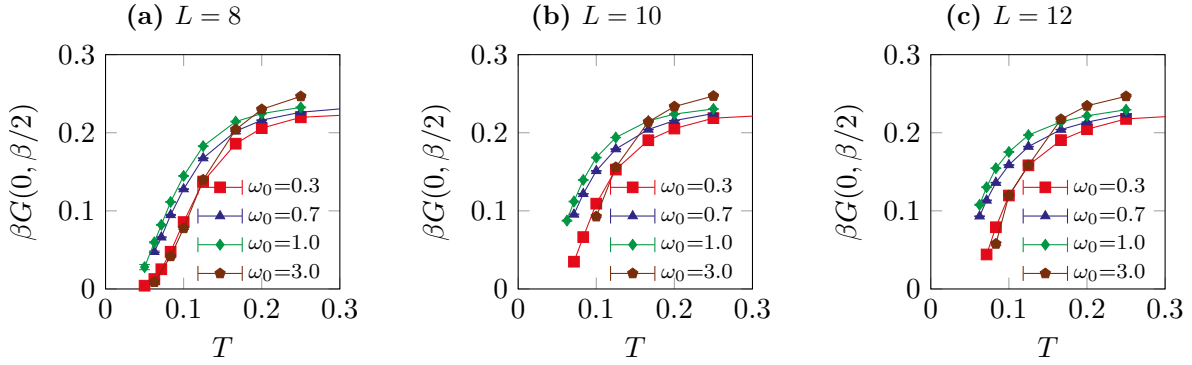


**Figure 6.17:** Susceptibilities of the local Green's functions at  $\tau = \frac{\beta}{2}$  for different lattice sizes and phonon frequencies  $\omega_0$  at  $\tilde{g} = 1.5$

Interestingly, this behavior seems not to fit with any of our previous scenarios for the phase transition. Even if in Ref. [76] a first order transition between a staggered  $(\pi, \pi)$  VBS phase and a AFM phase in two dimensions was observed for a Heisenberg model, we see no signs of a first order transition in our data. Moreover, a direct second order phase transition between two phases with different order parameters and breaking different symmetries can not be explained using the usual standard Ginzburg-Landau theory.

Deconfined quantum criticality provides a framework to explain the transition between a VBS and an AFM phase. Contrary to the staggered  $(\pi, \pi)$  VBS (sVBS) ground state of the SSH model, the DQCP theory assumes a columnar  $(\pi, 0)$  ordered VBS (cVBS) state. Although the behavior of the correlation ratios seems to support an interpretation of the phase transition by using the DQCP mechanism, two properties prevent it. First the Fermi surface of the bare model is quadratic and  $(\pi, \pi)$  nested compared to the two Dirac points in case of other DQCP models, see e.g. Ref. [68]. This means the electronic behavior has to play a much more important role in case of the SSH model. Secondly, the patterns of the VBS ground states are different. The cVBS as well as the sVBS ground states are four-fold degenerate. Fig. 6.18a illustrates the vortice of the cVBS pattern. The vortices occur if the domain walls of the four ground state configurations cross each other. Due to the columnar patterns, every vortice between four different bond domains has to carry a spin degree of freedom. In the framework of DQCP those spin degrees of freedom condense at the critical point and order the system to an AFM ground state [69, 70]. This differs from the sVBS pattern. As Fig. 6.18b shows, also the sVBS pattern can form vortices carrying a spin degree of freedom. But in contrast to the cVBS pattern also defects without a spin degree of freedom are possible, see Fig. 6.18c. This is a fundamental difference between the theory of a DQCP and the situation we observe in the two-dimensional SSH model. In addition, the authors

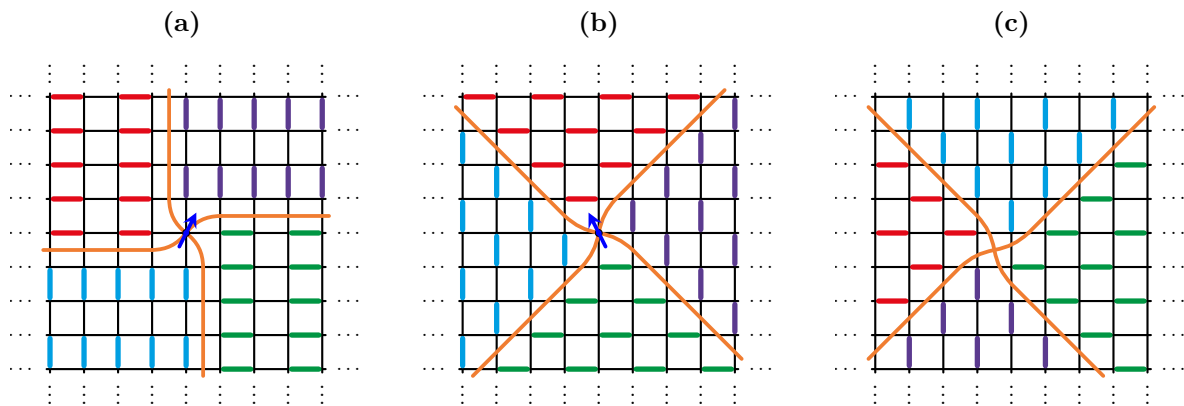


**Figure 6.18:** Defects of the  $(\pi, 0)$  ordered cVBS states (a) and the  $(\pi, \pi)$  ordered sVBS patterns, (b) and (c).

of Ref. [77] investigate the low-energy field theory of sVBS phase and see large differences to the case of cVBS.

Unfortunately, at the end of this chapter we remain without a clear interpretation of the frequency-dependent phase transition in the two-dimensional half filled SSH model. After all, a weak first order transition can not be excluded for sure. A standard DQCP mechanism does not apply. Furthermore, a fine tuned Ginzburg-Landau theory for  $\tilde{g} = 1.5$  seems to be unlikely too.

At the end several scenarios seem to be conceivable to explain our observations. A metallic point exactly at the critical point separating the AFM and VBS phase could be one interpretation consistent with the nesting of the Fermi surface and explain the suppression/closing of the single particle gap. This could be some kind of special fine tuning that occurs for every strength of the coupling. Considering the nesting of the Fermi surface we do also not expect a disordered phase between the VBS and AFM state. However, we can not finally exclude a small regime of coexisting phases. A scenario where the AFM starts to form while the VBS is weakening for increasing the phononic frequency could be an option that fits in the Ginzburg-Landau theory. Finally, also a different mechanism we do not know yet could be responsible for the phase transition. As concluded in Ref. [77], some field theoretical aspects of the staggered VBS phase are still under investigation and may hold some surprises.

In this chapter we provided some first insights into the physics of the half filled two-dimensional SSH model using a Monte Carlo method. We discussed the VBS pattern in a mean field approach as well as for the results of the HQMC method and achieved good agreement. We have shown the  $O(4)$  symmetric AFM state in the simulation results of our Monte Carlo method and we

were able to perform a first-time investigation of the frequency-dependent phase transition in the two-dimensional SSH model.

Further improvements of the HQMC method could help to improve the quality of the data, e.g. for temperature dependent spin susceptibilities. A determination of the dynamical scaling exponent  $z$  could be possible. We have demonstrated the principal capability of the HQMC method to simulate the two-dimensional SSH model, additional improvements could help to reach larger lattice sizes as well as lower temperatures in order to get a deeper understanding of the model in the future.

# 7

## Chapter 7

---

# Zero hopping limit

In the previous chapter we considered the physics of the SSH model as a function of the phononic frequency. Beside the energy of phonons the SSH Hamiltonian also contains the hopping parameter  $t$  and the electron-phonon interaction parameter  $\tilde{g}$ . An obvious question is how the coupling strength influences the physics of the model. In theory arbitrary parameters are possible to simulate by the HQMC method. However, in practice the implementation of our HQMC method is limited. The electron-phonon coupling appears in the exponential function of the  $B$  matrices in Eq. (5.11). Besides the approximation strategies to speed up the computation of those exponential functions in the  $B$  matrices, see Appendix B,  $\tilde{g}$  also influences the condition number of the resulting system of linear equations. As discussed in Sec. 3.5 the condition number affects the CG method which is crucial to achieve a good performance. Therefore, large electron-phonon couplings slow down the method. However, another way to simulate the strong coupling regime is to lower the tight-binding hopping parameter  $t$  while keeping  $\tilde{g}$  fixed.

This chapter focuses on the physics of the SSH model in the limiting case of a vanishing tight-binding hopping parameter  $t$ . In this case, all electronic hopping is mediated by phonons. In all other chapters of this thesis we use  $t$  to normalize the other parameters and energies of the model. Unfortunately this procedure is incompatible in the case of vanishing  $t$  and another parameter is used to this purpose. Here,  $\tilde{g}$  is predestinated to be used as normalization factor. Of course, the normalization determines the energy scales. Nevertheless, it does not change the physics of the system and  $\tilde{g}$  could also be used to normalize the other cases. Because we also make contact between the  $t = 0$  limit and the simulations of the previous chapters where  $t$  is used for normalization and  $\tilde{g}/t = 1.5$  we try to avoid a change in measuring the energies. Therefore, we use the bare coupling  $g$ . Note, in Eq. (5.16) we got rid of the force constant  $k$  in the original model and introduced  $\omega_0$  and  $\tilde{g} = \sqrt{\frac{2}{k}} g$ . Now we use the bare coupling  $g$  for normalization such that

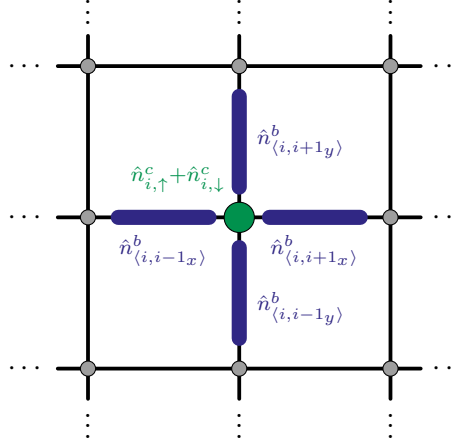


**Figure 7.1:** Sketch of the star operator  $\hat{Q}_i$ .

$\tilde{g}/g = 1.5$  is consistent with most of our simulations in the previous chapters and we are using de facto the same energy scale as before. Furthermore, this enables us to study different coupling strengths  $\tilde{g}$  in the zero hopping limit, what is in this normalization equivalent to different force constants  $k$ . To keep the notation simple, we set  $g$  to unity and drop it in the notation.

## 7.1 Unconstrained gauge theory

At  $t = 0$  the SSH model exhibits an additional  $\mathbb{Z}_2$  symmetry that is broken at any finite  $t$ . To illustrate the symmetry, we rewrite the SSH Hamiltonian using bosonic creation and annihilation operators  $\hat{a}_b$  and  $\hat{a}_b^\dagger$  for excitations of the harmonic oscillators to achieve

$$\hat{H}_{t=0} = \sum_{b,\sigma} \left[ \tilde{g} \sqrt{\omega_0} (\hat{a}_b^\dagger + \hat{a}_b) \hat{K}_{b,\sigma} + \omega_0 \hat{a}_b^\dagger \hat{a}_b \right]. \quad (7.1)$$

In this representation we are aware of the connection between the hopping of the electrons and the creation or annihilation of phonons. Using this mechanism we can define an Ising operator that is sensitive to the number of electrons on a lattice site as well as the parity of the phonon excitations on its associated bonds

$$\hat{Q}_i = (-1)^{\hat{n}_{i,\uparrow}^c + \hat{n}_{i,\downarrow}^c} (-1)^{\hat{n}_{\langle i, i+1_x \rangle}^b \hat{n}_{\langle i, i-1_x \rangle}^b \hat{n}_{\langle i, i+1_y \rangle}^b \hat{n}_{\langle i, i-1_y \rangle}^b}. \quad (7.2)$$

Due to its geometric shape on the lattice, this operator is also referred to as star operator, see Fig. 7.1.



The most important properties of  $\hat{Q}_i$  are

$$\hat{Q}_i^2 = 1, \quad [\hat{Q}_i, \hat{Q}_j] = 0 \quad \text{and} \quad [\hat{Q}_i, \hat{H}_{t=0}] = 0. \quad (7.3)$$

The last one follows from

$$[\hat{Q}_i, \hat{c}_{j,\sigma}^{(\dagger)}] = 2\hat{Q}_i \hat{c}_{j,\sigma}^{(\dagger)} \delta_{i,j} \quad \text{and} \quad [\hat{Q}_i, \hat{a}_{\langle m,n \rangle, \sigma}^{(\dagger)}] = 2\hat{Q}_i \hat{a}_{\langle m,n \rangle, \sigma}^{(\dagger)} (\delta_{i,m} + \delta_{i,n}). \quad (7.4)$$

Because  $\hat{Q}_i$  commutes with the Hamiltonian, it has to be a local conserved quantity. Unfortunately, the occupation number of phonons on the bonds is not accessible in an easy way by the HQMC method, so we are not able to measure it. The SSH model at  $t = 0$  can be understood as an unconstrained  $\mathbb{Z}_2$  gauge theory. In contrast to ordinary gauge theories an unconstrained gauge theory does not fulfill Gauss' law. Recently some models with unconstrained gauge theories attracted attention [60, 78, 79, 80].

In the anti-adiabatic limit,  $\omega_0 \rightarrow \infty$ , it becomes reasonable to use a hard-core constraint for the phonons. This means we expect to have not more than one phonon on a single bond. At this point we make contact with the model discussed in Ref. [60]. The authors discuss a model similar to the SSH model at  $t = 0$ . Instead of phonon mediated hopping they investigate how the electrons behave if Ising spins on the bonds determine the signs of the hopping. The authors of Ref. [60] use a hard core-boson description and derive a phase transition between a  $\mathbb{Z}_2$  Dirac deconfined phase ( $\mathbb{Z}_2$ D) and an AFM/CDW/SC phase.

Since the SSH model at  $t = 0$  has the same fundamental symmetries as the model in Ref. [60] we expect similar observations. Therefore we suppose the AFM/CDW/SC phase is still present in the zero hopping limit while the VBS phase could be replaced in favor of another, maybe a  $\mathbb{Z}_2$ D phase.

A further consequence of the  $\mathbb{Z}_2$  symmetry concerns the bond variables. The commutation rules of Eq. (7.4) transfer to  $\hat{X}_b$  and  $\hat{K}_b$ , so it holds

$$\hat{Q}_i \hat{X}_{\langle m,n \rangle} \hat{Q}_i = \begin{cases} -\hat{X}_{\langle m,n \rangle} & i \in \{m, n\} \\ \hat{X}_{\langle m,n \rangle} & \text{else} \end{cases}, \quad \hat{Q}_i \hat{K}_{\langle m,n \rangle} \hat{Q}_i = \begin{cases} -\hat{K}_{\langle m,n \rangle} & i \in \{m, n\} \\ \hat{K}_{\langle m,n \rangle} & \text{else} \end{cases}. \quad (7.5)$$

This also means  $\hat{X}_b$  and  $\hat{K}_b$ , like  $\hat{a}_b$ ,  $\hat{c}_i$  and  $\hat{c}_i^\dagger$ , carry a  $\mathbb{Z}_2$  charge. As shown in Fig. 6.11b, in the  $t = 1.0$  case we only observed finite and negative expectation values for the  $\hat{X}_b$  operators.

However, if  $t = 0$  the bond expectation value has to vanish because of

$$\langle \hat{X}_b \rangle = \langle \hat{X}_b \hat{Q}_i^2 \rangle = \langle \hat{Q}_i \hat{X}_b \hat{Q}_i \rangle = -\langle \hat{X}_b \hat{Q}_i^2 \rangle = -\langle \hat{X}_b \rangle = 0. \quad (7.6)$$

The equality in the first and last step are trivial. The equality relation in the second steps holds because  $\hat{Q}_i$  commutes with the Hamiltonian that means we can permute the  $\hat{Q}_i$  operator in the expectation value to the front of the product. Afterwards we make use of the anticommutator relations of Eq. (7.5) and conclude a vanishing expectation value. For the same reason also  $\langle \hat{K}_b \rangle$  vanishes.

As pointed out in Ref. [60], the  $\mathbb{Z}_2$  symmetry also applies to fermionic quantities and therefore causes localization of the electrons in real space because of

$$\langle \hat{c}_{i,\sigma}^\dagger(\tau) \hat{c}_{j,\sigma}(\tau') \rangle = \delta_{i,j} \langle \hat{c}_{i,\sigma}^\dagger(\tau) \hat{c}_{i,\sigma}(\tau') \rangle. \quad (7.7)$$

Additionally, the authors of Ref. [60] use electron operators connected by a string of bond operators, such as

$$\left\langle \hat{c}_{i_1,\sigma}^\dagger(\tau) \prod_{j=1}^{n-1} \hat{X}_{\langle i_j, i_{j+1} \rangle} \hat{c}_{i_n,\sigma}(\tau') \right\rangle, \quad (7.8)$$

to motivate the conductivity of quasi-particles in the  $\mathbb{Z}_2$ D phase. For further discussions of this phase we refer to Ref. [60].

In order to show the connection to the Ising model as well as to the models treated in Refs. [60, 81, 82] we consider the hard core boson restriction for a moment. In this case the Hilbert space of the bond operators is truncated to  $\{|0\rangle, |1\rangle\}$ . Therefore, Ising states can be defined by  $|\pm\rangle = \frac{1}{\sqrt{2}}(|0\rangle \pm |1\rangle)$ . In addition, we can define Ising spin operators as  $\hat{x}_b = 2\hat{b}_b^\dagger \hat{b}_b - 1$  and  $\hat{z}_b = \hat{b}_b + \hat{b}_b^\dagger$  such that  $\hat{z}_b|\pm\rangle = \pm|\pm\rangle$  and  $\hat{x}_b|\pm\rangle = |\mp\rangle$  [80]. Substituting the numerical parameters  $\tilde{g}$  and  $\omega_0$  in the Hamiltonian by  $g'$  and  $h'$  we derive the Hamiltonian as discussed in Ref. [60]

$$\hat{H}_{Z_2} = g' \sum_b \hat{z}_b \hat{K}_b + h' \sum_b \hat{x}_b. \quad (7.9)$$

Note, here the operator  $\hat{z}_b$  corresponds to the  $\hat{X}_b$  operator of the SSH model. As mentioned in Refs. [60, 80, 83], on the square lattice the plaquette product of  $\hat{z}_b$  operators  $\left(\prod_{b \in \square} \hat{z}_b\right)$  breaks no symmetry of the model and can be generated dynamically.

$$\hat{H}_{Z_2} = g' \sum_b \hat{z}_b \hat{K}_b + h' \sum_b \hat{x}_b + F \sum_{\square} \prod_{b \in \square} \hat{z}_b. \quad (7.10)$$

In the case of  $h' = 0$ , Refs. [60, 80, 83] discuss also a  $\pi$ -flux state ( $\prod_{b \in \square} \hat{z}_b = -1$ ) according to Lieb's theorem [71] that gives rise to Dirac fermions.

Although, Elitzur's theorem [84] does not permit a spontaneous breaking of the local  $\mathbb{Z}_2$  symmetry, the unconstrained gauge theory defined by Eq. (7.9) exhibits a (topological) phase transition [85, 86]. As discussed e.g. in Ref. [86], a duality transformation can be used to map Eq. (7.10) to an Ising model with the usual Ising transition.

Considering only the pure gauge fields, depending on the strength of  $h'$  the Ising gauge theory goes from a deconfined into a confined ground state. In detail, at small values of  $h'$  the system is expected to be in a deconfined  $\pi$ -flux state [60, 80]. At the phase transition, visons proliferate to the confined phase and fade out the  $\pi$ -flux [86]. More precisely, if a bond flips, it changes the fluxes of the two plaquettes it belongs to. These are the two vison excitations, one in each plaquette. In the deconfined phase the vison excitations are gapped [86] while they proliferate at the phase transition to the confined phase and therefore fade out the  $\pi$ -fluxes [80]. In the confined phase the visons can move through the lattice but stay connected by a string of bonds where the  $\hat{x}_b$  operator has acted on [86]. Although Elitzur's theorem [84] permit no local order parameter, Wilson loops can be used to measure the phases of the gauge theory [83]. A wilson loop is the product of a closed path of bond operators  $\hat{z}_b$  on the lattice. Therefore, the product of the hopping for a single plaquette can be seen as a special case of a wilson loop. Depending on the phase of the gauge theory, the Wilson loop exhibits an area-law or a perimeter-law behavior [83, 86]. For further discussions of the principles of  $\mathbb{Z}_2$  gauge theories we refer at this point to the literature, see e.g. Refs. [80, 60, 81, 82, 83, 85, 86, 87].

Although the assumption of hard core bosons in the SSH model can not be justified for small  $\omega_0$ , we make use of the symmetry arguments to discuss the possible ground states. For small values of  $\omega_0$  we assume to find a  $\pi$ -flux phase that indicates the deconfined  $\mathbb{Z}_2$  phase and causes Dirac fermions. As reported in Refs. [81, 82] the confinement-deconfinement phase transition can separate an AFM phase from a  $\mathbb{Z}_2$ D phase but can also occur between two AFM states. In this case the AFM state which contains the deconfined  $\mathbb{Z}_2$  gauge state is labeled by a star. Therefore, the AFM\* phase is separated from the AFM phase by a confinement-deconfinement phase transition.

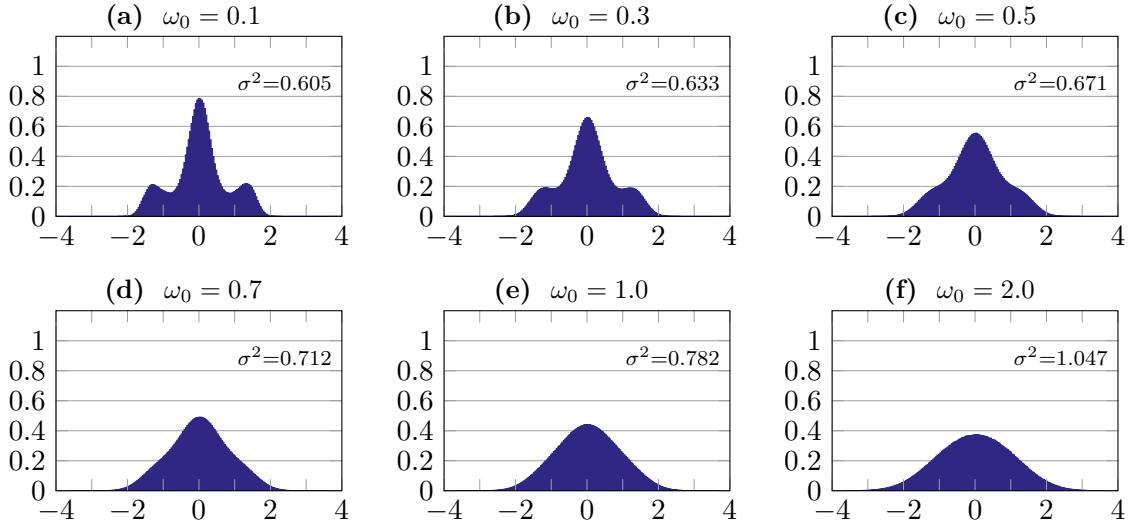


**Figure 7.2:** Histograms of  $\tilde{x}$  at  $t = 0$  on a  $8 \times 8$  lattice with  $\tilde{g} = 1.5$  and  $\beta = 16.0$ .

## 7.2 Vanishing hopping parameter

In the previous section we showed the vanishing of  $\langle \hat{K}_b \rangle$  and  $\langle \hat{X}_b \rangle$ . Because this is an important feature and is also relevant for the structure factors and susceptibilities we begin with a look at the HQMC histograms. Fig. 7.2 shows histograms of the bond variables  $\tilde{x}$ . In contrast to the histograms in Fig. 6.8 we observe only symmetric distributions that illustrate the vanishing of bond expectation values. Like in the previous chapter, the distribution reshapes to a single Gaussian and gets wider if the phonon frequency  $\omega_0$  becomes larger.

A further consequence of the local  $\mathbb{Z}_2$  symmetry concerns the structure factors and susceptibilities of the bond variables. The same argument that describes the vanishing of  $\langle \hat{X}_b \rangle$  and  $\langle \hat{K}_b \rangle$  can be also applied to the correlation function. Therefore, all non-local correlation functions of  $\hat{X}_b$  and  $\hat{K}_b$  have to vanish, too. This means, all structure factors and susceptibilities are flat and show no more information about long range ordered states, see (a) in Fig. 7.3. To investigate the bond observables in the  $t = 0$  limit, we have to consider gauge-invariant operators. Therefore, we can use structure factors of the squared operators  $\hat{X}_b^2$  and  $\hat{K}_b^2$ . Also a product of both operators,  $\hat{K}_b \hat{X}_b$ , is possible to define nontrivial structure factors and susceptibilities. Fig. 7.3b shows the structure factor of  $\hat{X}_b^2$ . Like in the  $t = 1$  case, all bond observables describe the same properties, whereby the bosonic bond observables  $\hat{X}_b$  do not depend on the stochastic inversion. Therefore, we choose the  $\hat{X}_b^2$  operator for illustrations in the following discussion.

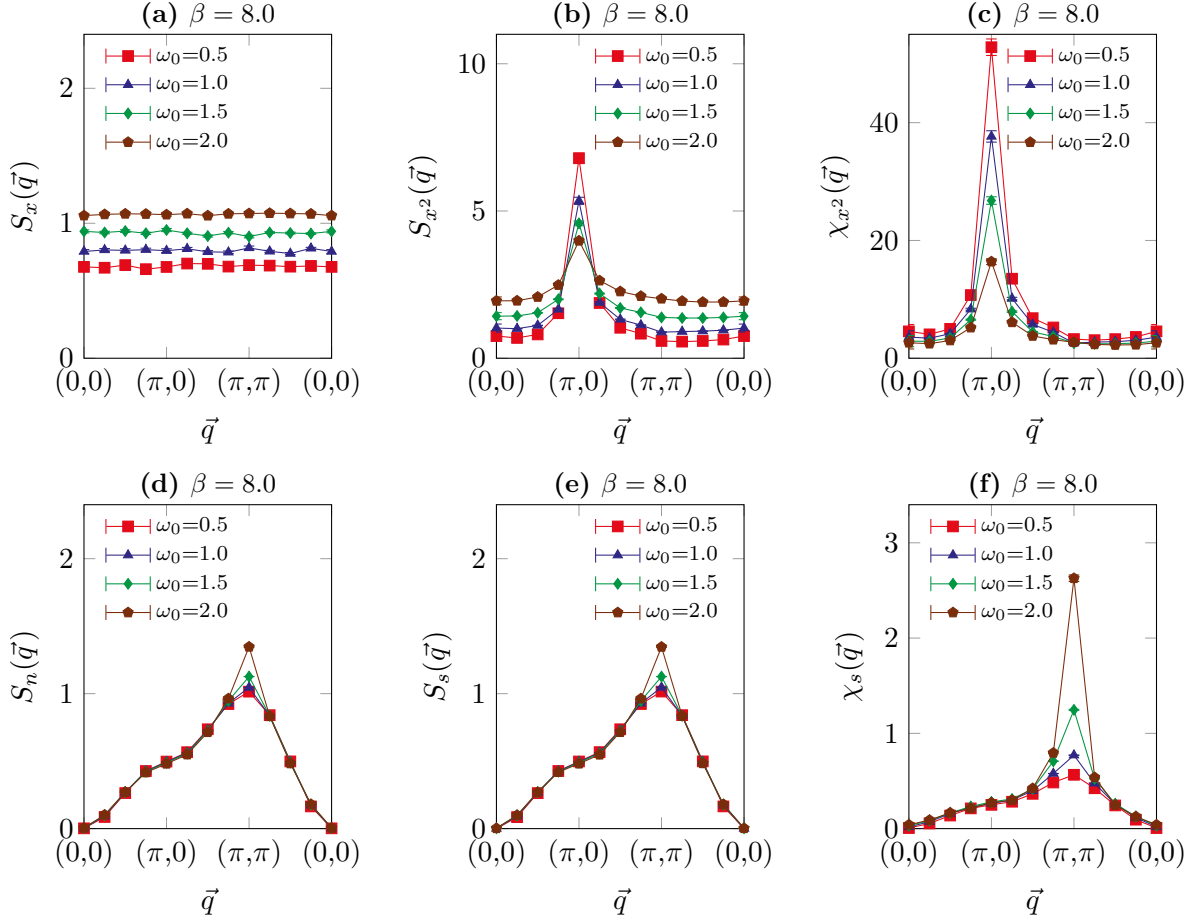


**Figure 7.3:** Structure factors and susceptibilities at  $t = 0$  on a  $8 \times 8$  lattice with  $\tilde{g} = 1.5$ ,  $\beta = 8.0$ .

Fig. 7.3c shows the susceptibility of the  $\hat{X}_b^2$  operator. In contrast to the peak at  $(\pi, \pi)$  we observed for  $t = 1$ , here we see a peak at  $(\pi, 0)$  in the structure factor as well as in the susceptibility. Besides a long ranged ordered  $(\pi, 0)$  VBS state the peak can also indicate a scenario of critical bond correlations as in Ref. [60]. Increasing  $\omega_0$  leads to a lowering of the peak in the bond susceptibility while a peak in the spin susceptibility at  $(\pi, \pi)$  emerges, see Fig. 7.3f. This peak in the spin susceptibility agrees with the expected AFM order [60]. Subplots (d) and (e) of Fig. 7.3 show the structure factors of the occupation number operator and the spin operator. Like at  $t = 1$  they are identical due to the  $O(4)$  symmetry.

As in the previous chapter, we can use the correlation ratio for further observations. To distinguish if the correlation ratio is evaluated at  $(\pi, \pi)$  or  $(\pi, 0)$ , we use the notation  $R'$  to label correlation ratios at  $(\pi, 0)$ . As in the previous section we assume  $z = 1$ . The correlation ratio of the structure factor and susceptibility of the bond variables in subplots (a) and (b) of Fig. 7.4 may support

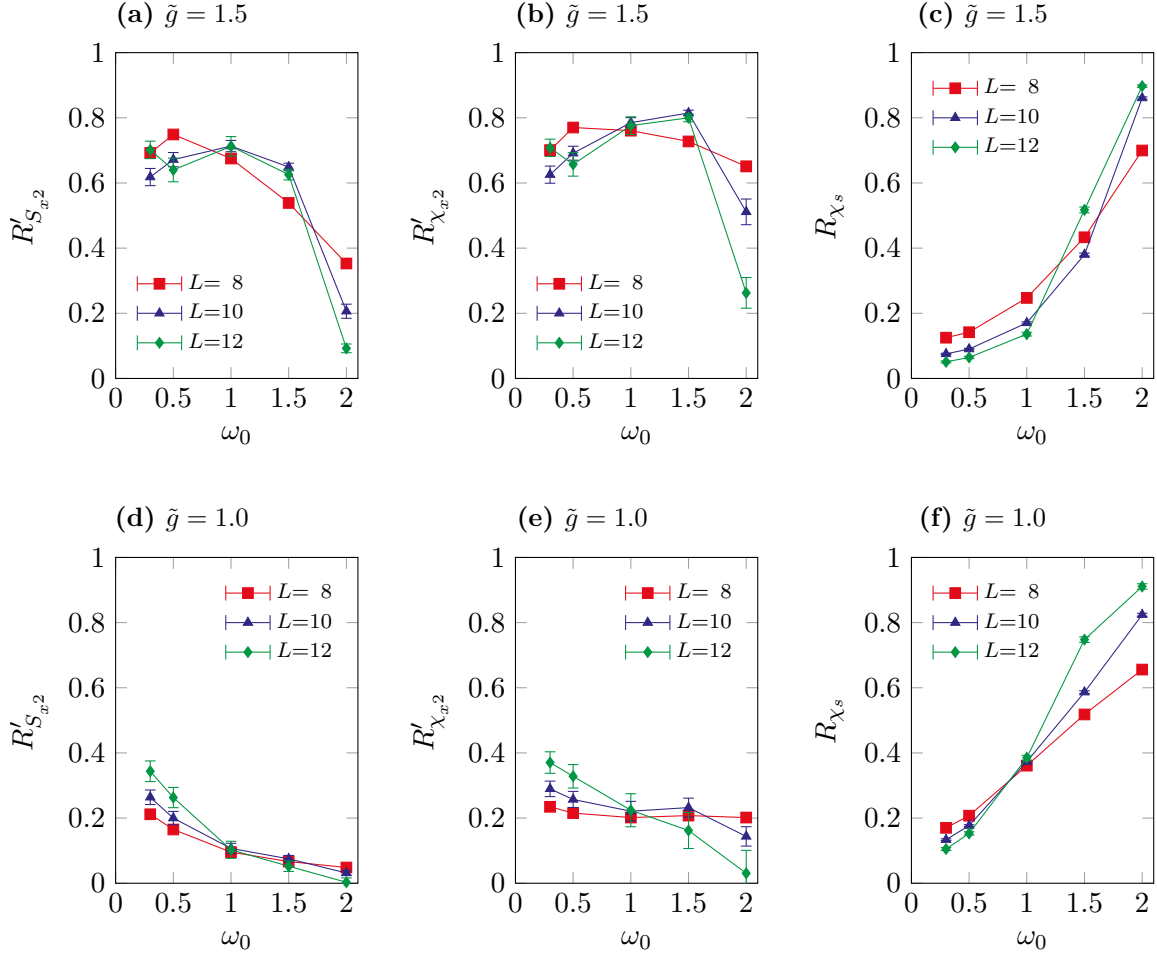


**Figure 7.4:** Correlation ratios on  $L \times L$  lattices using  $\beta = L$  for several values of  $\tilde{g}$ .

the suspicion that the bonds do not order. The slightly different behavior of the  $8 \times 8$  system could be a finite size effect. Strong fluctuations of the structure factors and susceptibilities at  $(\pi, 0)$  complicate a proper analysis. The data in (a) and (b) exhibit a maximum at intermediate values of  $\omega_0$  which seems not to fit to a VBS ordered state extending to  $\omega_0 = 0$ . However it could indicate an intermediate VBS phase, surrounded by a  $Z_2$ D phase at lower frequencies and an AFM phase at higher frequencies. Such a scenario was observed in Ref. [60] in the case of three fermionic spin flavors. In contrast, the correlation ratio of the spin susceptibility in (c) supports clearly long range AFM order at sufficient large  $\omega_0$ .

In order to investigate the ground state physics of the SSH model in the  $t = 0$  limit we change  $\tilde{g}$ . The qualitative behavior of the structure factors and susceptibilities is unchanged, but we achieve better data for the correlation ratios. Subplots (d)-(f) show the correlation ratios at

$\tilde{g} = 1.0$ . Fortunately, the finite size effects seem to be suppressed. The correlation ratios of the spin susceptibilities exhibit a clear crossing point near  $\omega_0 = 1$ , see Fig. 7.4f. And also the correlation ratios of the bond structure factor show a clear crossing at  $\omega_0 = 1.0$ , Fig. 7.4d. Taking the error bars into account, also the correlation ratios of the bond susceptibilities in Fig. 7.4e supports this observation. Furthermore, the clear indication for a long range  $(\pi, 0)$  VBS order suggests the possibility of a DQCP phase transition. Certainly, a further  $Z_2$ D phase at smaller frequencies as we simulated seems unlikely but can not be excluded.

Summarizing the observations from the correlation ratios, the presence of an AFM phase at large phonon frequencies is shown. In the regime of small phonon energies we have indications for a  $(\pi, 0)$  ordered VBS which maybe shrinks in favor of a  $Z_2$ D phase if  $\tilde{g}$  is increased. Although the authors of Ref. [60] do not notice a VBS phase in their simulation of two fermionic spin flavors this is no contradiction to our observations. Ref. [60] assumes hard-core bosons modulating the hopping of the electrons. Additionally, the phase transition in Ref. [60] is controlled by the strength of a transverse field. In case of the SSH model the energy of the phonons controls the phases and the number of phononic excitations is arbitrary. Of course, concerning very high frequencies the excitation of many phonons becomes unlikely but especially at small values of  $\omega_0$  the hard-core boson assumption can not be applied to the SSH model. Therefore a condensation of the phonons in favor of a  $(\pi, 0)$  ordered VBS state does not conflict with the observations in Ref. [60].

It remains to discuss the origins of the  $(\pi, 0)$  instabilities as well as the confinement-deconfinement phase transition of the unconstrained  $Z_2$  gauge theory. In the previous chapter, the band structure of the tight-binding model on a square lattice promoted  $(\pi, \pi)$  ordering. However, if the tight-binding hopping vanishes, this argument drops.

As mentioned in Ref. [60] and according to Ref. [71], in case of Ising variables controlling the sign of the local hopping parameter on the bonds of a square lattice and without other interactions the ground state has to show  $\pi$ -fluxes. Furthermore, a pure  $\pi$ -flux phase exhibits two Dirac points in the first Brillouin zone, with a momentum transfer vector of  $(\pi, 0)$  that may cause the peaks in the bond variables. Note, bond ordering like in the Kekule phase is a mass term for the Dirac electrons and equivalent to the VBS phases [88, 89]. In our case the bond observables are continuous and should be able to generate  $\pi$ -fluxes dynamically as mentioned in the previous section. Therefore, it seems reasonable to interpret a  $\pi$ -flux state as an indication, or maybe even a requirement, for a  $Z_2$ D or columnar VBS order. As in the previous chapter we use  $f_\pi$ , as defined by Eq. (6.13), to measure a potential  $\pi$ -flux. In addition, we also introduce the average sign of

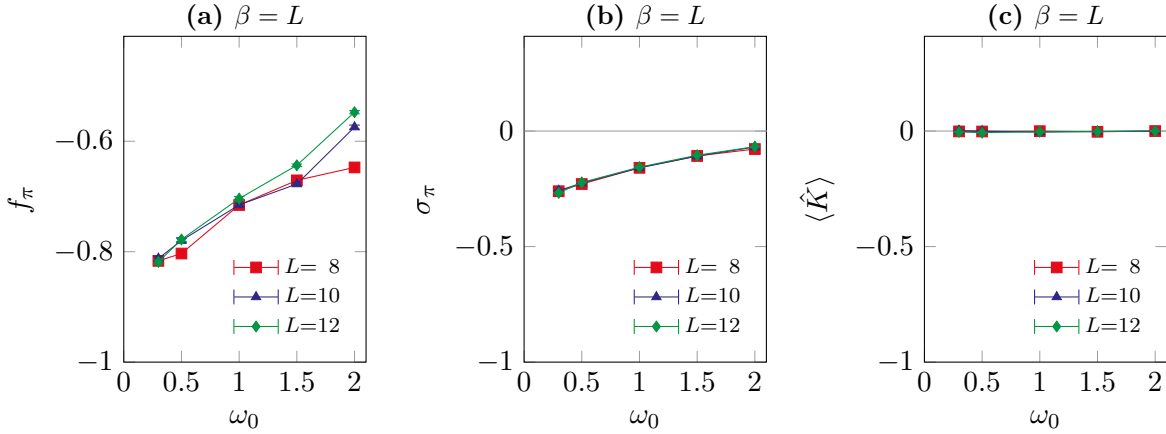


**Figure 7.5:** Average flux per plaquette on  $L \times L$  lattices with  $\tilde{g} = 1.5$  and  $\beta = L$ .

the product of effective hopping per plaquette  $\square$  by

$$\sigma_\pi(\tilde{x}) = \frac{1}{L_x L_y} \sum_{\square} \text{sgn} \left( \prod_{b \in \square} \tilde{g} \tilde{x}_b \right). \quad (7.11)$$

Fig. 7.5 shows how  $f_\pi$  and  $\sigma_\pi$  behave dependent on the phonon frequency. As we supposed, the average of the product of the effective hopping parameters per plaquette is negative, Fig. 7.5a. This agrees to the expectation of a  $\pi$ -flux state. The average sign  $\sigma_\pi$  is also negative, see Fig. 7.5b. However it shows us that not all plaquettes exhibit a  $\pi$ -flux what is different from the scenario in the Lieb theorem [71] but compatible with our assumption of a dynamically generated flux. This behavior agrees with the expectation of a deconfined  $\mathbb{Z}_2$  phase at small  $\omega_0$  as discussed at the end of the previous section.

As discussed in Sec. 7.1, a deconfined AFM phase is named AFM\* and is separated by a phase transition from the confined AFM state [81, 82]. Furthermore, because also the possible cVBS phase is according to the  $\mathbb{Z}_2$  deconfined regime we have call it cVBS\* henceforth. While the condensation of the particle-hole excitations is responsible for the AFM phase, the proliferation of visons only rely on the confinement-deconfinement phase transition and is independent from the matter fields. However, we have no indications for the confinement-deconfinement phase transition. The increasing of  $f_\pi$  in Fig. 7.5a shows no kink, jump or any other indication of a transition. Nevertheless, the confined  $\mathbb{Z}_2$  gauge phase is expected for large values of  $\omega_0$  and is most likely not covered by our sets of parameters. Concluding the discussion of the effective hopping, Fig. 7.5c shows the expected vanishing of the expectation value of the bare hopping operator.



At the end of this section we briefly summarize our observations. Actually, the HQMC method is able to simulate the SSH model even without tight-binding hopping. We were able to observe the expected features of an unconstrained gauge theory like  $\langle \hat{X} \rangle = 0$  and  $\langle \hat{K} \rangle = 0$ . In addition, we can detect the AFM\* phase and the signals of the bond structure factor at  $(\pi, 0)$ . Considering also our  $\pi$ -flux observations our results may indicate a cVBS\*, respectively a  $\mathbb{Z}_2$ D phase at small  $\omega_0$ . Although, more simulations by the HQMC method are required to improve the understanding of the model at  $t = 0$  and the influence of  $\tilde{g}$  we successfully used the method to gain some first promising insights.

### 7.3 Intermediate hopping regime

After discussing the physical properties in the case of vanishing  $t$  in the previous section, we now aim to extend the discussion to the regime between  $t = 0$  and  $t = 1$ . Here we present some data scans by the HQMC method to get an idea what happens in the intermediate regime. Because the unconstrained  $\mathbb{Z}_2$  gauge theory is broken at any finite value of  $t$  also the concepts of confined and deconfined phases are meaningless in the this case.

To beginning with, we take a look at the structure factors and susceptibilities. We consider two data scans, one inside the AFM ordered phase at  $\omega_0 = 2.0$  and another at  $\omega_0 = 0.3$  containing the VBS state at  $t = 1$ . Fig. 7.6 shows the bond structure factors and susceptibilities of the bond operator as well as the spin susceptibilities at  $\tilde{g} = 1.5$ . Starting in the AFM regime, increasing  $t$  reduces the maximum in  $S_{x^2}$  and  $\chi_{x^2}$  at  $(\pi, 0)$  until it vanishes, see (a) and (b). Subplot (c) shows, also the peak in  $\chi_s$  is reduced by increasing  $t$ . As we motivated the  $t = 0$  limit, lowering  $t$  can be interpreted like increasing  $\tilde{g}$ . Therefore the reduction of the peak in (c) is reasonable.

Considering the structure factor  $S_{x^2}$  in Fig. 7.6d and  $S_{x^2}$  in Fig. 7.6e we see how the peak at  $(\pi, 0)$  vanishes and the  $(\pi, \pi)$  VBS order continuously rises. Meanwhile, the structure factor of the spin remains unchanged, see Fig. 7.6f. Note the scale in (d) and (e) due to the peaks at  $(\pi, 0)$ , the  $(\pi, \pi)$  peaks are stronger as it seems. The strong fluctuations with the according large error bars we observe in our data scan for the bond observables at  $(\pi, 0)$  prevents a more detailed discussion by correlation ratios.

In the next step we take a look at  $f_\pi$  and  $\sigma_\pi$ . As we know from Fig. 6.11, no  $\pi$ -flux is observed at  $t = 1$ . In contrast, at  $t = 0$  all simulations show a  $\pi$ -flux behavior. The subplots (a) and (d) of Fig. 7.7 show  $f_\pi$  as function of  $t$  for large and small phonon frequencies.  $f_\pi$  behaves like a continuous function. We also observe no deviations between simulations of different lattice sizes

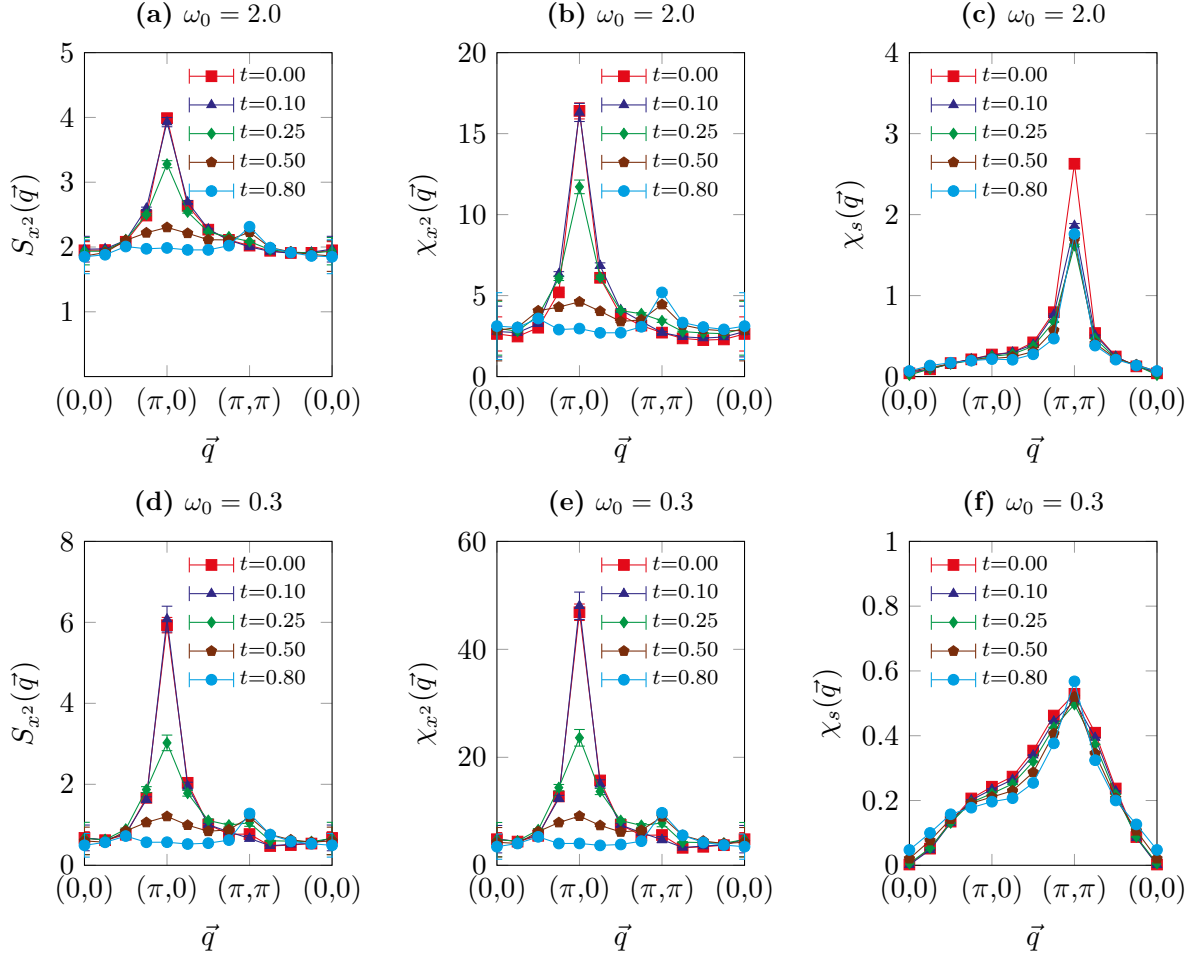


**Figure 7.6:** Structure factors dependent and susceptibilities on a  $8 \times 8$  lattice, using  $\tilde{g} = 1.5$  and  $\beta = 8.0$ .

and temperatures. Comparing  $f_\pi$  in Fig. 7.7 with the bond structure factors in Fig. 7.6 we can see how the  $f_\pi$  becomes positive simultaneously to the vanishing of the peak at  $(\pi, 0)$ . The same holds for  $\sigma_\pi$  in subplots (b) and (e). Interestingly, a close look to the data reveals  $f_\pi$  take its minimum at a finite value of  $t$ . In case of  $\omega_0 = 0.3$  the minimum is at approximately  $t = 0.05$ . In case of  $\omega_0 = 2.0$  the minimum occurs somewhere between  $t = 0.1$  and  $t = 0.2$ .

Especially in case of small  $\omega_0$  some kind of phase transition has to take place. The staggered VBS order of  $t = 1$  is not observed at  $t = 0$ . In general, phase transitions are described and classified by the behavior of the free energy and the according derivatives. If  $t$  is varied and  $\omega_0$  is fixed, the first derivative of the free energy becomes equivalent to  $-\langle \hat{K} \rangle$ . Considering the subplots (c) and (f) of Fig. 7.7 we observe how  $\langle \hat{K} \rangle$  behaves. Again we obtain the same behavior

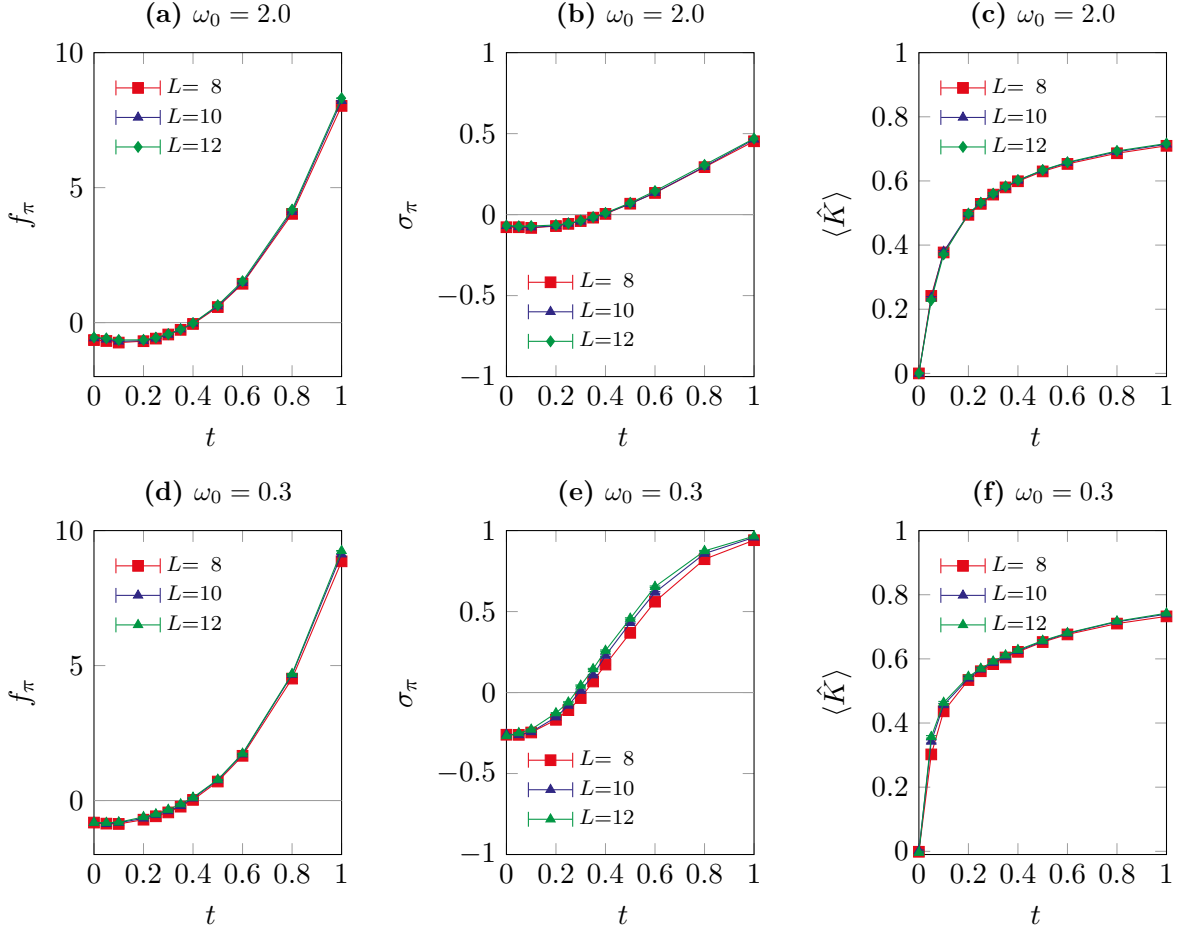


**Figure 7.7:**  $\pi$ -flux and bond variables with  $\tilde{g} = 1.5$  and  $\beta = L$ .

for different system sizes. In general, we observe no indicators for discontinuities. Consequently, no phase transitions can be determined. Instead, the vanishing of the dynamically generated  $\pi$ -fluxes seems to be a crossover. Because the unconstrained  $\mathbb{Z}_2$  gauge symmetry is broken at finite  $t$  a crossover between AFM\* and AFM seems to be natural. However a crossover does not explain the vanishing of the sVBS phase at small  $\omega_0$  if  $t$  is decreased. Otherwise, the derivatives only exclude strong first order transitions. For a more detailed investigation, the correlation ratios or other types of scaling analysis are required to determine phase transitions.

For completeness we also take a look at the histograms of the bond variables. Starting from  $t = 0$  in the AFM phase, Fig. 7.8 illustrates the shift of the midpoint of the distribution from 0 to negative values. At the same time, the variance of the Gaussian lowers little bit. More is happening for small frequencies. Fig. 7.9 shows how the distribution of the  $\tilde{x}$  variables changes

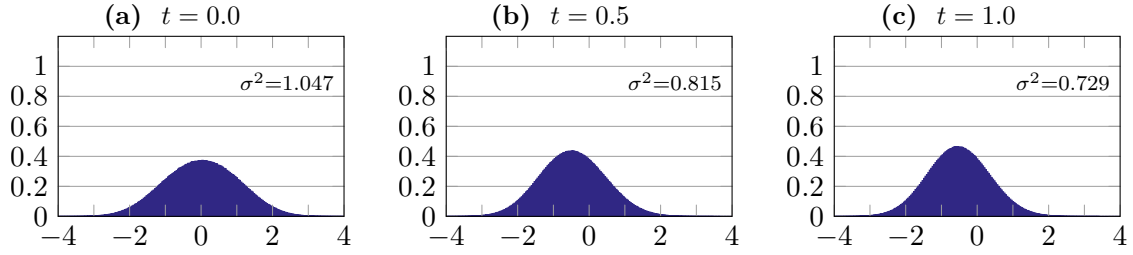


**Figure 7.8:** Histograms of  $\tilde{x}$  at  $t = 0$  on a  $8 \times 8$  lattice with  $\tilde{g} = 1.5$  and  $\beta = 8.0$ .

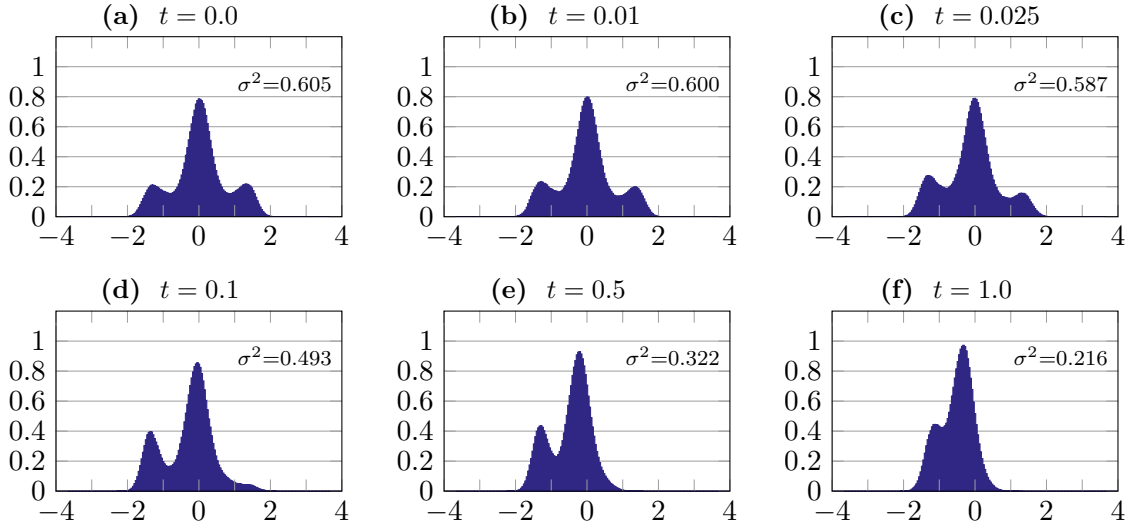


**Figure 7.9:** Histograms of  $\tilde{x}$  at  $t = 0$  on a  $8 \times 8$  lattice with  $\tilde{g} = 1.5$  and  $\omega_0 = 0.1$  and  $\beta = 16.0$ .

step wise. Here we use  $\beta = 16.0$  to emphasize the shape of the derivation. As soon as  $t$  becomes finite, the right peak in the distribution lowers while the left peak increases simultaneously and the maximum in the middle seems to be unchanged. In (d) the bimodal Gaussian we know from Fig. 6.8 remains. A further increasing of  $t$  moves the distribution to negative numbers and brings the two peaks closer together. The vanishing of the third peak in the distribution of  $\tilde{x}$  happens already for small values of  $t$  and seems to be unrelated to the vanishing of the  $\pi$ -flux.

Summing up, we observed continuous changes in all quantities for varying  $t$ . The peaks of  $S_{x^2}$  and  $\chi_{x^2}$  at  $(\pi, 0)$  seem to be connected to the  $\pi$ -flux state. Interestingly, we observed a continuous crossover in the  $\pi$ -flux function  $f_\pi$  and  $\sigma_\pi$  and no discontinuities in the energy derivation according to  $\langle \hat{K} \rangle$ . More detailed simulations in the future could help to draw a precise picture of what is happening in this regime.

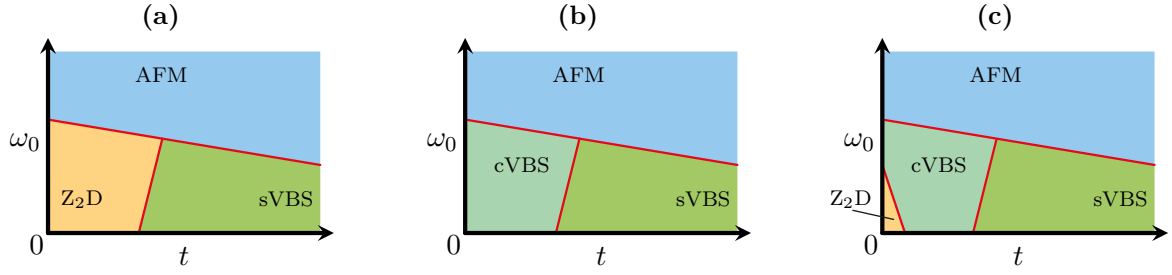


**Figure 7.10:** Sketches how the phase diagram of the two-dimensional SSH model could look.

## 7.4 Possible phase diagram

At the end of this chapter, we summarize all observations of the previous sections. Varying the tight-binding hopping parameter  $t$  in the half-filled SSH model seems to be a promising way to learn more about several mechanisms. The unconstrained gauge theory of Ref. [60] as well as the dynamical generation of  $\pi$ -fluxes are some of the interesting aspects of the model.

Although further simulations are necessary to draw a precise picture of the ground state physics of the two-dimensional SSH model, we were already able to investigate some of its fundamental properties. The presence of an AFM phase at large phonon frequencies seems to be sure. The  $(\pi, 0)$  peaks in the structure factors and susceptibilities of the bond operators together with the  $\pi$ -fluxes could explain a columnar VBS phase, respectively a cVBS\* or  $Z_2$ D phase, at small  $\omega_0$  and zero hopping, similar to Ref. [60]. The evolution from  $t = 0$  to  $t = 1$  seems continuous. However, a phase transition between the cVBS, or  $Z_2$ D, phase at small  $t$  and the staggered VBS phase at  $t = 1$  has to take place somewhere. Therefore, a clear interpretation is missing at the moment and further simulations and investigations are required.

Finally, we can make some educated guesses how the phase diagram of the two-dimensional SSH model could look in dependency on  $t$  and  $\omega_0$ . Because the phase diagram is also depending on  $\tilde{g}$ , various of the following scenarios could apply to different values of  $\tilde{g}$ .

Due to the broken  $Z_2$  symmetry of the unconstrained gauge theory at finite  $t$ , we always assume a crossover between the AFM\* phase with its according  $\pi$ -flux state as observed at  $t = 0$  and the AFM phase at  $t = 1$ . In the  $t = 0$  limit of the first scenario, we furthermore assume the existence of an AFM\* phase and a  $Z_2$ D phase at  $t = 0$ . Theoretically, an emergent symmetry could protect the  $Z_2$ D phase for small hopping perturbations such that the phase is still present at small finite  $t$ . Fig. 7.10a shows a sketch of the according phase diagram. This scenario could apply to our observations at  $\tilde{g} = 1.5$ .

The next scenario in Fig. 7.10b is inspired by our observations for  $\tilde{g} = 1.0$  we assume a cVBS\* phase at  $t = 0$  and a cVBS phase for small finite values of  $t$  at small  $\omega_0$ . Interestingly, in this scenario a DQCP transition between cVBS\* and AFM\* and also between cVBS and AFM seems possible.

In the last scenario, illustrated by Fig. 7.10c, we extend the second one by a small  $Z_2D$  regime. This possibility could apply to the  $\tilde{g} = 1.5$  data as well.

In this chapter we provided some first insights to the phase diagram of the SSH model in two dimensions. Of course, even more scenarios are conceivable. A detailed and conclusive determination of the phase diagram of the two-dimensional SSH model remains an interesting topic for ongoing research.

# 8

## Chapter 8

---

# Conclusion

In order to conclude this thesis, we summarize our results, report the experience we made using the hybrid quantum Monte Carlo method and provide an outlook on followup work.

The goal of this thesis was to investigate the applicability and performance of the HQMC method and to apply it to a electron-phonon model, namely the SSH model.

In the first part of this thesis we studied the HQMC method to investigate its applicability and tested its performance. Starting with the Hubbard model, we pointed out ergodicity issues and proposed a way to solve the problem by a complexified formulation of the HQMC method in Chapter 4. The intended sub-quadratic scaling with system size and inverse temperature could not be observed for the Hubbard model. In a comparison with the BSS-QMC method, the HQMC method is less efficient, i.e. it exhibits much larger statistical errors for a given amount of computing time. Subsequently, we reformulated the HQMC method for simulations of the two-dimensional SSH model in Chapter 5 and achieved a much better scaling behavior. An important observation we made concerns the simulation parameters of the HQMC method. Besides the considered model and the model parameters, the parameters of the HQMC simulation itself have a large influence on the performance of the method. Parameters like time-step size, number of stochastic inversions during each measurement, targeted accuracy of the CG method, number and length of Leapfrog runs between measurements, the chosen variance for the directly sampled momentum fields etc. have an important impact to the performance of the method. If the parameters are not chosen carefully the simulation slows down, generates highly correlated samples and/or increases the time to warm up the simulation. Unfortunately, it is very challenging to predict the optimal parameters but data observations and experiences guide to well balanced sets of parameters. Even though the HQMC method requires more fine tuning than other methods,

applied to the SSH model we were able to perform systematical Monte Carlo simulations in two dimensions for the first time.

In the second part of this thesis we applied the HQMC method to the SSH model in order to investigate its physical properties. The SSH model is of special interest because of its topological aspects in one dimension. In Chapter 6, we used an extended mean field approach to investigate the adiabatic limit of the SSH model in two dimensions. The staggered VBS pattern we observed was confirmed by our HQMC simulations. Although, we were not able to determine the precise nature of the phase transition, our HQMC simulations reveal important results. We illustrated the staggered VBS ground state for small phonon energies as well as the  $O(4)$  symmetric AFM/CDW/SC state on finite lattices for large phonon energies. Interestingly, the phase transition between the two ordered states seems to be more complicated than expected and also no field-theoretical description is available.

Finally, we gave an outlook to the entire phase diagram of the SSH model in two dimensions in Chapter 7. We varied the hopping parameter  $t$  in order to simulate different strengths of the electron-phonon coupling. At  $t = 0$  we made contact with an unconstrained  $\mathbb{Z}_2$  gauge theory. The results of our simulations for a vanishing hopping parameter point to a  $\pi$ -flux state and indicate a possible  $Z_2$ D phase as well as a columnar VBS state at small phonon frequencies. At large frequencies we again observed AFM/CDW/SC order. Furthermore, we provided some insights to the intermediate hopping regime and discussed possible scenarios for the phase diagram. Remarkably, the phase diagram seems to be very rich and includes a lot of interesting phase transitions. While we excluded a DQCP between the staggered VBS and the AFM phase, for small hopping, or equivalent for strong electron-phonon coupling, a DQCP transition is expected to occur between the columnar VBS and the AFM phase. Usually, exotic phase transitions like this are simulated using designer Hamiltonians. In contrast, the SSH model is a well established and physical motivated model.

It remains to take an outlook on how the insights of this work could be used in the future. Especially models that are not feasible for the BSS-QMC method due to long autocorrelation times are candidates to be simulated with the HQMC method. Further method developments like approaches to combine the global updating scheme of the HQMC method with the robustness and predictability of the BSS-QMC method are conceivable. In view of the SSH model several further investigations are possible. Especially the  $O(4)$  symmetry and the additional unconstrained  $\mathbb{Z}_2$  gauge theory at  $t = 0$  make the model very interesting. This work can be used as a starting point for further numerical and analytical investigations of the phonon frequency-dependent phase transition between a staggered VBS and an AFM phase as well as for the phase transitions in



---

---

the zero hopping limit and the intermediate regime. Breaking the  $O(4)$  symmetry by introducing a finite chemical potential or next nearest neighbor hopping offers even more opportunities for further investigations.



**Part III**

**Appendix**



# A

## Appendix A

---

# Trotter Decomposition

In this chapter we shine a light on the Trotter decomposition, also known as Suzuki-Trotter approximation. The systematical error of hybrid quantum Monte Carlo as well as of the BSS-QMC traces back to the Trotter decomposition as used in Eq. (3.4).

Historically, the Trotter product formula [90] for linear operators  $\hat{A}$  and  $\hat{B}$

$$\lim_{n \rightarrow \infty} \left( e^{-t\hat{A}/n} e^{-t\hat{B}/n} \right)^n = e^{-t(\hat{A}+\hat{B})}, \quad (\text{A.1})$$

initiated the development of splitting methods which is still a field of ongoing research [30]. Later on Suzuki extended the work of Trotter and started to use it in condensed matter physics [91, 92, 93]. In general, the Trotter decomposition can be seen as an approximation of the well known Baker-Campbell-Hausdorff formula

$$e^{\hat{A}+\hat{B}} = e^{\hat{A}} e^{\hat{B}} e^{-\frac{1}{2}[\hat{A}, \hat{B}]} \quad (\text{A.2})$$

which holds for  $[\hat{A}, [\hat{A}, \hat{B}]] = [\hat{B}, [\hat{A}, \hat{B}]] = 0$ , with the commutator  $[\hat{A}, \hat{B}] = \hat{A}\hat{B} - \hat{B}\hat{A}$ . As used in Eq. (3.4), the Trotter decomposition neglects all commutator relations between the operators and generates an error proportional to  $\Delta\tau^2$  in its leading order,

$$e^{-\Delta\tau(\hat{H}_K + \hat{H}_U)} = e^{-\Delta\tau\hat{H}_K} e^{-\Delta\tau\hat{H}_U} + \mathcal{O}(\Delta\tau^2). \quad (\text{A.3})$$

For HQMC and BSS-QMC this systematical error needs to be controlled by choosing a sufficiently small  $\Delta\tau$ .

Besides the discussed usage of a Trotter decomposition to rearrange the partition function it is also present in other parts of the algorithm.

In detail, the leapfrog method that performs the time evolutions of the artificial Hamilton function, as discussed in Sec. 3.2 and 3.3, is equivalent to a symmetric Trotter expansion [30]. The simultaneous time evolution of momentum and auxiliary fields are separated from each other and executed in alternating fashion.

Another situation where the Trotter decomposition can be used beneficially is during the implementation of the HQMC or BSS-QMC method. In case of the HQMC, most of the computing time is spent by performing matrix vector multiplications which are needed for example during the conjugate gradient method. The block matrices  $B_l$  of Eq. (3.8) have to be multiplied by parts of the pseudo fermion vector  $\phi$ . For both, Hubbard and SSH models, the  $B_l$  matrices are some kind of exponentiated hopping matrices. Because the hopping matrices are not diagonal, the resulting  $B_l$  matrices are dense. Dealing with dense matrices is unfavorable for several reasons, like memory requirements and computation time for calculating the exponential matrix. Additionally, due to its  $\mathcal{O}(N^2)$  scaling, the numerical effort of a matrix vector multiplication using dense matrices leads to disproportionately long runtimes for the whole method.

Computing the exponential of a matrix is a common problem, a discussion of modern strategies can be found in Ref. [94]. To speed up the methods, several ways of using sparse matrices are possible. Using a simple Taylor expansion is one option. It preserves properties like hermiticity and it can be combined with a wide selection of software libraries for sparse matrices. The respective truncation error has to be controlled by  $\Delta\tau$ . Taylor expansions to higher orders in  $\Delta\tau$  ensure that this error stays smaller than the systematic error introduced by the Trotter decomposition in Eq. (3.4).

Another option to keep down the computational effort is the usage of a checkerboard decomposition on a bipartite lattice which is just another application of the Trotter decomposition [33]. Instead of approximating the exponential function, the checkerboard method rearranges the hopping matrix in a sum of a few matrices that are easy to exponentiate individually. In practice, the hopping matrix describes electron hopping on the lattice. So the coordination number of the lattice defines the minimal number of required terms. If next nearest neighbor hopping on the square lattice is simulated, the number of matrices has to be increased by the number of next nearest neighbors. For arbitrary lattices, Vizing's theorem for simple undirected graphs estimates the number of required families to be either the coordination number or the coordination number increased by one.

---

In the following we will discuss the details of the checkerboard decomposition and compare it with the results of a truncated Taylor expansion. For simplicity we restrict our discussion to spinless nearest neighbor hopping on a square lattice

$$\hat{H} = -t \sum_{\langle i,j \rangle} (\hat{c}_i^\dagger \hat{c}_j + \hat{c}_j^\dagger \hat{c}_i). \quad (\text{A.4})$$

All findings and arguments are transferable to other lattices and models.

Every lattice site is connected to the four surrounding sites. Due to the associativity of operator addition various arrangements are possible. We rewrite the exponential expression and approximate

$$e^{-\Delta\tau \hat{H}} = e^{\hat{X}_1 + \hat{X}_2 + \hat{Y}_1 + \hat{Y}_2} \simeq e^{\hat{X}_1} e^{\hat{X}_2} e^{\hat{Y}_1} e^{\hat{Y}_2}, \quad (\text{A.5})$$

where  $\hat{X}_1$  and  $\hat{X}_2$  contain hopping in  $x$ -direction, while the hopping in  $y$ -direction is represented by  $\hat{Y}_1$  and  $\hat{Y}_2$ . Terms consisting of exponentiated commutators of  $\hat{X}_i$  and  $\hat{Y}_j$  are neglected. In principle we are free to group these families as we want, up to a single restriction. All hopping operators belonging to the same family are defined to commute pairwise.

If so, we can separate the matrix exponentiation of each family into a series of independent  $2 \times 2$  matrix operations. For illustration, if we consider one of those families, all bonds in this family have to connect different sites of the lattice, otherwise they do not commute. In a matrix representation, the independent bonds are equivalent to a reducible matrix structure. Consequently, we can perform permutations to simplify those matrices into a set of decoupled  $2 \times 2$  matrices. After exponentiation and permuting them back, we achieve a sparse matrix representation of each exponentiated family

$$\begin{pmatrix} \ddots & & & & \\ & 0 & \cdots & -\Delta\tau t & \\ & \vdots & \ddots & \vdots & \\ & -\Delta\tau t & \cdots & 0 & \\ & & & & \ddots \end{pmatrix} \xrightarrow{\text{exp}} \begin{pmatrix} \ddots & & & & \\ & \cosh(\Delta\tau t) & \cdots & -\sinh(\Delta\tau t) & \\ & \vdots & \ddots & \vdots & \\ & -\sinh(\Delta\tau t) & \cdots & \cosh(\Delta\tau t) & \\ & & & & \ddots \end{pmatrix}. \quad (\text{A.6})$$

The giant computational effort that is necessary to exponentiate the Hopping matrix breaks down to a bookkeeping problem and additionally saves a lot of memory. For the Hubbard model, it is sufficient to compute the exponentiated hopping matrix once at the beginning. In case of the SSH model, the bond displacements determine the effective hopping between two sites. As a consequence the representation of the exponentiated hopping matrix has to be updated with

each change in the auxiliary fields. Without a sparse matrix approximation like the checkerboard decomposition, these simulations would be limited to very small system sizes.

As mentioned above, the choice of the families is not unique. We will discuss two different patterns on the square lattice and distinguish between columnar and staggered patterns in both  $x$ - and  $y$ -direction. The left hand side of Fig. A.1 shows what columnar patterns of bonds look like. Together, the four columnar patterns contain all bonds of the lattice. The same holds if staggered patterns, as illustrated on the right hand side of Fig. A.1, are used. To apply the checkerboard decomposition we may choose the columnar or the staggered patterns. Also a mixture, like columnar patterns in  $x$ -direction and staggered patterns in  $y$ -direction, can be implemented. Although all of those combinations are possible, we are going to show that some of them are more favorable than others.

To illustrate the importance of a suitable choice we will apply each checkerboard decomposition to the tight-binding model and calculate the local Green's function. As mentioned before, the Green's function is one of the most important physical observables and due to Wick's theorem it plays an essential role for all measurements in the HQMC and BSS-QMC method. According to that, it is important not to compromise the Green's function.

We do the comparison in the following way. The Green's function is given by the inverse of the matrix  $M$  defined in Eq. (3.8)

$$\begin{aligned}
 G(r = (i - j), \tau = (\tau' - \tau'')) &= [M^{-1}]_{(i, \tau'), (j, \tau'')} \\
 &= \left[ \begin{pmatrix} \mathbb{1} & 0 & 0 & \cdots & 0 & B_{N_\tau} \\ -B_1 & \mathbb{1} & 0 & \cdots & 0 & 0 \\ 0 & -B_2 & \mathbb{1} & \cdots & 0 & 0 \\ \vdots & \vdots & \vdots & \ddots & \vdots & \vdots \\ 0 & 0 & 0 & \cdots & \mathbb{1} & 0 \\ 0 & 0 & 0 & \cdots & -B_{N_\tau-1} & \mathbb{1} \end{pmatrix}^{-1} \right]_{(i, \tau'), (j, \tau'')} . \quad (\text{A.7})
 \end{aligned}$$

For the bare tight-binding model, all  $B_l$  block matrices are given by the exponentiated hopping matrix according to  $e^{-\Delta\tau \hat{H}}$ .



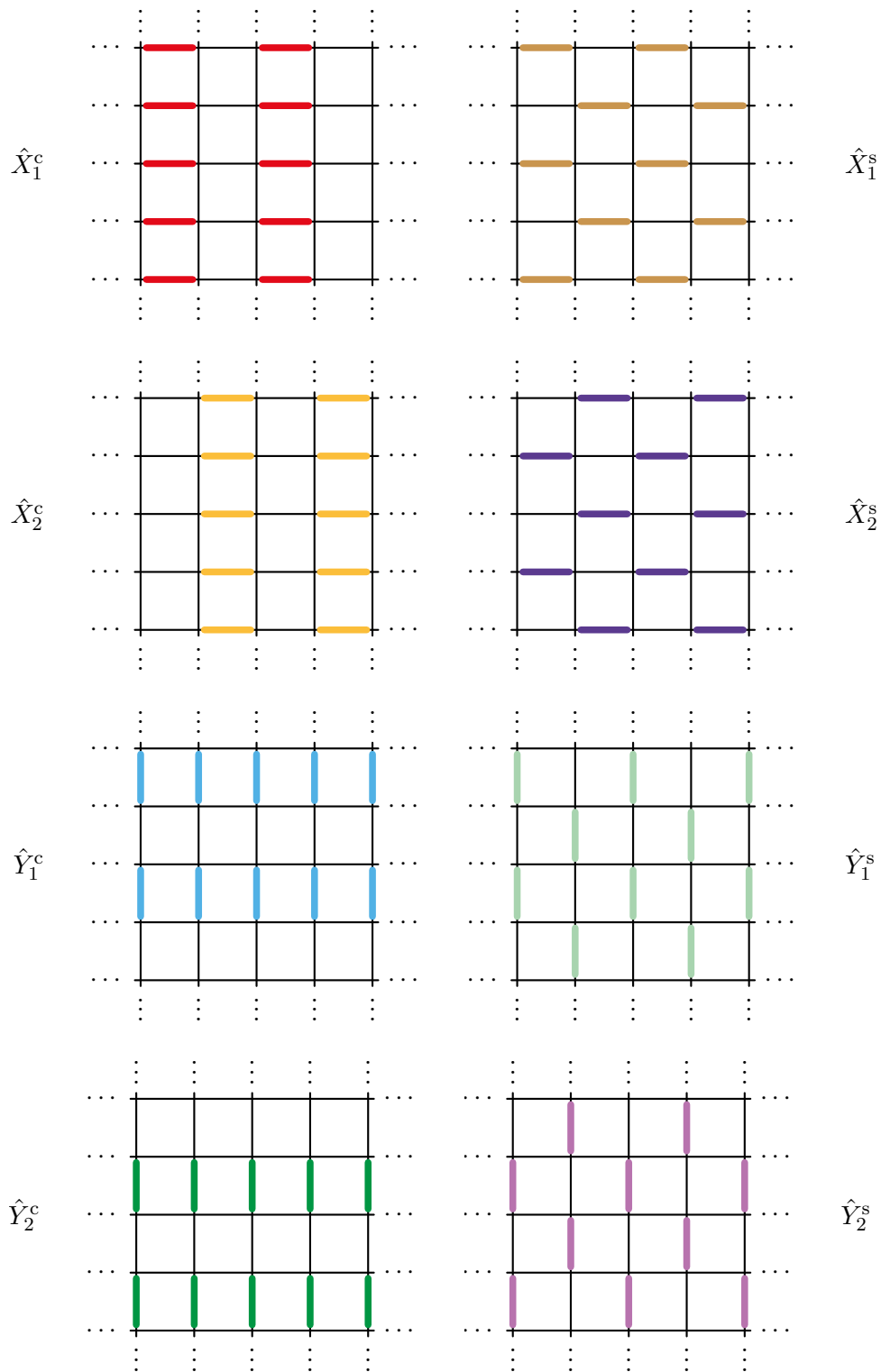


**Figure A.1:** Columnar and staggered patterns for the checkerboard decomposition.

We study the effects of the following four different combinations

$$\pi_1 : -\Delta\tau \hat{H} = \hat{X}_1^c + \hat{X}_2^c + \hat{Y}_1^c + \hat{Y}_2^c \rightsquigarrow e^{-\Delta\tau \hat{H}} \simeq e^{\hat{X}_1^c} e^{\hat{X}_2^c} e^{\hat{Y}_1^c} e^{\hat{Y}_2^c} \quad (\text{A.8})$$

$$\pi_2 : -\Delta\tau \hat{H} = \hat{X}_1^c + \hat{X}_2^c + \hat{Y}_1^s + \hat{Y}_2^s \rightsquigarrow e^{-\Delta\tau \hat{H}} \simeq e^{\hat{X}_1^c} e^{\hat{X}_2^c} e^{\hat{Y}_1^s} e^{\hat{Y}_2^s} \quad (\text{A.9})$$

$$\pi_3 : -\Delta\tau \hat{H} = \hat{X}_1^s + \hat{X}_2^s + \hat{Y}_1^c + \hat{Y}_2^c \rightsquigarrow e^{-\Delta\tau \hat{H}} \simeq e^{\hat{X}_1^s} e^{\hat{X}_2^s} e^{\hat{Y}_1^c} e^{\hat{Y}_2^c} \quad (\text{A.10})$$

$$\pi_4 : -\Delta\tau \hat{H} = \hat{X}_1^s + \hat{X}_2^s + \hat{Y}_1^s + \hat{Y}_2^s \rightsquigarrow e^{-\Delta\tau \hat{H}} \simeq e^{\hat{X}_1^s} e^{\hat{X}_2^s} e^{\hat{Y}_1^s} e^{\hat{Y}_2^s} \quad (\text{A.11})$$

to split up  $\hat{H}$  in order to approximate  $\exp(-\Delta\tau \hat{H})$ . Beside the reference results from a full eigendecomposition of  $\hat{H}$ , we consider a Taylor expansion as an additional opportunity to exploit the sparsity of  $\hat{H}$ . To ensure that the Taylor error is negligible compared to the general Trotter error of  $\mathcal{O}(\Delta\tau^2)$ , as in the initial decomposition (Eq. (3.4))<sup>1</sup> we expand up to third order in  $\Delta\tau$

$$\pi_T : e^{-\Delta\tau \hat{H}} \simeq \mathbb{1} - \Delta\tau \hat{H} + \frac{\Delta\tau^2}{2} \hat{H}^2 - \frac{\Delta\tau^3}{6} \hat{H}^3. \quad (\text{A.12})$$

We start the comparison by regarding the matrix norms of the approximation error for a single block matrix  $B_l$ . Using the spectral norm  $\|\cdot\|_2$  and the Frobenius norm  $\|\cdot\|_F$  we compute the approximation error

$$\epsilon_{\text{app}}^i = \left\| e^{-\Delta\tau H} - \pi_j \right\|_i \quad i \in \{2, F\}, \quad j \in \{1, 2, 3, 4, T\} \quad (\text{A.13})$$

on a  $8 \times 8$  lattice. Matrix norms are equivalent and for the considered norms  $\|\cdot\|_2 \leq \|\cdot\|_F$ . As table A.1 shows, the approximation errors of all checkerboard combinations are comparable with each other. Using the Frobenius norm they are in fact identical.

	$\pi_1$	$\pi_2$	$\pi_3$	$\pi_4$	$\pi_T$
$\ \cdot\ _2$	0.020759	0.021881	0.021881	0.023126	0.0011580
$\ \cdot\ _F$	0.081969	0.081969	0.081969	0.081969	0.0023505

**Table A.1:** Approximation error using a  $8 \times 8$  lattice ( $t = 1.0$ ,  $\Delta\tau = 0.1$ ) obtained by the spectral norm  $\|\cdot\|_2$  and Frobenius norm  $\|\cdot\|_F$ .

Although the norms of the errors are similar, the resulting Green's functions exhibit larger deviations. Figure A.2 shows that the different checkerboard decompositions vary in their physical results. On a  $8 \times 8$  lattice at a moderate temperature of  $\beta = 10.0$  we can already see how  $\pi_2$ ,  $\pi_3$  and  $\pi_4$  fail, while  $\pi_1$  and the Taylor series  $\pi_T$  are very close to the exact result. At lower

---

<sup>1</sup>To be precise, this systematical error vanishes if no interaction is considered, like in our example. Nevertheless, here we use the scaling of the error to determine the truncation of the Taylor series.

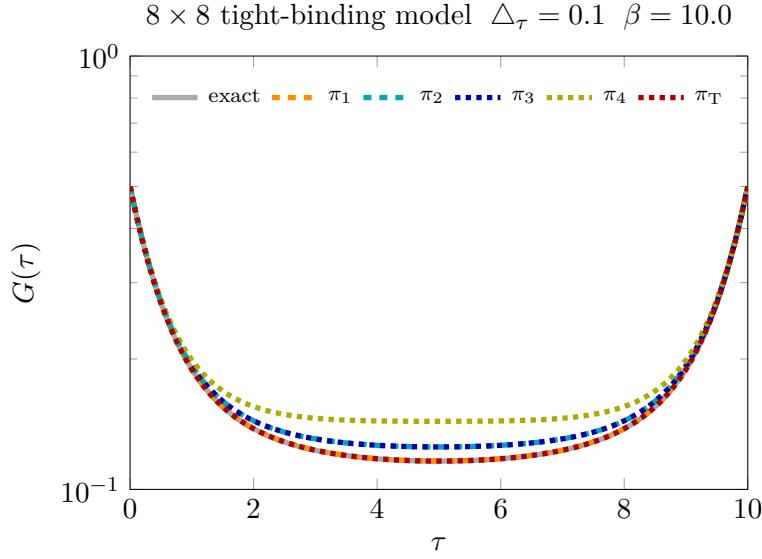


**Figure A.2:** The logarithmic plot of the local Green's function shows how the results differ depending on the used decompositions.

temperatures the deviations become larger. Regarding  $\beta = 24.0$  in Fig. A.3,  $\pi_4$  shows very strong deviations while  $\pi_2$  and  $\pi_3$  also violate the convexity predicted for physical Green's functions. On the other hand,  $\pi_1$  and the Taylor expansion  $\pi_T$  are still able to approximate the exact results with high precision.

The easiest way to avoid, or detect, a failure of the checkerboard decomposition is by reducing the imaginary step size  $\Delta\tau$ . As discussed above, the checkerboard decomposition is a Trotter decomposition and its error is dependent on  $\Delta\tau$ . In Fig. A.4 we show the results with a step size of  $\Delta\tau = 0.025$  instead of  $\Delta\tau = 0.1$ . Due to the four times smaller  $\Delta\tau$  the agreement of the approximation to the correct results is improved. However deviations are still visible for some combinations. The scaling of the computational effort as well as the memory requirements for quantum Monte Carlo methods like BSS-QMC and HQMC is strongly dominated by the lattice volume and the number of  $\tau$  slices. Therefore the decreasing of  $\Delta\tau$  is not desirable in general.

A look at the plots reveals a very good agreement between  $\pi_1$  and the exact result. It seems to be the preferable choice of the discussed combinations. And indeed, it profits from a symmetry the others do not have. We are going to prove

$$\left(\hat{X}_i^c \hat{Y}_j^c\right)^T = \hat{Y}_j^c \hat{X}_i^c = \hat{X}_i^c \hat{Y}_j^c \quad i, j \in \{1, 2\} \quad (\text{A.14})$$

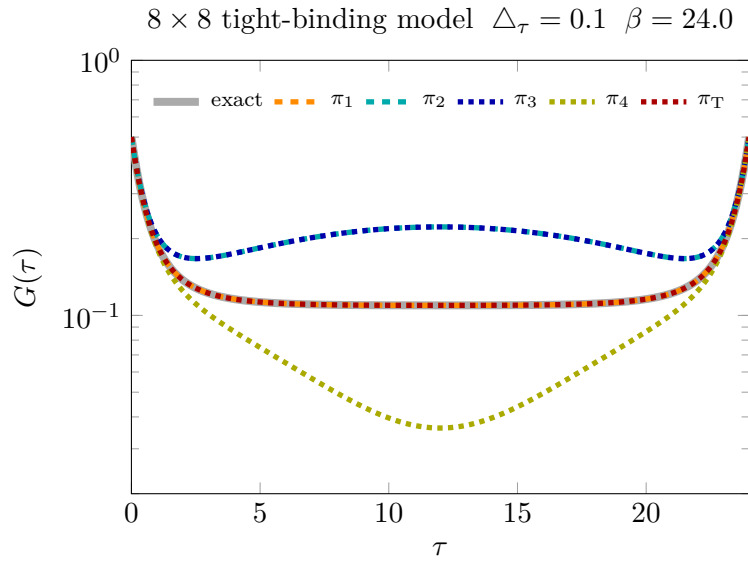


**Figure A.3:** The logarithmic plot of the local Green's functions shows unphysical results depending on the used decompositions.

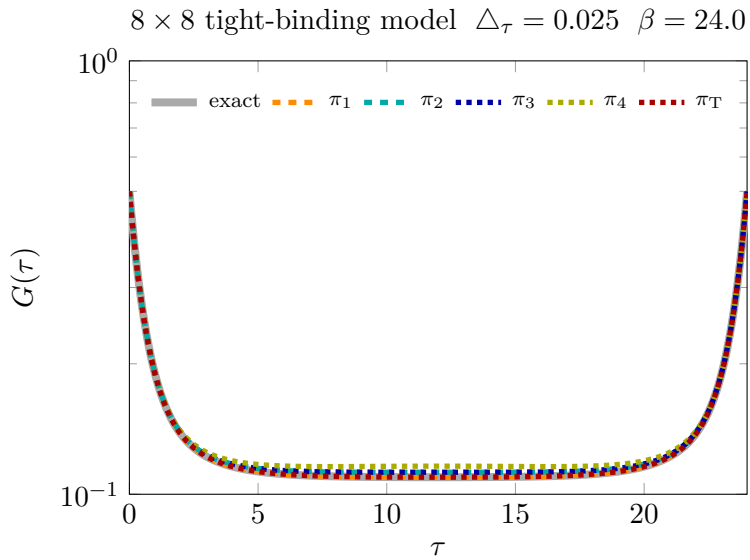


**Figure A.4:** A smaller Trotter step size improves the quality of the approximation.

and therefore

$$[\hat{X}_i^c, \hat{Y}_j^c] = 0. \quad (\text{A.15})$$

The first equality is trivial because the hopping on each bond is always symmetric. Using the anti-commutator relations of the fermionic creation and annihilation operator reduces the commutator of the hopping operators to a commutator of the associated matrices

$$[\hat{X}_i^c, \hat{Y}_j^c] = \left[ \sum_{k,l} \hat{c}_k^\dagger (X_i^c)_{k,l} \hat{c}_l, \sum_{m,n} \hat{c}_m^\dagger (Y_j^c)_{m,n} \hat{c}_n \right] = \sum_{k,l} \hat{c}_k^\dagger \left( [X_i^c, Y_j^c] \right)_{k,l} \hat{c}_l. \quad (\text{A.16})$$

To prove the symmetry of  $\hat{X}_i^c \hat{Y}_j^c$  we show the symmetry of the associated matrices and drop the  $-\Delta\tau t$  prefactor for readability. The numbering of lattice sites follows the  $x$ -direction first.

We rewrite  $X_1^c, X_2^c, Y_1^c, Y_2^c \in \mathbb{R}^{n^2 \times n^2}$  in terms of block matrices  $\Lambda_1, \Lambda_2, \mathbb{1} \in \mathbb{R}^{n \times n}$

$$X_1^c = \begin{pmatrix} \Lambda_1 & & \\ & \ddots & \\ & & \Lambda_1 \end{pmatrix}, \quad X_2^c = \begin{pmatrix} \Lambda_2 & & \\ & \ddots & \\ & & \Lambda_2 \end{pmatrix}, \quad (\text{A.17})$$

$$\Lambda_1 = \begin{pmatrix} 0 & 1 & & & \\ 1 & 0 & & & \\ & & 0 & 1 & \\ & & 1 & 0 & \\ & & & \ddots & \\ & & & & 0 & 1 \\ & & & & 1 & 0 \end{pmatrix}, \quad \Lambda_2 = \begin{pmatrix} 0 & & & & 1 \\ & 0 & 1 & & \\ & 1 & 0 & & \\ & & & \ddots & \\ & & & & 0 & 1 \\ 1 & & & & 1 & 0 \\ & & & & & 0 \end{pmatrix}, \quad (\text{A.18})$$

$$Y_1^c = \begin{pmatrix} 0 & \mathbb{1} & & & \\ \mathbb{1} & 0 & & & \\ & & 0 & \mathbb{1} & \\ & & \mathbb{1} & 0 & \\ & & & \ddots & \\ & & & & 0 & \mathbb{1} \\ & & & & \mathbb{1} & 0 \end{pmatrix}, \quad Y_2^c = \begin{pmatrix} 0 & & & & \mathbb{1} \\ & 0 & \mathbb{1} & & \\ & \mathbb{1} & 0 & & \\ & & & \ddots & \\ & & & & 0 & \mathbb{1} \\ \mathbb{1} & & & & \mathbb{1} & 0 \\ & & & & & 0 \end{pmatrix}. \quad (\text{A.19})$$

The symmetry we want to prove follows directly from the shape of the block matrices. Like for example

$$X_1^c Y_1^c = \begin{pmatrix} 0 & \Lambda_1 & & & \\ \Lambda_1 & 0 & & & \\ & & \ddots & & \\ & & & 0 & \Lambda_1 \\ & & & \Lambda_1 & 0 \end{pmatrix} = Y_1^c X_1^c. \quad (\text{A.20})$$

The symmetry of  $X_i^c Y_j^c$  implies a vanishing of the commutators in Eq. (A.16). Thus the operators  $\hat{X}_i^c$  and  $\hat{Y}_j^c$  are commuting with each other. First of all this implies that no error is introduced by splitting the exponentials in the last step of the approximation

$$e^{\hat{X}_1^c + \hat{X}_2^c + \hat{Y}_1^c + \hat{Y}_2^c} = e^{\hat{X}_1^c + \hat{Y}_1^c + \hat{X}_2^c + \hat{Y}_2^c} \simeq e^{\hat{X}_1^c + \hat{Y}_1^c} e^{\hat{X}_2^c + \hat{Y}_2^c} = e^{\hat{X}_1^c} e^{\hat{Y}_1^c} e^{\hat{X}_2^c} e^{\hat{Y}_2^c}. \quad (\text{A.21})$$

Because the exponential of a Hermitian operator is Hermitian,  $e^{\hat{X}_1^c + \hat{Y}_1^c} e^{\hat{X}_2^c + \hat{Y}_2^c}$  is a product of two Hermitian operators. The exponential function ensures furthermore a positive real spectrum of both operators. The authors of Ref. [95] prove that a product of two Hermitian operators with positive spectra also has a positive spectrum. Regarding the matrix representation, which is used to implement the checkerboard decomposition, the same has been proven for matrices in general. According to Ref. [96] the product of two symmetric real positive definite matrices has only real eigenvalues.

In contrast, the checkerboard decompositions  $\pi_2$ ,  $\pi_3$  and  $\pi_4$  exhibit complex eigenvalues which are most probably responsible for the observed deviations in the local Green's function. Their imaginary parts can cause oscillations in imaginary time that occur at larger step sizes  $\Delta\tau$ , as shown in Fig. A.5. Table A.2 contains the vector norms of the imaginary part of the eigenvalues obtained from the different checkerboard combinations. In agreement with our observations,  $\pi_4$  exhibits the largest vector norm what explains the unphysical behavior.

$\ \text{Im } \vec{\lambda}\ $	$\pi_1$	$\pi_2$	$\pi_3$	$\pi_4$	$\pi_T$
	0.0	0.028431	0.028431	0.040131	0.0

**Table A.2:** Vector norm of the imaginary part of the vector of eigenvalues. Due to hermiticity the Taylor expansion has only real eigenvalues, like  $\pi_1$ . ( $8 \times 8$  lattice,  $t = 1.0$ ,  $\Delta\tau = 0.1$ )

As long as we only consider the bare tight-binding hopping,  $\pi_1$  preserves hermiticity. As soon as the checkerboard decomposition is applied to interaction terms or the hopping gets modulated on

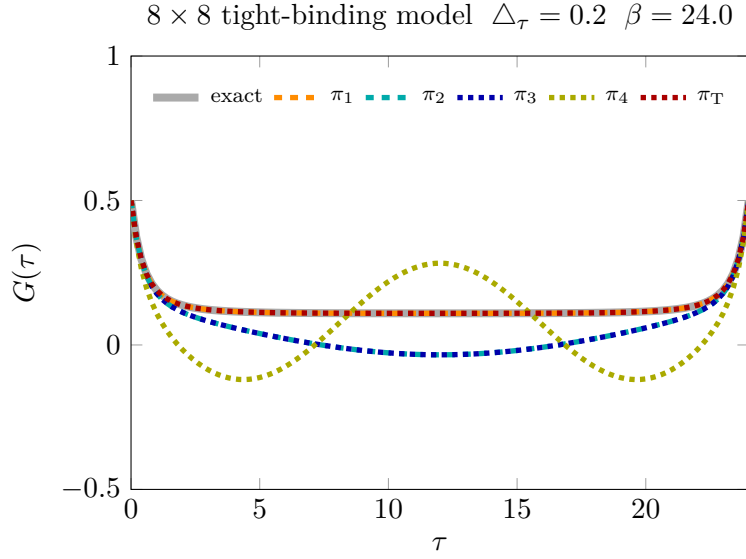


**Figure A.5:** Larger Trotter-step sizes lead to oscillations by increased imaginary parts in the eigenvalue spectrum of some combinations.

individual bonds, like in the SSH model, this property is lost.

In general, the problematic imaginary parts occurring in the eigenvalues after the checkerboard decomposition can be eliminated by using a symmetrized version like

$$\pi_1^s : e^{\hat{X}_1^c + \hat{X}_2^c + \hat{Y}_1^c + \hat{Y}_2^c} \simeq e^{\hat{X}_1^c/2} e^{\hat{X}_2^c/2} e^{\hat{Y}_1^c/2} e^{\hat{Y}_2^c/2} e^{\hat{Y}_2^c/2} e^{\hat{Y}_1^c/2} e^{\hat{X}_2^c/2} e^{\hat{X}_1^c/2}. \quad (\text{A.22})$$

The symmetrization recovers hermiticity of the price of more matrix multiplications. Figure A.6 shows the local Green's function for a symmetrized checkerboard decomposition. All combinations approximate the exact Green's function very accurately. Although more individual approximations are necessary and the number of introduced error terms is larger than before, the resulting error of the individual block matrices is reduced as documented in Table A.3.

	$\pi_1$	$\pi_2$	$\pi_3$	$\pi_4$
$\ \cdot\ _2$	0.0008305	0.0007057	0.0014178	0.0015122
$\ \cdot\ _F$	0.0030583	0.0030316	0.0050544	0.0050383

**Table A.3:** Approximation error for symmetrized checkerboard decomposition using a 8 × 8 lattice ( $t = 1.0$ ,  $\Delta\tau = 0.1$ ) obtained by the spectral norm  $\|\cdot\|_2$  and Frobenius norm  $\|\cdot\|_F$ .

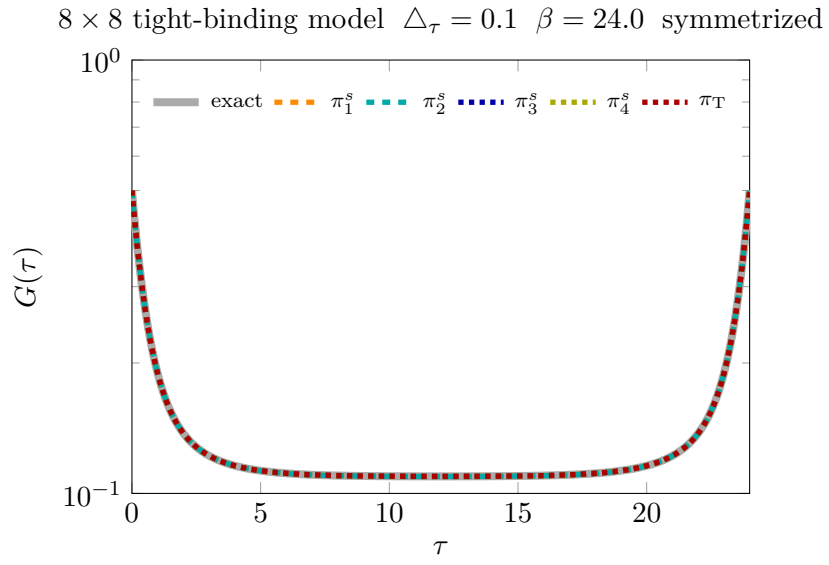


**Figure A.6:** Local Green's function for symmetrized checkerboard decompositions.

For additional information like error estimates or efficient minimal checkerboard decompositions in arbitrary dimensions and arbitrary coordination we refer to Ref. [97].



# B Appendix B

---

## Data analysis

In this chapter we briefly discuss the most important data analysis techniques which are used to evaluate Monte Carlo data. Especially the Markov chain properties of the discussed methods require an appropriate treatment. Every Monte Carlo sample of the HQMC and BSS method is obtained from the previous one. However, since the idea of Monte Carlo techniques is based on independent samples, undesirable correlations between the samples have to be taken into account during the data analysis. Ignoring them could bias the results, especially the errors of mean values.

### B.1 Jackknife method

The first technique we discuss is the so called jackknife method [98, 99, 100]. Its name is based on its universal applicability in data analysis. Besides the bootstrap, the jackknife is one of the most important resampling techniques. For a given data set  $x_1, x_2, \dots, x_N$  of observations the jackknife samples are defined by

$$\bar{x}_i = \frac{1}{N-1} \sum_{\substack{j=1 \\ j \neq i}}^N x_j, \quad (\text{B.1})$$

so a jackknife data point  $\bar{x}_i$  is the average over all samples except  $x_i$ . Averaging over the jackknife data gives the (unbiased) estimate

$$\bar{x} = \frac{1}{N} \sum_{i=1}^N \bar{x}_i. \quad (\text{B.2})$$

A correction factor of  $(N - 1)^2$ , due to the now trivial correlations within the jackknife data, has to be added to the variance (cf. Eq. (2.9)). In the end, the jackknife estimate of the standard error is

$$\epsilon_{\bar{x}} = \sqrt{\frac{N - 1}{N} \sum_{i=1}^N (\bar{x} - \bar{x}_i)^2}. \quad (\text{B.3})$$

## **B.2 Rebinning**

Another technique to figure out the correct errorbars of samples obtained by a Markov chain process is called rebinning. Here we provide only a short qualitative discussion of the method, for detailed discussions see Refs. [101, 102, 103]. Calculating the error of the samples without consideration of the relations between them leads to wrong errors. The time, here the number of samples, that is needed during a Markov chain process to overcome the correlations between the samples is named autocorrelation time. If nothing about the autocorrelation of the data is known, the rebinning scheme is an easy tool to measure it and obtain estimates for the error.

The idea is to combine more data within a single bin. First we do data analysis as usual and calculate the mean value and the error. Afterwards we combine two, or more, neighboring data points in the time series to a new sample. The new set of data has only half, or less, the size of the initial one. But because we combined correlated data points the data analysis returns another error value for the same mean value as before. Repeating the procedure generates values of the error depending on the number of data points combined to a single bin. Dependent on the underlying autocorrelation time the error grows and saturates to its correct value because the correlations between two rebinned data points are decreased. Figure B.1 illustrates the saturation of errors as a function of rebinning. Because the number of rebinned samples is also varied, depending on the bin size, fluctuations around the saturated error value are expected.

For a more detailed discussion of the rebinning method as well as an extensive review of Monte Carlo data analysis we refer to Ref. [102].

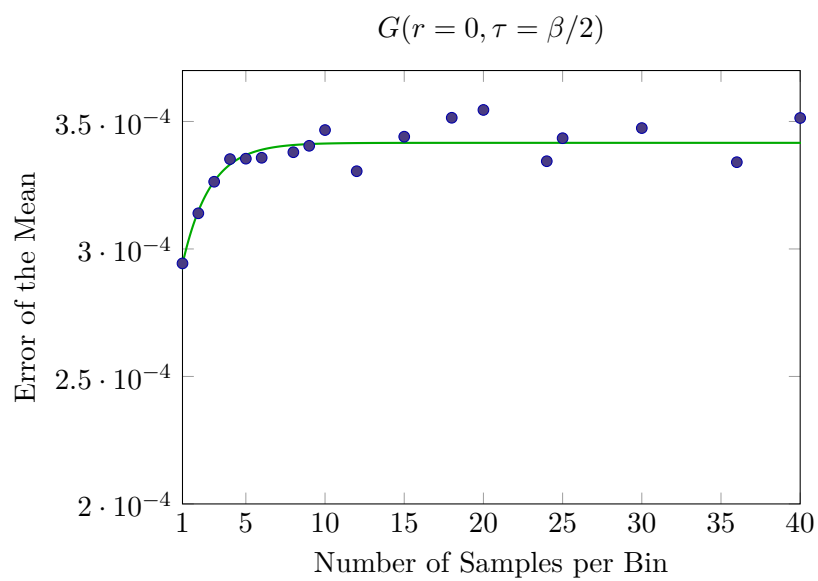


**Figure B.1:** Dependent on the number of samples combined to a bin the error of the mean value increases and converges. (SSH model:  $4 \times 4$  lattice  $\beta = 4.0$   $\tilde{g} = 1.5$   $\omega_0 = 1.0$ )



# Danksagung

Zum Abschluss möchte mich mich noch bei all den Menschen bedanken, die mich in den letzten Jahren maßgeblich beim Erstellen dieser Arbeit unterstützt haben.

Zunächst und vor allem bedanke ich mich bei Prof. Dr. Fakher Assaad dafür, dass er mir die Möglichkeit gegeben hat, bei ihm zu promovieren. Ich möchte mich für all das bedanken, was ich in den letzten Jahren von ihm lernen durfte, sowie die zahllosen inspirierenden Diskussionen und hilfreichen Anleitungen in der Zeit meiner Promotion.

Bei Prof. Dr. Giorgio Sangiovanni bedanke ich mich vielmals für die Übernahme der Zweitkorrektur.

Darüber hinaus danke ich Florian Goth und Martin Hohenadler für das gewissenhafte Korrekturlesen. Aber auch für die vielen Diskussionen, hilfreichen Erklärungen und kurzweiligen Fachsimpeleien bin ich ihnen zutiefst dankbar.

Für die kollegiale und angenehme Atmosphäre voller gegenseitiger Unterstützung in der Arbeitsgruppe möchte ich mich bei all denen bedanken, deren Bekanntschaft ich in den letzten Jahre hier machen durfte. Ich bedanke mich daher bei Manuel Weber, Johannes Hofmann, Martin Bercx, Thomas Lang, Francesco Parisen Toldin, Marcin Raczkowski, Toshihiro Sato, Jonas Schwab, Maxim Ulybyshev und Zhenjiu Wang für eine lange und prägende Zeit des gemeinsamen Forschens, Lernens und Lehrens.

Ganz besonderer Dank gebührt meiner Verlobten Lydia. Ihr danke ich mich für ihre Geduld, ihre Unterstützung und ihren Zuspruch. Aber auch für ihre penibelsten Kritiken an dieser Arbeit, die stets Ansporn für Verbesserungen waren, bin ich ihr über alle Maßen dankbar.

Abschließend möchte ich noch meinen Eltern Heinz und Ingrid sowie meiner Schwester Deborah dafür danken, dass sie mich stets unterstützt und bestärkt haben, solange ich denken kann.



## Bibliography

- [1] G. Czycholl, *Theoretische Festkörperphysik Band 2*, ch. Kollektiver Magnetismus, pp. 271–345. Berlin, Heidelberg: Springer, 2017.
- [2] T. Müller-Gronbach, E. Novak, and K. Ritter, *Monte Carlo-Algorithmen*. Berlin Heidelberg New York: Springer, 2012. Aufl. ed., 2012.
- [3] D. W. Hubbard, *How to measure anything : finding the value of intangibles in business*. Hoboken, N.J: Wiley, 2. ed. ed., 2010.
- [4] H. L. Anderson, “Metropolis, Monte Carlo, and the MANIAC,” *Los Alamos Science*, vol. 14, pp. 96–108, 1986.
- [5] H. H. Fehske, ed., *Computational many particle physics*. Lecture notes in physics ; 739, Berlin: Springer, 2008.
- [6] S. Duane, A. Kennedy, B. J. Pendleton, and D. Roweth, “Hybrid Monte Carlo,” *Phys. Lett. B*, vol. 195, no. 2, pp. 216–222, 1987.
- [7] A. Kennedy and B. Pendleton, “Cost of the generalised hybrid Monte Carlo algorithm for free field theory,” *Nuclear Physics B*, vol. 607, no. 3, pp. 456–510, 2001.
- [8] C. Gattringer and C. B. Lang, *Quantum Chromodynamics on the Lattice: An Introductory Presentation*, ch. Numerical simulation of pure gauge theory, pp. 73–101. Berlin, Heidelberg: Springer, 2010.
- [9] R. Blankenbecler, D. J. Scalapino, and R. L. Sugar, “Monte Carlo calculations of coupled boson-fermion systems. I,” *Phys. Rev. D*, vol. 24, pp. 2278–2286, Oct 1981.
- [10] R. T. Scalettar, D. J. Scalapino, R. L. Sugar, and D. Toussaint, “Hybrid molecular-dynamics algorithm for the numerical simulation of many-electron systems,” *Phys. Rev. B*, vol. 36, pp. 8632–8641, Dec 1987.

- [11] J. E. Drut and T. A. Lähde, “Is Graphene in Vacuum an Insulator?,” *Phys. Rev. Lett.*, vol. 102, p. 026802, Jan 2009.
- [12] M. V. Ulybyshev, P. V. Buividovich, M. I. Katsnelson, and M. I. Polikarpov, “Monte Carlo Study of the Semimetal-Insulator Phase Transition in Monolayer Graphene with a Realistic Interelectron Interaction Potential,” *Phys. Rev. Lett.*, vol. 111, p. 056801, Jul 2013.
- [13] T. Luu and T. A. Lähde, “Quantum Monte Carlo calculations for carbon nanotubes,” *Phys. Rev. B*, vol. 93, p. 155106, Apr 2016.
- [14] M. Bercx, F. Goth, J. S. Hofmann, and F. F. Assaad, “The ALF (Algorithms for Lattice Fermions) project release 1.0. Documentation for the auxiliary field quantum Monte Carlo code,” *SciPost Phys.*, vol. 3, p. 013, 2017.
- [15] M. Creutz, “Global Monte Carlo algorithms for many-fermion systems,” *Phys. Rev. D*, vol. 38, pp. 1228–1238, Aug 1988.
- [16] M. Hohenadler and T. C. Lang, “Autocorrelations in quantum monte carlo simulations of electron-phonon models,” in *Computational Many-Particle Physics* (H. Fehske, R. Schneider, and A. Weiße, eds.), pp. 357–366, Berlin, Heidelberg: Springer, 2008.
- [17] M. Weber, F. F. Assaad, and M. Hohenadler, “Directed-Loop Quantum Monte Carlo Method for Retarded Interactions,” *Phys. Rev. Lett.*, vol. 119, p. 097401, Aug 2017.
- [18] D. Reiter, “The monte carlo method, an introduction,” in *Computational Many-Particle Physics* (H. Fehske, R. Schneider, and A. Weiße, eds.), pp. 63–78, Berlin, Heidelberg: Springer, 2008.
- [19] S. M. Ulam, *Adventures of a Mathematician*. Berkeley: University of California Press, 1991.
- [20] N. Metropolis, A. W. Rosenbluth, M. N. Rosenbluth, A. H. Teller, and E. Teller, “Equation of State Calculations by Fast Computing Machines,” *The Journal of Chemical Physics*, vol. 21, no. 6, pp. 1087–1092, 1953.
- [21] W. K. Hastings, “Monte Carlo Sampling Methods Using Markov Chains and Their Applications,” *Biometrika*, vol. 57, no. 1, pp. 97–109, 1970.
- [22] C. P. Robert and G. Casella, *Monte Carlo Statistical Methods*. New York: Springer, 2004.
- [23] J. S. Liu, *Monte Carlo Strategies in Scientific Computing*. New York, NY: Springer, 2004.



- 
- [24] D. J. E. Callaway and A. Rahman, “Lattice gauge theory in the microcanonical ensemble,” *Phys. Rev. D*, vol. 28, pp. 1506–1514, Sep 1983.
- [25] S. Beyl, F. Goth, and F. F. Assaad, “Revisiting the hybrid quantum Monte Carlo method for Hubbard and electron-phonon models,” *Phys. Rev. B*, vol. 97, p. 085144, Feb 2018.
- [26] J. E. Hirsch, “Two-dimensional Hubbard model: Numerical simulation study,” *Phys. Rev. B*, vol. 31, pp. 4403–4419, Apr 1985.
- [27] M. Troyer and U.-J. Wiese, “Computational Complexity and Fundamental Limitations to Fermionic Quantum Monte Carlo Simulations,” *Phys. Rev. Lett.*, vol. 94, p. 170201, May 2005.
- [28] F. Assaad and H. Evertz, “World-line and determinantal quantum monte carlo methods for spins, phonons and electrons,” in *Computational Many-Particle Physics* (H. Fehske, R. Schneider, and A. Weiße, eds.), pp. 277–356, Berlin, Heidelberg: Springer, 2008.
- [29] E. Hairer, C. Lubich, and G. Wanner, *Geometric Numerical Integration: Structure-Preserving Algorithms for Ordinary Differential Equations: 31 (Springer Series in Computational Mathematics)*. Heidelberg: Springer, 2006.
- [30] R. I. McLachlan and G. R. W. Quispel, “Splitting methods,” *Acta Numerica*, vol. 11, pp. 341–434, 2002.
- [31] E. Hairer and G. Söderlind, “Explicit, Time Reversible, Adaptive Step Size Control,” *SIAM J. Sci. Comput.*, vol. 26, no. 6, pp. 1838–1851, 2005.
- [32] A. Meister, *Numerik linearer Gleichungssysteme: Eine Einführung in moderne Verfahren*, ch. Iterative Verfahren, pp. 69–229. Wiesbaden: Springer, 2015.
- [33] Z. Bai, W. Chen, R. Scalettar, and I. Yamazaki, *Multi-Scale Phenomena in Complex Fluids*, ch. Numerical Methods for Quantum Monte Carlo Simulations of the Hubbard Model, pp. 1–110. World Scientific, 2009.
- [34] I. Yamazaki, Z. Bai, W. Chen, and R. Scalettar, “A high-quality preconditioning technique for multi-length-scale symmetric positive definite linear systems,” *Numer. Math. Theor. Meth. Appl.*, vol. 2, pp. 469–484, Nov 2009.
- [35] M. Ulybyshev, N. Kintscher, K. Kahl, and P. Buividovich, “Schur complement solver for Quantum Monte-Carlo simulations of strongly interacting fermions,” *Comput. Phys. Commun.*, vol. 236, pp. 118–127, 2019.
-

- [36] S. R. White and J. W. Wilkins, “Fermion simulations in systems with negative weights,” *Phys. Rev. B*, vol. 37, pp. 5024–5031, Apr 1988.
- [37] M. Imada, “A Fermion Simulation Algorithm by Molecular Dynamics Technique Combined with Monte Carlo Method,” *J. Phys. Soc. Jpn.*, vol. 57, no. 8, pp. 2689–2698, 1988.
- [38] S. R. White, R. L. Sugar, and R. T. Scalettar, “Algorithm for the simulation of many-electron systems at low temperatures,” *Phys. Rev. B*, vol. 38, pp. 11665–11668, Dec 1988.
- [39] R. Brower, C. Rebbi, and D. Schaich, “Hybrid Monte Carlo simulation on the graphene hexagonal lattice,” *PoS Lattice 2011, 056*, 2011.
- [40] P. V. Buividovich and M. I. Polikarpov, “Monte Carlo study of the electron transport properties of monolayer graphene within the tight-binding model,” *Phys. Rev. B*, vol. 86, p. 245117, Dec 2012.
- [41] M. Hohenadler, F. Parisen Toldin, I. F. Herbut, and F. F. Assaad, “Phase diagram of the Kane-Mele-Coulomb model,” *Phys. Rev. B*, vol. 90, p. 085146, Aug 2014.
- [42] D. Smith and L. von Smekal, “Monte Carlo simulation of the tight-binding model of graphene with partially screened Coulomb interactions,” *Phys. Rev. B*, vol. 89, p. 195429, May 2014.
- [43] M. V. Ulybyshev and S. N. Valgushev, “Path integral representation for the Hubbard model with reduced number of Lefschetz thimbles,” *arXiv e-prints*, p. arXiv:1712.02188, Dec. 2017.
- [44] P. Buividovich, D. Smith, M. Ulybyshev, and L. von Smekal, “Hybrid Monte Carlo study of competing order in the extended fermionic Hubbard model on the hexagonal lattice,” *Phys. Rev. B*, vol. 98, p. 235129, Dec 2018.
- [45] S. Chakravarty, B. I. Halperin, and D. R. Nelson, “Low-temperature behavior of two-dimensional quantum antiferromagnets,” *Phys. Rev. Lett.*, vol. 60, pp. 1057–1060, Mar 1988.
- [46] S. R. White, D. J. Scalapino, R. L. Sugar, E. Y. Loh, J. E. Gubernatis, and R. T. Scalettar, “Numerical study of the two-dimensional Hubbard model,” *Phys. Rev. B*, vol. 40, pp. 506–516, Jul 1989.
- [47] W. P. Su, J. R. Schrieffer, and A. J. Heeger, “Solitons in polyacetylene,” *Phys. Rev. Lett.*, vol. 42, pp. 1698–1701, Jun 1979.

- 
- [48] Z.-X. Li, Y.-F. Jiang, and H. Yao, “Solving the fermion sign problem in quantum Monte Carlo simulations by Majorana representation,” *Phys. Rev. B*, vol. 91, p. 241117, Jun 2015.
- [49] A. N. Rubtsov, V. V. Savkin, and A. I. Lichtenstein, “Continuous-time quantum Monte Carlo method for fermions,” *Phys. Rev. B*, vol. 72, p. 035122, Jul 2005.
- [50] A. J. Heeger, S. Kivelson, J. R. Schrieffer, and W. P. Su, “Solitons in conducting polymers,” *Rev. Mod. Phys.*, vol. 60, pp. 781–850, Jul 1988.
- [51] M. Weber, F. Parisen Toldin, and M. Hohenadler, “Competing Orders and Unconventional Criticality in the Su-Schrieffer-Heeger Model,” *arXiv e-prints*, p. arXiv:1905.05218, May 2019.
- [52] J. K. Asbóth, L. Oroszlány, and A. Pályi, *A Short Course on Topological Insulators*, ch. The Su-Schrieffer-Heeger (SSH) Model, pp. 1–22. Cham: Springer, 2016.
- [53] A. Altland and B. D. Simons, *Condensed Matter Field Theory*. Cambridge: Cambridge University Press, 2 ed., 2010.
- [54] M. Weber, F. F. Assaad, and M. Hohenadler, “Excitation spectra and correlation functions of quantum Su-Schrieffer-Heeger models,” *Phys. Rev. B*, vol. 91, p. 245147, Jun 2015.
- [55] S. Tang and J. E. Hirsch, “Peierls instability in the two-dimensional half-filled Hubbard model,” *Phys. Rev. B*, vol. 37, pp. 9546–9558, Jun 1988.
- [56] S. Mazumdar, “Valence-bond approach to two-dimensional broken symmetries: Application to  $\text{La}_2\text{CuO}_4$ ,” *Phys. Rev. B*, vol. 36, pp. 7190–7193, Nov 1987.
- [57] Y. Ono and T. Hamano, “Peierls Distortion in Two-Dimensional Tight-Binding Model,” *J. Phys. Soc. Jpn.*, vol. 69, no. 6, pp. 1769–1776, 2000.
- [58] Q. Yuan and T. Kopp, “Coexistence of the bond-order wave and antiferromagnetism in a two-dimensional half-filled Peierls-Hubbard model,” *Phys. Rev. B*, vol. 65, p. 085102, Feb 2002.
- [59] K. Ji, K. Iwano, and K. Nasu, “Quantum Monte Carlo study on electron–phonon coupling in monolayer graphene,” *J. Electron Spectrosc. Relat. Phenom.*, vol. 181, no. 2, pp. 189–192, 2010. Electronic Spectroscopy and Structure (ICES-11).
- [60] F. F. Assaad and T. Grover, “Simple Fermionic Model of Deconfined Phases and Phase Transitions,” *Phys. Rev. X*, vol. 6, p. 041049, Dec 2016.

- [61] P. W. Anderson, “Random-Phase Approximation in the Theory of Superconductivity,” *Phys. Rev.*, vol. 112, pp. 1900–1916, Dec 1958.
- [62] E. Fradkin and J. E. Hirsch, “Phase diagram of one-dimensional electron-phonon systems. I. The Su-Schrieffer-Heeger model,” *Phys. Rev. B*, vol. 27, pp. 1680–1697, Feb 1983.
- [63] N. D. Mermin and H. Wagner, “Absence of Ferromagnetism or Antiferromagnetism in One- or Two-Dimensional Isotropic Heisenberg Models,” *Phys. Rev. Lett.*, vol. 17, pp. 1133–1136, Nov 1966.
- [64] Y. Ono, S. Chiba, and T. Hamano, “2D Peierls state in a square lattice – Effect of anisotropy,” *Synth. Met.*, vol. 152, no. 1, pp. 405–408, 2005. Proceedings of the International Conference on Science and Technology of Synthetic Metals.
- [65] S. Chiba, Y. Baba, and Y. Ono, “Two-Dimensional Spin-Peierls State With a Multimode Lattice Distortion,” *J. Phys. Soc. Jpn.*, vol. 75, no. 3, p. 034705, 2006.
- [66] S. Mazumdar, “Comment on ‘Peierls instability in the two-dimensional half-filled Hubbard model’,” *Phys. Rev. B*, vol. 39, pp. 12324–12326, Jun 1989.
- [67] S. Tang and J. E. Hirsch, “Reply to ‘Comment on ‘Peierls instability in the two-dimensional half-filler Hubbard model’ ’,” *Phys. Rev. B*, vol. 39, pp. 12327–12328, Jun 1989.
- [68] Y. Liu, Z. Wang, T. Sato, M. Hohenadler, C. Wang, W. Guo, and F. F. Assaad, “Superconductivity from the condensation of topological defects in a quantum spin-Hall insulator,” *Nat. Commun.*, vol. 10, no. 1, p. 2658, 2019.
- [69] T. Senthil, A. Vishwanath, L. Balents, S. Sachdev, and M. P. A. Fisher, “Deconfined Quantum Critical Points,” *Science*, vol. 303, no. 5663, pp. 1490–1494, 2004.
- [70] T. Senthil, L. Balents, S. Sachdev, A. Vishwanath, and M. P. A. Fisher, “Quantum criticality beyond the Landau-Ginzburg-Wilson paradigm,” *Phys. Rev. B*, vol. 70, p. 144407, Oct 2004.
- [71] E. H. Lieb, “Flux Phase of the Half-Filled Band,” *Phys. Rev. Lett.*, vol. 73, pp. 2158–2161, Oct 1994.
- [72] S. Pujari, T. C. Lang, G. Murthy, and R. K. Kaul, “Interaction-Induced Dirac Fermions from Quadratic Band Touching in Bilayer Graphene,” *Phys. Rev. Lett.*, vol. 117, p. 086404, Aug 2016.
- [73] L. Liu, H. Shao, Y.-C. Lin, W. Guo, and A. W. Sandvik, “Random-Singlet Phase in Disordered Two-Dimensional Quantum Magnets,” *Phys. Rev. X*, vol. 8, p. 041040, Dec 2018.

- 
- [74] A. V. Chubukov, S. Sachdev, and J. Ye, “Theory of two-dimensional quantum Heisenberg antiferromagnets with a nearly critical ground state,” *Phys. Rev. B*, vol. 49, pp. 11919–11961, May 1994.
- [75] N. Trivedi and M. Randeria, “Deviations from Fermi-Liquid Behavior above  $T_c$  in 2D Short Coherence Length Superconductors,” *Phys. Rev. Lett.*, vol. 75, pp. 312–315, Jul 1995.
- [76] A. Sen and A. W. Sandvik, “Example of a first-order Néel to valence-bond-solid transition in two dimensions,” *Phys. Rev. B*, vol. 82, p. 174428, Nov 2010.
- [77] C. Xu and L. Balents, “Quantum phase transitions around the staggered valence-bond solid,” *Phys. Rev. B*, vol. 84, p. 014402, Jul 2011.
- [78] C. Prosko, S.-P. Lee, and J. Maciejko, “Simple  $\mathbb{Z}_2$  lattice gauge theories at finite fermion density,” *Phys. Rev. B*, vol. 96, p. 205104, Nov 2017.
- [79] A. Smith, D. L. Kovrizhin, R. Moessner, and J. Knolle, “Dynamics of a lattice gauge theory with fermionic matter—minimal quantum simulator with time-dependent impurities in ultracold gases,” *Quantum Science and Technology*, vol. 3, p. 044003, aug 2018.
- [80] F. F. Assaad, *DMFT: From Infinite Dimensions to Real Materials*, vol. Lecture Notes of the Autumn School on Correlated Electrons 2018, ch. Quantum Monte Carlo Methods for Fermion-Boson Problems. Verlag des Forschungszentrums Jülich, 2018.
- [81] S. Gazit, M. Randeria, and A. Vishwanath, “Emergent Dirac fermions and broken symmetries in confined and deconfined phases of  $\mathbb{Z}_2$  gauge theories,” *Nat. Phys.*, vol. 13, pp. 484 EP –, Feb 2017. Article.
- [82] S. Gazit, F. F. Assaad, S. Sachdev, A. Vishwanath, and C. Wang, “Confinement transition of  $\mathbb{Z}_2$  gauge theories coupled to massless fermions: Emergent quantum chromodynamics and  $\text{SO}(5)$  symmetry,” *Proceedings of the National Academy of Sciences*, vol. 115, no. 30, pp. E6987–E6995, 2018.
- [83] E. Fradkin, *Field Theories of Condensed Matter Physics*. Cambridge: Cambridge University Press, 2 ed., 2013.
- [84] S. Elitzur, “Impossibility of spontaneously breaking local symmetries,” *Phys. Rev. D*, vol. 12, pp. 3978–3982, Dec 1975.
- [85] F. J. Wegner, “Duality in Generalized Ising Models and Phase Transitions without Local Order Parameters,” *J. Math. Phys.*, vol. 12, no. 10, pp. 2259–2272, 1971.

- [86] S. Sachdev, “Topological order, emergent gauge fields, and Fermi surface reconstruction,” *Rep. Prog. Phys.*, vol. 82, p. 014001, nov 2018.
- [87] J. B. Kogut, “An introduction to lattice gauge theory and spin systems,” *Rev. Mod. Phys.*, vol. 51, pp. 659–713, Oct 1979.
- [88] C.-Y. Hou, C. Chamon, and C. Mudry, “Electron Fractionalization in Two-Dimensional Graphenelike Structures,” *Phys. Rev. Lett.*, vol. 98, p. 186809, May 2007.
- [89] T. Sato, M. Hohenadler, and F. F. Assaad, “Dirac Fermions with Competing Orders: Non-Landau Transition with Emergent Symmetry,” *Phys. Rev. Lett.*, vol. 119, p. 197203, Nov 2017.
- [90] H. F. Trotter, “On the product of semi-groups of operators,” *Proc. Amer. Math. Soc.*, vol. 10, pp. 545–551, 1959.
- [91] M. Suzuki, “Generalized Trotter’s formula and systematic approximants of exponential operators and inner derivations with applications to many-body problems,” *Commun. Math. Phys.*, vol. 51, pp. 183–190, Jun 1976.
- [92] M. Suzuki, “Relationship between d-Dimensional Quantal Spin Systems and (d+1)-Dimensional Ising Systems: Equivalence, Critical Exponents and Systematic Approximants of the Partition Function and Spin Correlations,” *Progress of Theoretical Physics*, vol. 56, pp. 1454–1469, 11 1976.
- [93] M. Suzuki, “On the convergence of exponential operators—the Zassenhaus formula, BCH formula and systematic approximants,” *Commun. Math. Phys.*, vol. 57, pp. 193–200, Oct 1977.
- [94] C. Moler and C. Van Loan, “Nineteen Dubious Ways to Compute the Exponential of a Matrix, Twenty-Five Years Later,” *SIAM Rev.*, vol. 45, no. 1, pp. 3–49, 2003.
- [95] M. Hladnik and M. Omladič, “Spectrum of the product of operators,” *Proceedings of the American Mathematical Society*, vol. 102, no. 2, pp. 300–302, 1988.
- [96] L.-Z. Lu and C. Pearce, “Some New Bounds for Singular Values and Eigenvalues of Matrix Products,” *Annals of Operations Research*, vol. 98, pp. 141–148, Dec 2000.
- [97] C. Lee, “Minimal Split Checkerboard Method for Exponentiating Sparse Matrices and Its Applications in Quantum Statistical Mechanics,” *SIAM J. Sci. Comput.*, vol. 35, no. 2, pp. C143–C171, 2013.

- [98] M. H. Quenouille, “Notes on Bias in Estimation,” *Biometrika*, vol. 43, pp. 353–360, 12 1956.
- [99] J. W. Tukey, “Abstracts of Papers,” *Ann. Math. Statist.*, vol. 29, pp. 614–623, 06 1958.
- [100] B. Efron and C. Stein, “The Jackknife Estimate of Variance,” *Ann. Statist.*, vol. 9, pp. 586–596, 05 1981.
- [101] T. C. Lang, *Quantum Monte Carlo methods and strongly correlated electrons on honeycomb structures*. doctoralthesis, Universität Würzburg, urn:nbn:de:bvb:20-opus-53506, 2010.
- [102] W. Janke, “Monte carlo methods in classical statistical physics,” in *Computational Many-Particle Physics* (H. Fehske, R. Schneider, and A. Weiße, eds.), pp. 79–140, Berlin, Heidelberg: Springer, 2008.
- [103] A. D. Sokal and L. E. Thomas, “Exponential convergence to equilibrium for a class of random-walk models,” *J. Stat. Phys.*, vol. 54, pp. 797–828, Feb 1989.

